Vessel and Aneurysm Reconstruction using Speed and Flow Coherence Information in Phase Contrast Magnetic Resonance Angiograms

D. Phil. Thesis

(Albert) Chi Shing Chung

Oriel College

Medical Vision Laboratory
Department of Engineering Science
University of Oxford

Trinity 2001

A thesis submitted to the
Department of Engineering Science, University of Oxford,
in partial fulfilment of the requirements for the degree of Doctor of Philosophy.

Abstract

Phase contrast magnetic resonance angiography (PC-MRA) is a non-invasive method for 3D vessel delineation, which for each voxel not only provides measurement of speed (conveyed as a speed image), but also gives a three-component estimate of flow direction (in the form of phase images). In this thesis, we present a new approach to reconstructing vessels and aneurysms from PC-MRA, and demonstrate how speed and flow coherence information extracted from a PC-MRA dataset can be combined for detecting and reconstructing normal vessels and aneurysms with relatively low flow rate and low signal-to-noise ratio (SNR).

We propose to use a Maxwell-Gaussian mixture density to model the background signal and combine this with a uniform distribution for modelling vascular signal to give a Maxwell-Gaussian-uniform (MGU) mixture model of speed image intensity. The MGU model parameters are estimated by the Expectation-Maximisation (EM) algorithm. It is shown that the Maxwell-Gaussian mixture distribution models the background signal more accurately than a Maxwell distribution. Although the MGU model works satisfactorily in classifying the background and vessel voxels, for relatively low flow rate and low SNR vessel regions (especially inside an aneurysm), we find that it is hard to distinguish vessel voxels from the background voxels because of their low intensity value.

To deal with this problem, we propose to include the information about local flow coherence as *a priori* knowledge modelled by a Markov random field (MRF). A new coherence measure, namely *local phase coherence*, which incorporates information about the spatial relationships between neighbouring flow vectors, is defined and shown to be more robust to noise than prior coherence measures. The MGU statistical measure from the speed images and the local phase coherence measure from the phase images are combined in a Bayesian framework to estimate the posterior probabilities of vessel and background. It is shown that segmentation based on speed and flow coherence information gives a higher accuracy at low and high SNR values than segmentation using either speed or flow coherence information alone. Finally, the vessels and aneurysms are reconstructed by using a sub-voxel based level set method running on the estimated posterior probabilistic maps of vessel and background.

The new method is tested on an aneurysm phantom data set and 7 clinical data sets. The results show that the proposed method can help detecting and reconstructing relatively low flow and low SNR regions when both speed and flow coherence information are utilised.

Acknowledgements

Many people have contributed to this work and given me invaluable support and encouragement. I would like to express my gratitude to:

Alison Noble, for all her continual support, insights and comments on this research work during the past three enjoyable years;

Michael Brady, for his encouragement and for the excellent learning and research environment that he and Alison maintain at Oxford;

Paul Summers, for bringing me into the world of clinical magnetic resonance imaging, engaging me in many unforgettable discussions and proofreading parts of this thesis;

James Byrne and Antonio Martinez de la Cuesta, for initiating many helpful discussions about the clinical issues of this work and deepening my knowledge of radiology;

Members of the Medical Vision Laboratory (MVL) at Oxford University, especially Paul A., Paul W. and Djamal, for giving comments on and proofreading parts of this thesis; Robert, for providing flow field images; Gary, Miguel, Chris, Maud, Big Miguel, Kostas, Michael B., Margaret, Gerardo, Guofang, Yongyue, Gabriel, Lianghao, Jerome, Marius, Carolyn, Keith, Xujiong, Mark, James S., Jeong-Gyoo, Matt, Jean, David A., for their friendships at Oxford;

Members of the image-guided endovascular neuro-intervention project, David Hawkes, Alison Noble, Derek Hill, James Byrne, Tim Cox, Robert McLaughlin, John Hipwell, Kawal Rhodes and Graeme Penney, who have been a great source of inspiration and have offered great help in conducting experiments and data collections;

Helen Shen and Simon Yu, for encouraging me to enter into the field of medical vision;

The Croucher Foundation, Hong Kong, for offering me a postgraduate scholarship;

Maggie and Simon, for their support and understanding;

My parents, who first showed me how to learn new things;

and finally, to my wife, Alice, for her love.

Contents

Chapter 1

Introduction

The objective of this thesis is to reconstruct brain vessels and aneurysms from phase contrast magnetic resonance angiography (PC-MRA), which for each voxel provides an estimated rate of flow (speed) and a three-component estimate of flow direction (velocity field). It is common to perform vascular reconstruction relying on speed information alone [57, 49, 84, 87, 45, 46]. The focus of this work is to demonstrate that flow coherence (directional) information, which is extracted from the flow velocity field, can be combined with the speed information to detect and reconstruct normal vessels and aneurysms with relatively low signal-to-noise (SNR) and low flow rate.

This chapter begins by introducing the endovascular treatment of intracranial aneurysms, and then discusses the limitations of PC-MRA in detecting aneurysms and low flow regions. Finally, a summary of the thesis is given.

1.1 Endovascular treatment of intracranial aneurysms

An intracranial (brain) aneurysm is a bulge in the arteries and usually develops on the weak part of the major arteries located at the base of the brain[1]. The weakness of the arteries causes the vessel wall to swell outward and form the saccular aneurysm. The diameter of the aneurysm sac can range from a few millimetres to several centimetres. A ruptured aneurysm can cause fatal internal bleeding or haemorrhage.

[1]The common sites of the aneurysms are on the major arteries including internal carotid artery/posterior communicating artery (30%), anterior communicating artery (40%), bifurcation of the middle cerebral artery (25%) and basilar artery (5%) [83, pp. 3963]. 25% of patients has multiple aneurysms.

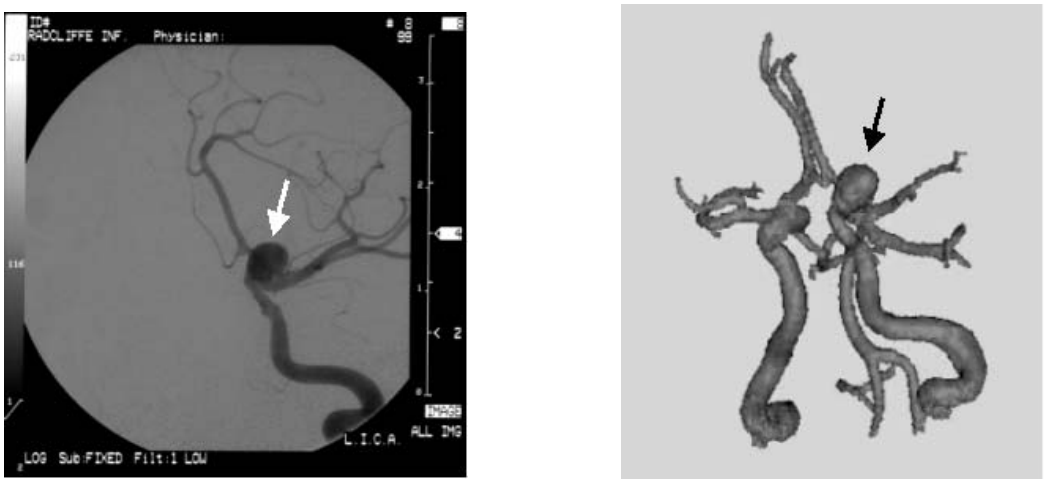

a. **b.**

Figure 1.1: *(a) A digital substraction angiogram (DSA) and (b) 3D reconstruction of the vasculature. Aneurysm is pointed to by an arrow in each image.*

An intracranial aneurysm is conventionally treated by craniotomy and microsurgical clipping. However, aneurysms are increasingly treated by endovascular (inside vessel) coil embolisation[2] (ECE) with the patient awake [33, 32, 15]. ECE is cost effective, less expensive than open surgery and only requires minimal operative intervention [23]. For ECE treatment, the platinum coils are delivered by a microcatheter guided by a neuroradiologist with the help of X-ray angiography, as illustrated in Figure 1.1a, which shows a 2D projection of an aneurysm and its connecting vessels. When the microcatheter reaches the aneurysm, the coil on the tip of the microcatheter is detached electrolytically and packed into the aneurysm. Thrombosis, which is induced by the coils, excludes the aneurysm from the blood circulation and prevents rupture of aneurysm. Clearly, it is a difficult task for a neuroradiologist to navigate the microcatheter with the 2D projection views alone.

To increase the success rate and procedural safety of the treatments, radiologists need a comprehensive and patient-specific understanding of the 3D shape, size and position of each aneurysm as well as the vasculature in the vicinity of the aneurysm, as shown in Figure 1.1b. This has created the need to develop 3D vascular reconstruction methods to generate vascular models that can be used for diagnosis, as well as treatment, of aneurysms and other arterial diseases.

[2]It is also known as the Guglielmi detachable coil (GDC) treatment after Guglielmi who developed the technique in early 1990's [33, 32].

1.2 Limitations of MRA

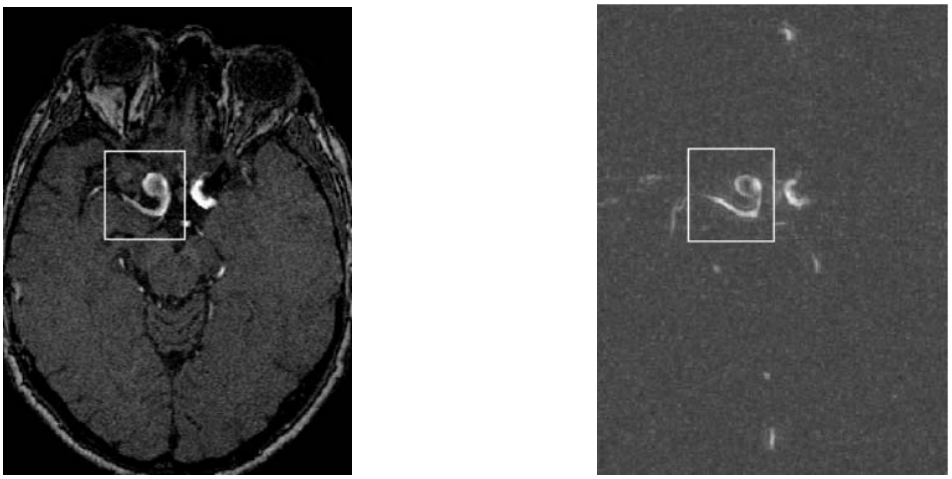

a. **b.**

Figure 1.2: *(a) Time-Of-Flight (TOF) MRA and (b) Phase Contrast (PC) MRA. As shown in the figures, the presence of an aneurysm causes significant vascular signal loss in the MRA speed image with some intensity levels approximately equal to those of the background signal, thereby, producing a heterogeneous intensity pattern within the aneurysm. The inclusion of such regions of inhomogeneous intensities is a challenge to robust vascular segmentation.*

Magnetic resonance angiography (MRA) is a collection of non-invasive, non-irradiating methods for 3D vessel delineation. Three major groups of MRA techniques are Time-Of-Flight (TOF) MRA, Contrast Enhanced (CE) MRA and Phase Contrast (PC) MRA. The main advantage of PC-MRA over TOF- and CE-MRA is that it not only gives information about vascular morphology but also provides additional velocity field information beyond the speed dependent intensity. Moreover, a PC-MRA speed image has good background suppression and displays two high contrast voxel types: vessel and background [74]. Medical diagnosis of vascular diseases is commonly performed on the basis of an analysis of MRA speed images alone, which assign high intensity to the moving blood and cerebrospinal fluid (CSF).

While most of the arterial anatomy can be shown clearly in MRA speed images, this is not the case, for example, for intracranial aneurysms. These can contain low or complex flow and are poorly represented in the images [79, 85]. The presence of an aneurysm causes significant vascular signal loss in an MRA speed image with some intensity levels approximately equal to those of background signal, thereby, producing a heterogeneous intensity pattern within

the aneurysm, as shown in Figures 1.2a and 1.2b. These inhomogeneous sub-regions are a challenge if vascular segmentation is to be robust.

A variety of approaches have been proposed for the segmentation of MRA speed images. For instance, Mclnerney et al. proposed topologically adaptable surfaces (T-surfaces), which is a variant of the classical deformable models but has an efficient topologically adaptable property for segmentation of intracranial vasculature [57]. Another variant, geodesic active contour was proposed to segment MRA speed images by Lorigo et al. [49]. In this case, the contour was implemented by using the level set methods [78] to offer flexible topological adaptability, and has been subsequently extended to be more locally adaptable according to the properties of local geometrical structure, for example, eigenvalues of the tensor [84]. A fast vessel delineation method was suggested by iteratively reconstructing a vessel segment defined by two user specified starting and end points [87]. Krissian et al. [45, 46] proposed a multiscale method to detect the vessel centreline and estimate vessel width based on eigenvalue and eigenvector analysis of the Hessian matrix, which relies on the partial differentiation of the MRA speed images. In all of these methods, an intensity-based gradient function was employed to give information about the boundaries of vessels. A drawback in using a gradient-based method is that, in practice, gradient values are not sufficiently high in the low flow regions for robust segmentation.

This work was entirely motivated by the need to develop a fully automatic reconstruction algorithm that could reliably segment and then reconstruct the vasculature including aneurysms, vessels at the vicinity of the aneurysms and other regions of low flow and low SNR from PC-MRA data. This will lead us to consider both the physics of PC-MRA image formation and segmentation based on both statistics of image formation and flow coherence. A result of applying our new method is shown in Figure 1.3.

Figure 1.3a shows a maximum intensity projection (MIP) of an aneurysm, which is located at the centre of the MIP. In the figure, the feeding (middle cerebral) vessel can be clearly seen because of its high intensity, whereas, the shape of the aneurysm is not obviously displayed because the flow rate inside is low and hence the intensity inside the aneurysm is low. A 3D reconstruction of the vasculature and aneurysm based on the speed information alone is depicted in Figure 1.3b. Observe that although the vessels are clearly reconstructed, the aneurysm is not well reconstructed due to its low intensity. Figure 1.3c shows the 3D reconstruction based on the integrated speed and flow coherence information approach, and

a. **b.** **c.**

Figure 1.3: *A closeup of an aneurysm: (a) maximum intensity projection (MIP), (b) 3D reconstruction using speed information alone and (c) 3D reconstruction using speed and flow coherence information.*

reveals that the shapes of the vessels and aneurysm are well delineated.

1.3 Thesis summary

In this thesis, we propose a new way of segmenting PC-MRA data. Firstly, based on knowledge of PC-MRA image formation and physical characteristics of blood flow, we investigate a tailored statistical description of the signals in PC-MRA data. Secondly, additional flow coherence information extracted from the velocity field is exploited to improve the segmentation quality of brain vessels and aneurysms. The new method is summarised in this section and in Figure 1.4.

In Chapter 2, we derive the background and vascular signal statistical models based on knowledge of image formation process and physical characteristics of blood flow, and combine these models to characterise the signals in PC-MRA speed images, in terms of a Maxwell-Gaussian-uniform (MGU) model. For each voxel in speed images, the model provides the probabilities of vessel and background based on its intensity value. In particular, we show that a Maxwell-Gaussian mixture distribution represents the background signal more accurately than a Maxwell distribution used in prior work [5]. The MGU model shows a better fit to clinical data and gives fewer false positive voxels (misclassified vessel voxels) in segmentation.

The method we propose draws on the fact that the flow pattern in the vasculature is locally coherent. In other words, if blood is flowing in a direction v, neighbouring voxels should have a high probability of exhibiting flow in the same direction v. In Chapter 3, a

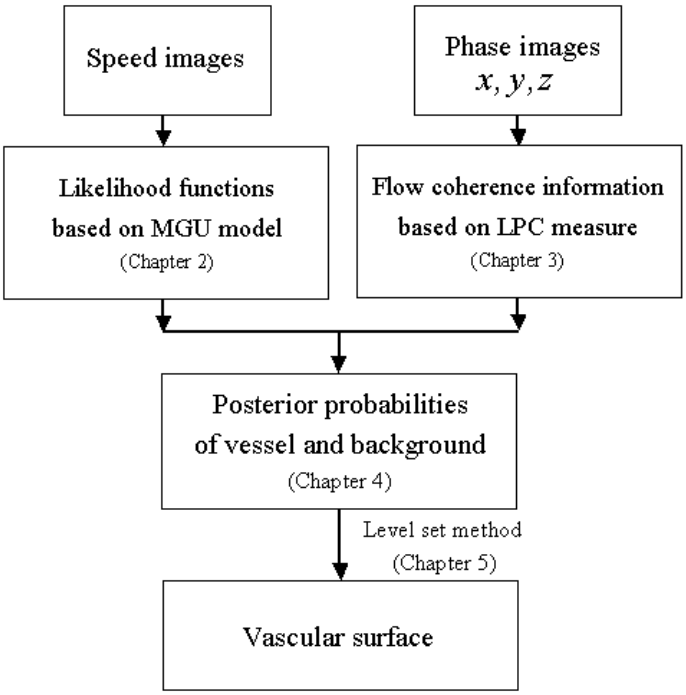

Figure 1.4: *A flow diagram of the proposed reconstruction process.*

local phase coherence (LPC) measure is derived to estimate the degree of coherence amongst neighbouring voxels, which gives useful information about the flow coherence within a local region. We find that (a) the LPC measure is more robust to noise than prior coherence measures and (b) when the SNR is low, segmentation using the LPC measure gives a more accurate segmentation result than a segmentation using speed information alone.

In Chapter 4, we combine the LPC measure and the statistical measure based on the MGU model in a Bayesian framework. The framework encodes knowledge of the PC-MRA speed image formation and physical characteristics of blood flow through the likelihood functions of vessel and background (MGU model) and incorporates the LPC measure into the prior probability by using a Markov random field (MRF) model. We show that the (Maximum *A-Posteriori*) MAP-MRF segmentation based on speed and flow coherence information outperforms segmentation using either speed or flow coherence information alone, and gives a higher segmentation accuracy than both at low and high SNR values.

The key ideas developed in Chapters 2 - 4 are integrated together in Chapter 5, which presents a sub-voxel based level set method to extract and reconstruct the vascular surface in the posterior probability maps of vessel and background obtained by the Bayesian framework

presented in Chapter 4. Experiments on a geometrically accurate straight tube show that the surface boundary extracted by the resulting sub-voxel level-set MAP-MRF method is clearly defined according to the probabilities of vessel and background, and smoother than the voxel-based equivalent method; and the accuracies of the sub-voxel based method and the voxel resolution method are comparable. We also show that the sub-voxel level-set MAP-MRF method is more accurate than an intensity gradient-based approach in extracting surface boundary.

Finally, in Chapter 6, the performance of the proposed method is evaluated on an aneurysm phantom and 7 clinical datasets. The results show that the combination of image and flow coherence information is useful in detecting and constructing normal vessels and aneurysms with relatively low SNR and low flow rate. We briefly present a summary and highlight possible directions of future work in Chapter 7.

Chapter 2

Maxwell-Gaussian-uniform (MGU) mixture model for phase contrast magnetic resonance angiographic images

2.1 Introduction

Phase Contrast Magnetic resonance angiography (PC-MRA) is a non-invasive and flow-dependent method of vessel visualisation. Phase contrast PC-MRA speed images are often used for medical diagnosis of vascular diseases because most of the arterial anatomy can be shown clearly in the images, which assign high intensity to the moving blood and cerebrospinal fluid (CSF). Moreover, a PC-MRA speed image has excellent background suppression and displays two high contrast voxel types: vessel and background [74]. The work described in this chapter was driven by the growing need for a better understanding of the PC-MRA signal statistical properties, including background and vascular signals, so that a better image segmentation could be derived for characterisation of vasculature and aneurysms.

Based on our knowledge of the PC-MRA image formation, in this chapter we propose to use a Maxwell-Gaussian mixture density model of the background signal combined with a uniform distribution for vascular signal to give a Maxwell-Gaussian-uniform (MGU) mixture model. The MGU model parameters are estimated by the Expectation-Maximisation (EM)

algorithm [10]. We have derived the update equations for this particular model and present a number of experiments on clinical images. The results show that the Maxwell-Gaussian mixture distribution (a) models the background signal more accurately than the Maxwell distribution, as used in [5], (b) exhibits a better fit to clinical data and (c) gives fewer false positive voxels (misclassified vessel voxels) in segmentation. Finally, we conclude by pointing out a potential problem in segmenting objects with low or complex flow and low SNR when using the proposed MGU model. A possible solution to this problem is discussed later in Chapters 3 and 4.

2.2 Phase contrast magnetic resonance angiography (PC-MRA)

PC-MRA is a flow-sensitised MR protocol for the imaging of vessels. It measures the x, y and z velocity components of the flow vectors on a voxel-by-voxel basis, and provides velocity field information about the motion of blood in the brain. To be more specific, each component of the flow vector is directly related to the *phase shift (angles)* ϕ induced by the dephasing and rephasing of the moving spins under the influence of the phase contrast magnetic field gradients [74]. In PC-MRA imaging, two images with voxel-wise phases ϕ_1 and ϕ_2, are acquired with different sensitivity to movement along a specific scan direction, resulting from the application of two opposite bipolar gradients of differing strengths. The resulting net phase shift (phase difference), $\Delta\phi = \phi_2 - \phi_1$, is then directly proportional to the directionally encoded velocity component v within a given voxel. The 3D velocity vector at each voxel v $(= (v_x, v_y, v_z)^T)$ is composed of the three velocity components measured separately. A speed-based image may be obtained by applying a modulus operation to the three directional components voxel by voxel, as shown in Figure 2.1. To suppress the spurious phase shifts occurring in extremely low regions (e.g. background air), an average magnitude mask is also applied at each voxel. Although this reconstructed image is a magnitude-weighted speed image, it is commonly referred to as *speed image* (since the phase shifts are flow sensitized along the three orthogonal components, x, y and z, the result is directly proportional to the speed).

A typical speed image is shown in Figure 2.2, in which the intensity value is directly proportional to the flow rate. The higher the velocity, the higher the image intensity level assigned to the voxel. A PC-MRA acquisition of the brain normally takes about $10mins$

to obtain all 3 velocity components. Four data volumes, three phase values (v_x, v_y and v_z) and speed (or flow magnitude), are obtained after the scanning. For clinical diagnosis, only the PC-MRA speed images are commonly used for visualisation of vessels. The three phase values are almost exclusively used for visualisation of flow fields.

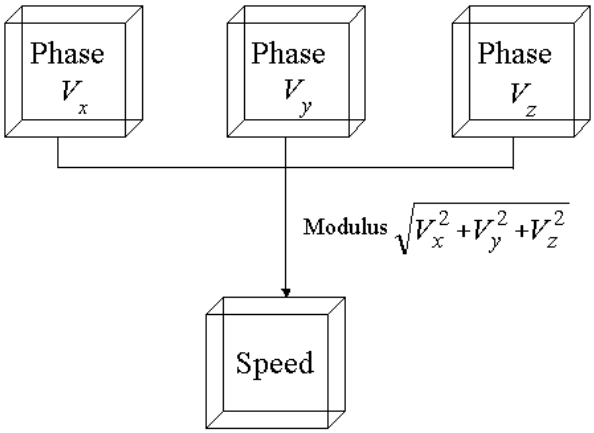

Figure 2.1: *Formation of a speed image. A speed image is obtained by applying the modulus operation to the three directional components.*

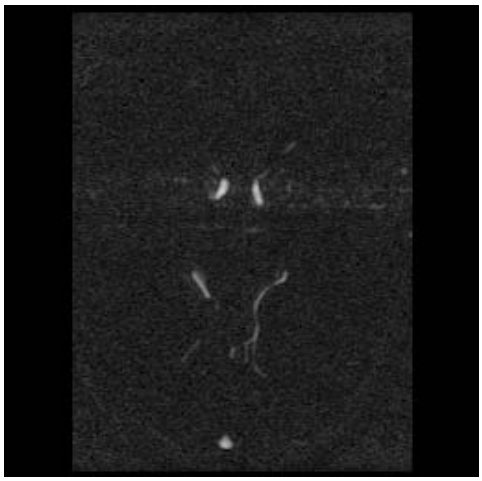

Figure 2.2: *A typical PC-MRA speed image, in which the intensity value is directly proportional to the flow rate. The higher the velocity, the higher the image intensity level assigned to the voxel.*

2.3 Statistical analysis of PC-MRA signals

This section derives statistical distributions for the target vascular signals in MRA speed images as well as for background regions containing static, signal generating tissues (brain, CSF and scalp) or signal-absent material (air, cortical bone) in accordance with the PC-MRA image reconstruction process and physical characteristics of blood flow. These two models are then combined additively to form a complete distribution of an MRA speed image.

2.3.1 Phase angle definition and its properties

The **phase angle** of a complex-valued MR signal S_1 is defined as ϕ_1 and computed by

$$arg(S_1) = \tan^{-1}\left(\frac{Im\{S_1\}}{Re\{S_1\}}\right), \tag{2.1}$$

where $Re\{S_1\}$ and $Im\{S_1\}$ denote real and imaginary components of the signal respectively, as illustrated in Figure 2.3. It is assumed that both real and imaginary components are statistically independent and corrupted by zero-mean Gaussian noise with equal variance σ_p^2 [37], i.e. $Re\{S_1\}$ and $Im\{S_1\} \sim N(0, \sigma_p^2)$. The probability density function (PDF) of ϕ_1 is given by [47]

$$f_{\phi_1}(\phi_1) = \frac{e^{-\kappa^2}}{2\pi} \cdot \{1 + \sqrt{\pi}\kappa \cdot \cos(\phi_1 - \bar{\phi_1}) \cdot e^{\kappa^2 \cdot \cos^2(\phi_1 - \bar{\phi_1})} \cdot [1 + erf(\kappa \cdot \cos(\phi_1 - \bar{\phi_1}))]\}, \tag{2.2}$$

where $\phi_1 \in [-\pi, \pi)$, $\kappa = \frac{M_1}{\sqrt{2}\sigma_p}$, $erf(x) = \left(\frac{2}{\sqrt{\pi}}\right) \cdot \int_0^x e^{-w^2} dw$ is the error function, $\bar{\phi_1}$ is the mean phase and M_1 is the magnitude of signal S_1. Note that $f_{\phi_1} = 0$ for $\phi_1 \notin [-\pi, \pi)$. The PDFs at different signal-to-noise ratios ($SNR = \frac{M_1}{\sigma_p} = 0, 1, 3$ and 6) are plotted in Figure 2.4. It is noted that the PDF becomes uniformly distributed when the SNR is zero, and tends to a Gaussian distribution when the SNR is sufficiently high.

2.3.2 Speed image definition and its properties

For each velocity component at a voxel, two complex-valued signals, S_2 and S_1, are acquired. These signals experience the same pulse sequence excitation and spatial encoding during imaging but differ by the polarity or strength of a bipolar gradient applied along the axis of the velocity component being measured. A velocity induced phase shift (phase difference) $\Delta\phi$ is produced by the angular difference between the two signal phases [72], i.e.

$$\Delta\phi = \phi_2 - \phi_1 = arg(S_2) - arg(S_1), \tag{2.3}$$

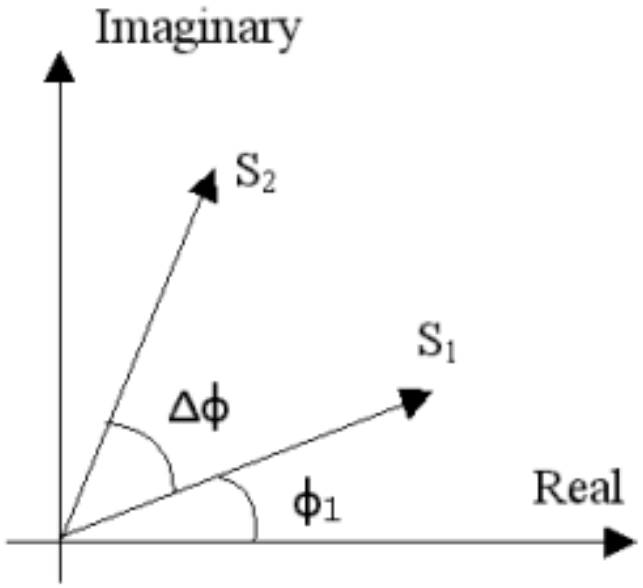

Figure 2.3: *Phase angle ϕ_1 and signal phase shift $\Delta\phi = \phi_2 - \phi_1$.*

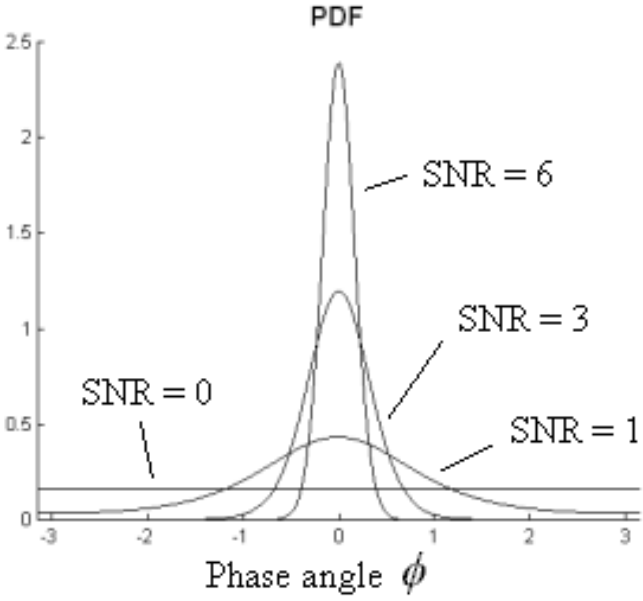

Figure 2.4: *Probability density functions (PDF) of a phase angle ϕ_1 in different signal-to-noise ratios (SNR). It is noted that the PDF becomes uniformly distributed when the SNR is zero, and tends to a Gaussian distribution when the SNR is sufficiently high.*

as shown in Figure 2.3. The resulting net phase $\Delta\phi$ for a voxel is directly proportional to the flow rate of material in the voxel in the specified direction.

An MRA speed image is reconstructed on a voxel-by-voxel basis by taking the modulus of the three corresponding phase shifts, $\Delta\phi_x$, $\Delta\phi_y$ and $\Delta\phi_z$, sensitised along orthogonal x, y and z axes respectively. An average magnitude mask $\bar{M}$ is also applied to suppress the spurious phase shifts occurring in extremely low signal regions (e.g. background air), i.e.

$$\begin{aligned} i &= \bar{M} \cdot \sqrt{\Delta\phi_x^2 + \Delta\phi_y^2 + \Delta\phi_z^2}, & (2.4) \\ &= \sqrt{(\bar{M}\Delta\phi_x)^2 + (\bar{M}\Delta\phi_y)^2 + (\bar{M}\Delta\phi_z)^2}, & (2.5) \end{aligned}$$

where i is the resulting image intensity and $\bar{M} = \frac{1}{N_{acq}} \sum_{n=1}^{N_{acq}} S_n$ is the average magnitude of all signals acquired at the same voxel, N_{acq} is the number of acquisitions at each voxel.

The number of acquisitions (N_{acq}) at each voxel depends on the pattern of bipolar gradients applied: for a six-point reconstruction method ($N_{acq} = 6$) a pair of oppositely oriented bipolar gradients are used for each velocity component, while for a four-point reconstruction method ($N_{acq} = 4$) a single image acquired with a null bipolar gradient (i.e. no velocity sensitivity) is used in combination with each of three velocity encoded images [6]. Although this reconstructed image is a magnitude-weighted speed image, it is commonly referred to as *speed image* (since the phase shifts are flow sensitized along the three orthogonal components, x, y and z, the result is directly proportional to the speed).

2.3.3 Statistical analysis of vascular signals

In modelling the intensity characteristics of vessel voxels, we assume a laminar flow pattern is present. In this case, for a circular vessel cross-section, the velocity flow is then parabolic [16, 68, 67], as shown in Figure 2.5. Hence, the intensity profile is given by

$$i(r) = C \cdot \left(1 - \frac{r^2}{R^2}\right), \quad (2.6)$$

where i is the intensity and is a function of r, C is a scaling constant (incorporating the signal magnitude), R is the vessel radius and r is the distance from vessel centre to the boundary. The PDF $f_{vessel}(i)$ for a vessel voxel that has intensity i is directly proportional to the image area, $a(x = i)$, in which all the voxels have the same intensity i. $f_{vessel}(i)$ is calculated as the rate-of-change of area having intensity greater than or equal to i, i.e.

$$f_{vessel}(i) \propto \left| \frac{da(x \geq i)}{di} \right|. \quad (2.7)$$

The area $a(x \geq i)$ is given by, using Equation 2.6,

$$a(x \geq i) = \pi r^2 = \pi R^2 \cdot \left(1 - \frac{i}{C}\right). \tag{2.8}$$

Therefore, the PDF $f_{vessel}(i)$ is constant and can be regarded as a uniform distribution, which can be expressed as

$$f_{vessel}(i) = w_U f_U(i), \tag{2.9}$$

where w_U is a weight (or prior probability) assigned to the uniform distribution, $f_u(i) = \frac{1}{I_{max}}$, I_{max} is the maximum intensity in the observed frequency histogram. Although, in practice, the visible vessels have voxel intensities in the high intensity region, the number of vessel voxels in clinical images is a small proportion (about 1% - 4%) of the frequency histogram. Hence, for the sake of simplicity, we assume that the uniform distribution spreads over the entire intensity range $[0, \ldots, I_{max}]$.

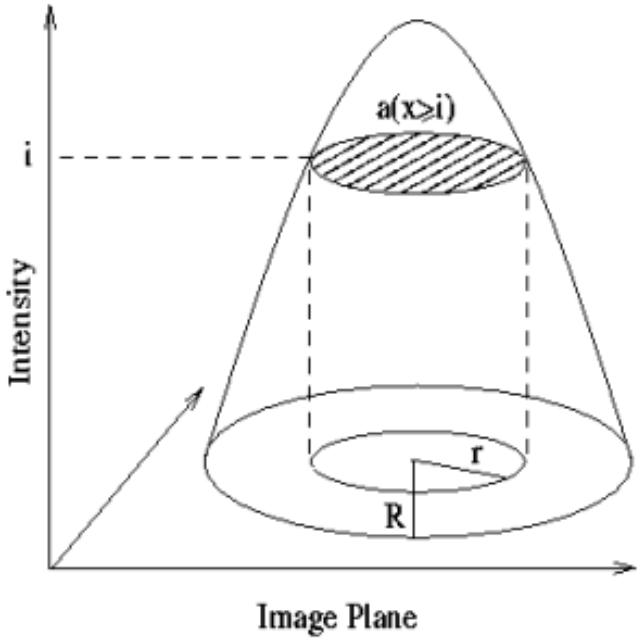

Figure 2.5: *In modelling the intensity characteristics of vessel voxels, we assume a laminar flow pattern is present. In this case, for a circular vessel cross-section, the velocity flow is then parabolic.*

2.3.4 Statistical analysis of background signals

A more involved description is required for signals in regions of background as a wide range of phase shift behaviour may be encountered, and also in practice the background regions occupy a large proportion of a speed image.

According to prior work [5], $\bar{M}\Delta\phi_j$ is assumed to follow a zero-mean Gaussian distribution in Equation 2.5, where $j = x$, y and z. The distribution described by the modulus of three independent zero-mean Gaussians with equal variance σ_M^2 is a Maxwell distribution. Hence, according to the Equation 2.5, the PDF of background signal is given by a Maxwell distribution [5, 71],

$$f_M(i) = \frac{2i^2}{\sqrt{2\pi}\sigma_M^3} \cdot e^{\left(\frac{-i^2}{2\sigma_M^2}\right)}, \tag{2.10}$$

where $i \geq 0$ and $f_M(i) = 0$ when $i < 0$.

Figures 2.6a and 2.6b show a background region of interest (ROI) inside an in-vivo speed image and its corresponding histogram respectively. The histogram was fitted by a Maxwell distribution using the relationship $\sigma_M = \frac{I_{peak}}{\sqrt{2}}$, where I_{peak} is the intensity value at which the histogram achieves its maximum, i.e. $\frac{df_M(i)}{di} = 0$ at $i = I_{peak}$. In Figure 2.6b, it is observed that the Maxwell distribution fits well in the low intensity region, but not in the high intensity region (indicated by an arrow in the figure).

The reason for the failure of the Maxwell distribution in describing the background signal is the deviation of the magnitude-weighted phase values $\bar{M}\Delta\phi$ in Equation 2.5 from a Gaussian distribution. Neither of the tails in the magnitude-weighted phase image histogram is perfectly fitted by a Gaussian distribution in clinical images (indicated by the arrows in Figure 2.7b, in which, for the purpose of illustration, a 95% HPD[1] interval is used). This distortion of the ideal Gaussian model results from contributions due to slight tissue motion, small vessels of sub-voxel size, ghosting artifacts and relatively low SNR in background regions of the phase images. These factors contribute to high voxel intensity in nominally background regions of the images. As well, as plotted in Figure 2.4, the low SNR makes the distributions of phase angles, ϕ_1 and ϕ_2, deviate from the Gaussian distribution, which in turn flattens the distribution of $\Delta\phi$ and makes the probabilities at both tails higher. To-

[1] A formal definition of HPD interval can be found in [12]. In general, given a probability content (95%), the HPD interval occupies the smallest volume in the parameter space (e.g. $[0, \ldots, I_{max}]$), which contains most (95%) of the probability. Moreover, the probability density of every point inside the HPD interval is at least as large as that of any point outside it.

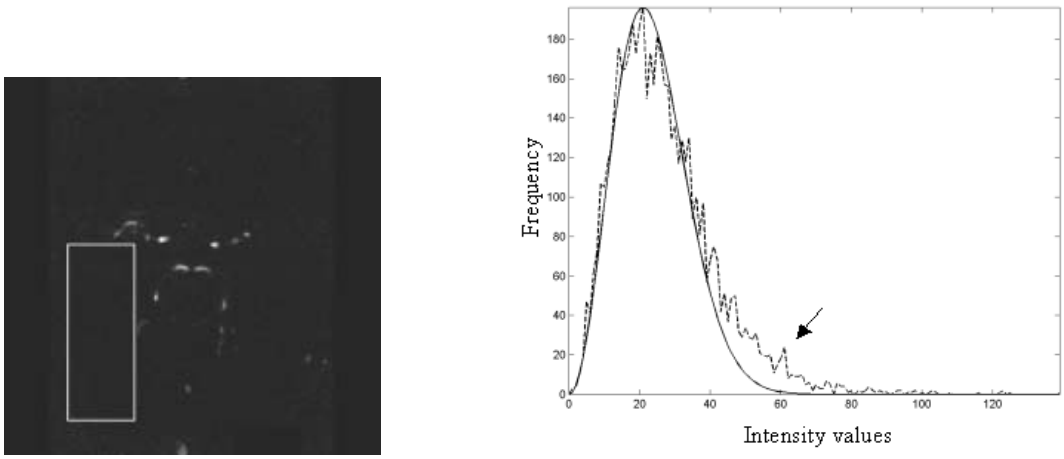

a. **b.**

Figure 2.6: *(a) Region-of-interest (ROI) inside a speed image and (b) its corresponding histogram (dashed) respectively. In Figure 2.6b, it is observed that the Maxwell distribution (solid) fits well in the low intensity region, but not in the high intensity region (indicated by an arrow in Figure 2.6b).*

gether with the Rician nature of noise in the signal magnitude [5], it is not surprising that the distribution of their product, the magnitude-weighted phase value $\bar{M}\Delta\phi$, is not entirely Gaussian when the SNR is low, especially in background regions.

To accommodate this recognised failing of the Maxwell distribution model and reduce the error in fitting the background signal [58], we assume that there are two additional residual distributions each located at the side of the ideal Gaussian model and they follow non-zero mean Gaussian pattern. Therefore, for each encoding direction, the PDF of the magnitude-weighted phase value $\bar{M}\Delta\phi$ consists of a zero-mean Gaussian (located at the centre) and two non-zero mean Gaussian distributions (located at each side), and is given by

$$f_{\bar{M}\Delta\phi_k}(\bar{M}\Delta\phi_k) = \frac{w_l}{\sqrt{2\pi}\sigma_l} \cdot e^{\frac{-(\bar{M}\Delta\phi_k-\mu_l)^2}{2\sigma_l^2}} + \frac{w_c}{\sqrt{2\pi}\sigma_c} \cdot e^{\frac{-\bar{M}\Delta\phi_k^2}{2\sigma_c^2}} + \frac{w_r}{\sqrt{2\pi}\sigma_r} \cdot e^{\frac{-(\bar{M}\Delta\phi_k-\mu_r)^2}{2\sigma_r^2}}, \quad (2.11)$$

where $k = \{x, y, z\}$; w_l, w_c and w_r are the weights attached to the distributions, and sum to one; μ_l and μ_r are the means; σ_l and σ_r are the standard deviation; subscripts l and r represent left and right distributions respectively. By using the EM algorithm to estimate the parameters in Equation 2.11 [10], Figure 2.8a shows the fitted distribution using one zero-mean Gaussian distribution and two opposite non-zero mean Gaussian distributions. Figure 2.8b illustrates the individual distributions. Appendix A will provide a more detailed

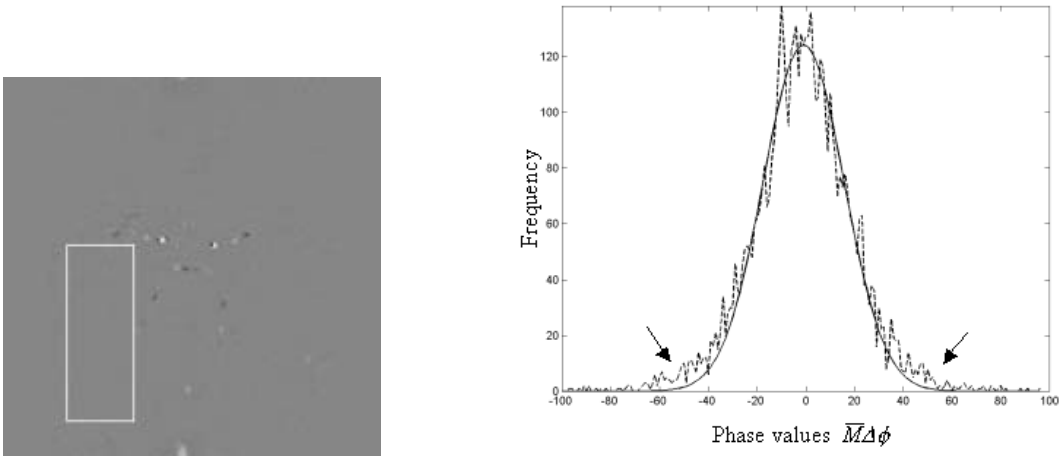

a. **b.**

Figure 2.7: *(a) Region-of-interest (ROI) inside a magnitude-weighted phase image $\bar{M}\Delta\phi$ and (b) its corresponding histogram (dashed) respectively. In Figure 2.7b, it is observed that both tails of the magnitude-weighted phase image histogram are not perfectly fitted by a Gaussian distribution (solid) (indicated by the arrows in Figure 2.7b).*

discussion about the triple Gaussian mixture model.

After application of modulus operator on the three magnitude-weighted phase values, as derived in Appendix A, the PDF of background signal can be approximated by a linear mixture of a Maxwell distribution $f_M(i)$ with variance σ_M^2 and a Gaussian distribution $f_G(i)$ with mean μ_G and variance σ_G^2, which is given by

$$f_{background}(i) = w_M f_M(i) + w_G f_G(i), \tag{2.12}$$

where w_M and w_G are weights (or prior probabilities) assigned to the Maxwell and Gaussian distributions respectively. As shown in Figure 2.9, using the EM algorithm (detailed in Section 2.4), a Maxwell and Gaussian mixture model achieves a better fit to the given histogram of a PC-MRA speed image, when compared with Figure 2.6b.

2.3.5 Maxwell-Gaussian-uniform (MGU) model

Thus, with reference to Equations 2.12 and 2.9, we conclude that the overall PDF $f(i)$ of a PC-MRA speed image can be modelled as a Maxwell-Gaussian and uniform finite mixture

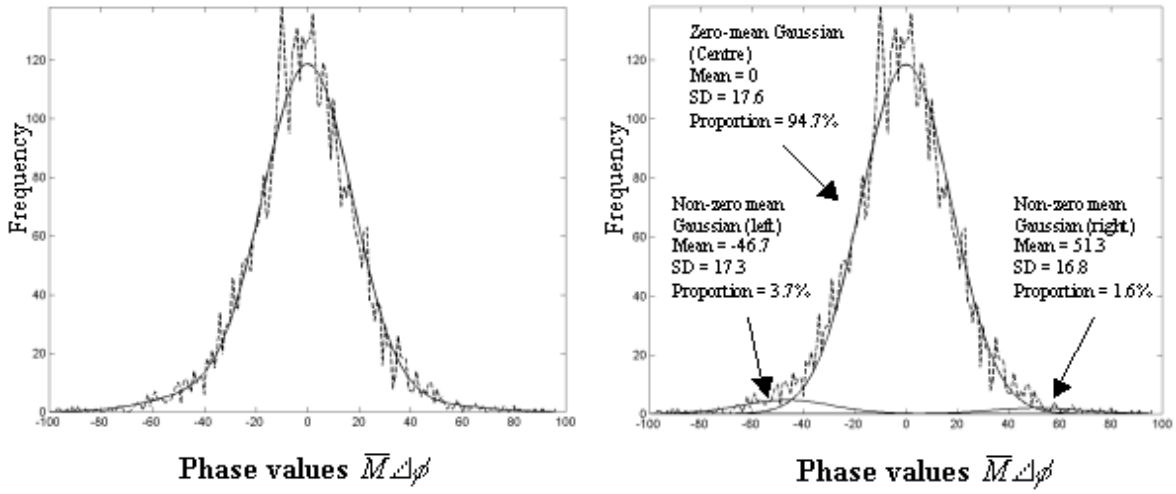

a. **b.**

Figure 2.8: *(a) The fitted distribution (solid) using one zero-mean Gaussian distribution and two opposite non-zero mean Gaussian distributions, (b) reveals the individual distributions (solid). The dashed line shows the given phase image histogram.*

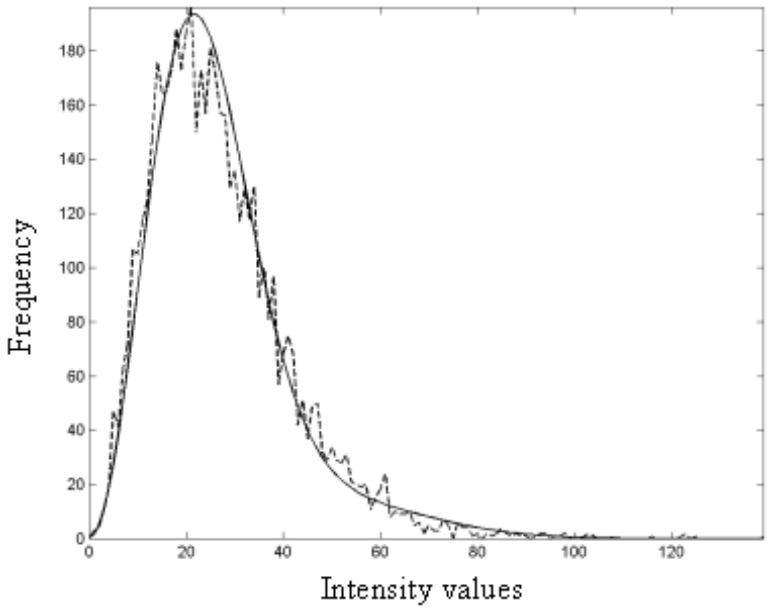

Figure 2.9: *Histogram of an MRA speed image (solid). The histogram was subsequently fitted by a Maxwell-Gaussian mixture distribution (dashed). It reveals that the Maxwell-Gaussian mixture model achieves a better fit than the Maxwell model, as shown in Figure 2.8b.*

distribution, namely a Maxwell-Gaussian-uniform (MGU) model, which is given by

$$f(i) = \underbrace{w_M f_M(i) + w_G f_G(i)}_{Background\ Signal} + \underbrace{w_U f_U(i)}_{Vascular\ Signal}, \tag{2.13}$$

where $w_M + w_G + w_U = 1$.

2.4 Parameter estimation using the Expectation-Maximisation (EM) algorithm

This section shows how we apply the EM algorithm to estimate the six parameters in the MGU model, and how we initialise these parameters based on the observed histogram of the data. The initialisation and estimation processes are fully automatic and fast, and do not require any pre-set values. Convergence is usually reached after 10-20 iterations and takes less than 1 second on a 500MHz PC. We then present the properties of the MGU model parameters.

2.4.1 EM algorithm and parameter initialisation

In Equation 2.13, the proposed mixture model has six parameters: w_M, w_G, w_U, σ_M^2, μ_G and σ_G^2, which need to be estimated. The EM algorithm can be used to estimate the parameters by maximising the log-likelihood of the mixture distribution at each iteration [10]. The update equations can be derived as shown in Appendix B. The update equations and posterior probabilities at the k^{th} iteration are summarised for each distribution as follows. For the **Maxwell (M) distribution**,

$$w_M^{k+1} = \frac{1}{n} \cdot \sum_i h(i) \cdot p^k(M|i) \quad \text{and} \tag{2.14}$$

$$(\sigma_M^2)^{k+1} = \frac{\sum_i h(i) \cdot p^k(M|i) \cdot i^2}{3 \cdot \sum_i h(i) \cdot p^k(M|i)}, \tag{2.15}$$

where n represents the total number of voxels, $h(i)$ denotes the observed histogram distribution, the intensity i ranges from 0 to I_{max} and

$$p^k(M|i) = \frac{w_M^k f_M^k(i)}{f^k(i)}. \tag{2.16}$$

For the **Gaussian (G) distribution**,

$$w_G^{k+1} = \frac{1}{n} \cdot \sum_i h(i) \cdot p^k(G|i) \quad \text{and} \tag{2.17}$$

$$\mu_G^{k+1} = \frac{\sum_i h(i) \cdot p^k(G|i) \cdot i}{\sum_i h(i) \cdot p^k(G|i)} \quad \text{and} \tag{2.18}$$

$$(\sigma_G^2)^{k+1} = \frac{\sum_i h(i) \cdot p^k(G|i) \cdot (i - \mu_G^{k+1})^2}{\sum_i h(i) \cdot p^i(G|i)}, \tag{2.19}$$

where

$$p^k(G|i) = \frac{w_G^k f_G^k(i)}{f^k(i)}. \tag{2.20}$$

For the **uniform (U) distribution**,

$$w_U^{k+1} = \frac{1}{n} \cdot \sum_i h(i) \cdot p^k(U|i), \tag{2.21}$$

where

$$p^k(U|i) = \frac{w_U^k f_U^k(i)}{f^k(i)} \quad \text{and} \tag{2.22}$$

$$f_U^k(i) = \frac{1}{I_{max}}. \tag{2.23}$$

In our implementation, the initial parameter estimates were found automatically. Let $h(i)$, $h_M^{init}(i)$ and $h_G^{init}(i)$ be the observed, initial Maxwell and initial Gaussian histograms respectively. The initial standard deviation σ_M^{init}, as described in Section 2.3.4, is set to $\frac{I_{peak}}{\sqrt{2}}$. The initial histogram of the Maxwell distribution is then given by

$$h_M^{init}(i) = C \cdot f_M(i|\sigma_M^{init}), \tag{2.24}$$

where

$$C = \frac{e \cdot \sqrt{\pi}}{4} \cdot h(I_{peak}) \cdot I_{peak} \tag{2.25}$$

to ensure that $h_M^{init}(I_{peak})$ has the same height as $h(I_{peak})$, as shown in Figure 2.10. Let A_M be the area of $h(i)$ covered by $h_M^{init}(i)$, and A_{total} be the total area covered by $h(i)$. Then, w_M^{init} is defined as the ratio of A_M to A_{total}, i.e.

$$w_M^{init} = \frac{A_M}{A_{total}}. \tag{2.26}$$

The residual histogram $h_{res}(i)$ is computed as:

$$h_{res}(i) = abs(h(i) - h_M^{init}(i)) \cdot u(i - I_{peak}), \tag{2.27}$$

where $u(i - I_{peak})$ is a step function[2]. The initial mean and standard deviation of the Gaussian distribution, μ_G^{init} and σ_G^{init}, are obtained from the 95% HPD interval of $h_{res}(i)$, where HPD

[2]The purpose of using a step function is, for the robustness of the method, to ensure that the mean of the Gaussian distribution is always larger than the peak of the Maxwell distribution.

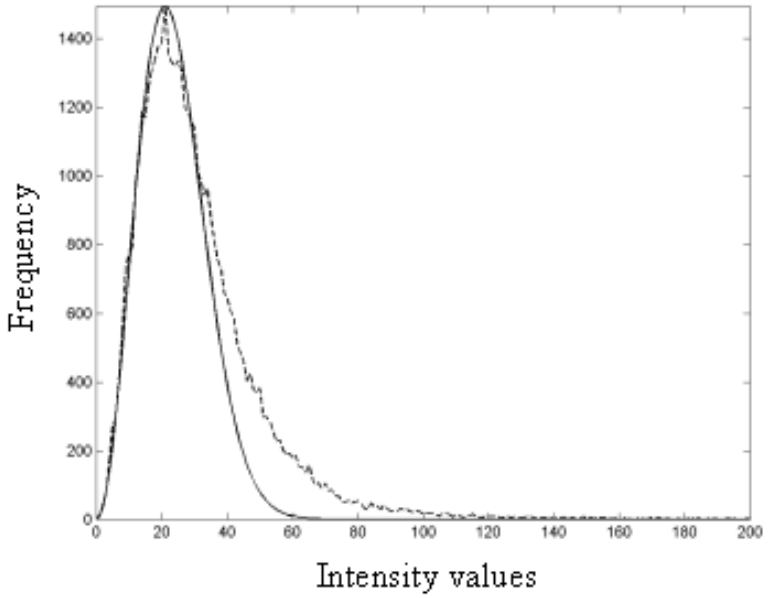

Figure 2.10: *The observed histogram $h(i)$ (dashed) and the initial histogram of the Maxwell distribution $h_M^{init}(i)$ (solid).*

interval stands for the Highest Posterior Density interval representing most (95%) of the mass of the distribution [12] and helps to avoid the influence of the long (relatively small) tail of $h_{res}(i)$ on the estimations of mean and standard derivation. The initial histogram of the Gaussian distribution is given by

$$h_G^{init}(i) = C' \cdot f_G(i|\mu_G^{init}, \sigma_G^{init}), \tag{2.28}$$

where

$$C' = \sqrt{2\pi} \cdot h_{res}(\mu_G^{init}) \cdot \sigma_G^{init} \tag{2.29}$$

to ensure that $h_G^{init}(\mu_G^{init})$ has the same height as $h_{res}(\mu_G^{init})$, as shown in Figure 2.11. Let A_G be the area of $h_{res}(i)$ covered by $h_G^{init}(i)$. Again, w_G^{init} is defined as the ratio of A_G to A_{total}, i.e.

$$w_G^{init} = \frac{A_G}{A_{total}}. \tag{2.30}$$

Finally,

$$w_U^{init} = 1 - w_M^{init} - w_G^{init} \quad \text{if} \quad w_M^{init} + w_G^{init} < 1. \tag{2.31}$$

Otherwise, in order to maintain the robustness of the method, w_M^{init}, w_G^{init} and w_U^{init} are set to empirically obtained values, e.g. $w_M^{init} = 0.91$, $w_G^{init} = 0.08$ and $w_U^{init} = 0.01$. Convergence

of the EM algorithm is generally reached after about 10-20 iterations when the changes of all estimated parameters are less than 1%.

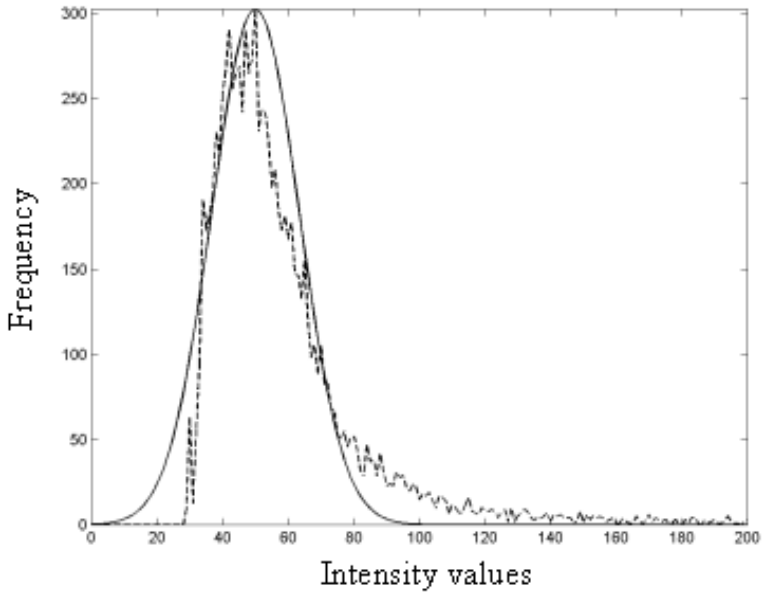

Figure 2.11: *The observed histogram $h_{res}(i)$ (dashed) and the initial histogram of the Gaussian distribution $h_G^{init}(i)$ (solid).*

2.4.2 Properties of the MGU model parameters

This section investigates the properties of the six MGU model parameters, w_M, w_G, w_U, σ_M, μ_G and σ_G, across the PC-MRA slices of a geometrically accurate straight tube with an 8mm diameter. The tube was scanned using the PC-MRA protocol on a 1.5T GE MR scanner at the Department of Clinical Neuroscience, King's College, London. The data volume size was $256 \times 256 \times 20$ voxels with a voxel dimension of $0.625 \times 0.625 \times 1.3mm^3$. The flow rate was constant and set at $300mms^{-1}$. Figures 2.12a and 2.12b show two cropped PC-MRA images with the same area (31x80 voxels in a slice). With these two data sets (one is pure background and the other has vessel voxels in the images), the changes in parameter values can be compared. Figure 2.12a shows the background region, while Figure 2.12b shows a cross-section of the tube.

The EM algorithm was first applied to the background data set. Figure 2.13 shows the variations of parameter values across the twenty PC-MRA slices. The average values are

a. *Background region.*
Maximum intensity = 171.

b. *Cross-section of a tube.*
Maximum intensity = 1591.

Figure 2.12: *Two PC-MRA images with the same area for comparing changes in parameter values when there are some vessels in the image.*

as follows: $(w_M, w_G, w_U, \sigma_M, \mu_G, \sigma_G) = (0.910 \pm 0.075, 0.081 \pm 0.075, 0.009 \pm 0.005, 30.177 \pm 1.183, 83.344 \pm 10.925, 15.052 \pm 5.584)$. Figure 2.13a shows that the weights for the background region ($w_M + w_G = 0.991$) and vessel region ($w_U = 0.009$) are almost constant. Figure 2.13b shows that the standard deviation of the Maxwell distribution, σ_M, is consistent across slices with an average value of 30.177. Figures 2.13c and 2.13d, shows the variations of the mean and standard deviation of the Gaussian distribution, μ_G and σ_G, across the slices with an average small weight, $w_G = 0.08$, assigned to the Gaussian distribution.

In order to study the changes in parameter values when there are vessel voxels in the image. The EM algorithm was applied to the data set in Figure 2.12b. The average values found in this case were as follows. $(w_M, w_G, w_U, \sigma_M, \mu_G, \sigma_G) = (0.796 \pm 0.091, 0.157 \pm 0.090, 0.047 \pm 0.002, 28.260 \pm 1.593, 83.453 \pm 11.263, 18.906 \pm 3.443)$. Figure 2.14 shows the values of weights across slices. Comparing to the parameters obtained above when there is no vessel voxel, it is observed that the weight for vessel w_U is almost constant across slices and has been increased because of the presence of vessel voxels in the dataset. Observe that the behaviour of w_M and w_G are complementary in order to maintain an approximately constant weight for the background histogram (Maxwell + Gaussian) across slices. Also, the standard deviation of the Maxwell distribution (σ_M) are almost constant (Figure 2.14b) and comparable to that when there is no vessel voxel in the dataset (Figure 2.13b). Finally, Figures 2.14c and 2.14d show the variations of the mean μ_G and standard deviation σ_G of the Gaussian distribution.

2.5 Comparing the MGU and Maxwell-uniform (MU) models

This section compares the new MGU model with the MU model in terms of the qualities of histogram fitting and segmentation.

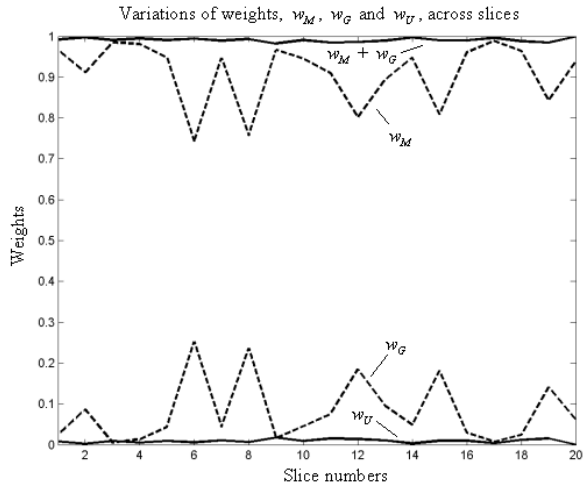

a. *Weights for the Maxwell (M), Gaussian (G) and uniform (U) distributions respectively.* $w_M + w_G + w_U = 1$. *Average values are* $w_M = 0.910 \pm 0.075$, $w_G = 0.081 \pm 0.075$ *and* $w_U = 0.009 \pm 0.005$.

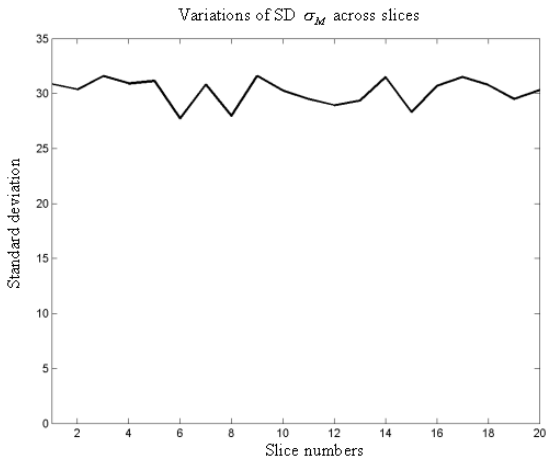

b. *Standard deviation of the Maxwell distribution. Average value is* $\sigma_M = 30.177 \pm 1.183$.

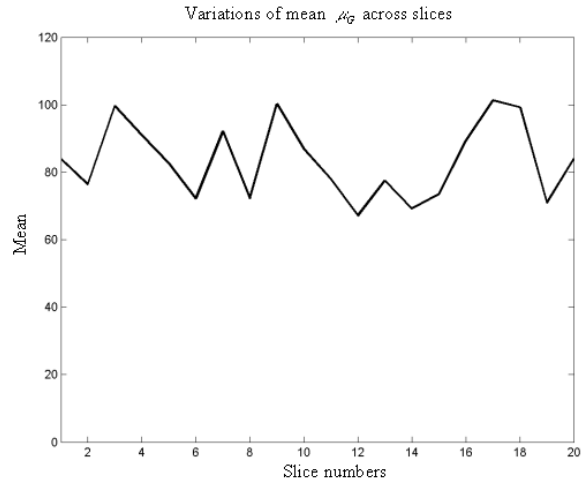

c. *Mean of the Gaussian distribution. Average value is* $\mu_G = 83.344 \pm 10.925$.

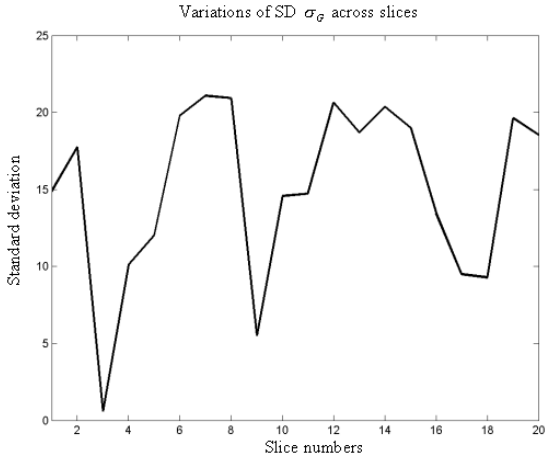

d. *Standard deviation of the Gaussian distribution. Average value is* $\sigma_G = 15.052 \pm 5.584$.

Figure 2.13: *Variations of MGU model parameters across slices for the background region.*

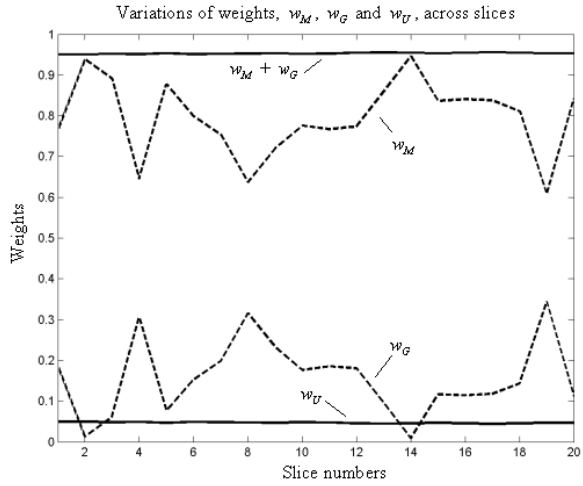

a. *Weights for the Maxwell (M), Gaussian (G) and uniform (U) distributions respectively.* $w_M + w_G + w_U = 1$. *Average values are* $w_M = 0.796 \pm 0.091$, $w_G = 0.157 \pm 0.090$ *and* $w_U = 0.047 \pm 0.002$.

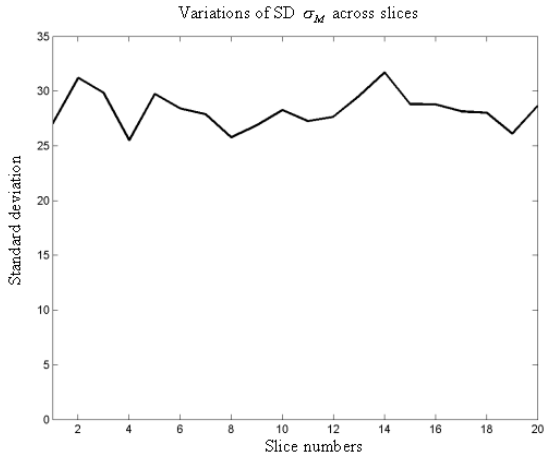

b. *Standard deviation of the Maxwell distribution. Average value is* $\sigma_M = 28.260 \pm 1.593$.

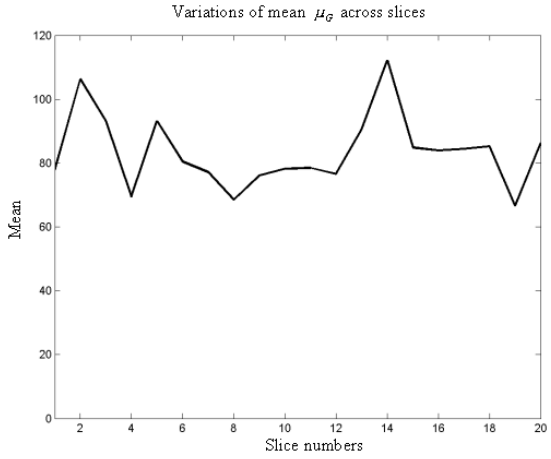

c. *Mean of the Gaussian distribution. Average value is* $\mu_G = 83.453 \pm 11.263$.

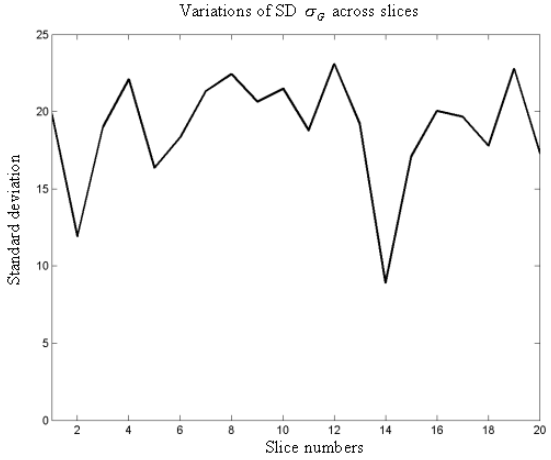

d. *Standard deviation of the Gaussian distribution. Average value is* $\sigma_G = 18.906 \pm 3.443$.

Figure 2.14: *Variations of MGU model parameters across slices with a tube filled with constant flowing fluid at the middle of the images.*

2.5.1 Quality of histogram fitting

The first comparison looks at the difference between MU and the proposed MGU models for describing the statistical characteristics of signal in MRA speed images. Intracranial scans (PC-MRA) of two patients were performed using a 1.5T GE MR scanner at the Department of Clinical Neuroscience, King's College London. The scan volume was $256 \times 256 \times 28$ voxels with a voxel size about $0.8 \times 0.8 \times 1mm^3$ (details of the scans are given in Section 6.4.1). The comparison of the proposed MGU model with the previously reported MU model was based on the absolute difference error for all slices (28 slices) in the two scans, where the absolute difference error is defined as

$$\text{Absolute difference error} = \frac{\sum_{i=0}^{I_{max}} |hist_m(i) - hist_o(i)|}{\sum_{i=0}^{I_{max}} hist_o(i)} \times 100\%, \tag{2.32}$$

where $hist_m$ represents the histogram estimated by using the MGU model or MU model, and $hist_o$ represents the histogram observed from a given data set. Results are plotted in Figures 2.15a and 2.15b. The Maxwell-Gaussian mixture model produced significantly better histogram fits than the Maxwell model for describing the background signal in PC-MRA speed images, reducing the absolute difference error by an average of 13%.

2.5.2 Quality of segmentation

A typical result of histogram fitting on a clinical MRA speed image with the MGU model is shown in Figure 2.16. For comparison, a MU mixture model fitted using the EM algorithm is shown in Figure 2.17, which reveals that the Maxwell model provides a poorer fit than the Maxwell-Gaussian mixture model for background signal. It is also worth noting that, in practice, the imperfection of the Maxwell background signal model, is exaggerated by ghosting artifacts and partial volume effect in the clinical data.

Given an estimated mixture model, a PC-MRA speed image can be segmented statistically on the basis of the MAP (Maximum *A-Posteriori*) criterion. Assuming that the weights (or prior probabilities) remain constant, then, using the MAP criterion, a voxel $x_j \in \{0, 1\}$, where $j = \{1, \ldots, n\}$, $x_j = 1$ and $x_j = 0$ denote vessel and background respectively, is classified as a vessel voxel when the vessel probability $w_U f_U(i)$ is greater than the background probability $w_M f_M(i) + w_G f_G(i)$. Therefore, a threshold can be found by seeking the intersection of the background and vessel probability distributions. As indicated by the arrows in Figures 2.16 and 2.17, the threshold t_{MGU} found by using the MGU model is higher than the threshold

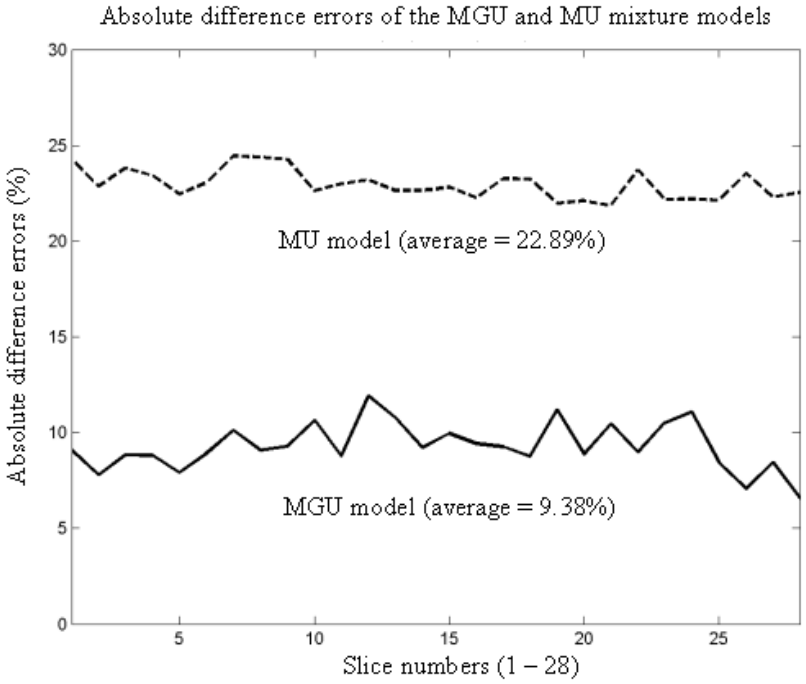

a. *Patient 1.*

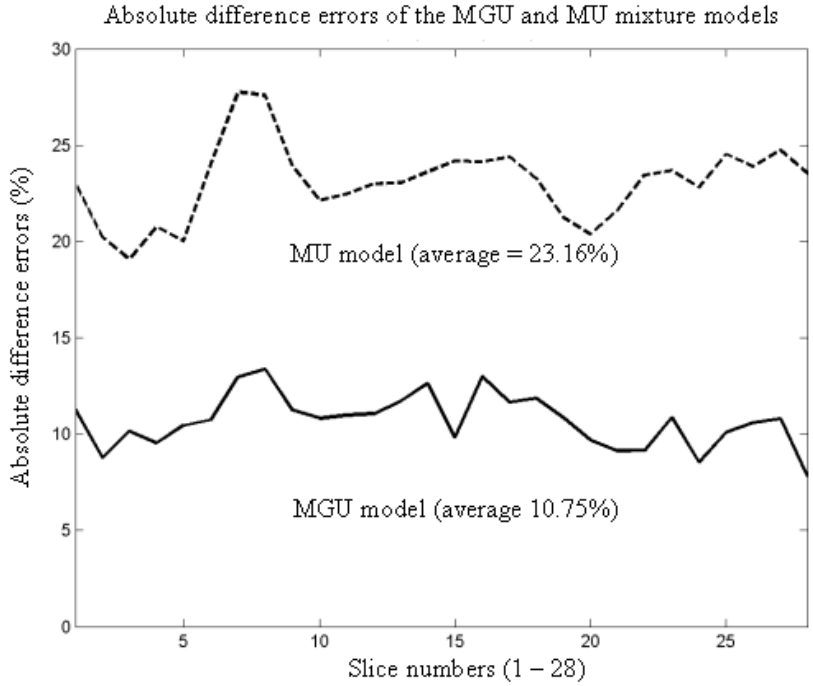

b. *Patient 2.*

Figure 2.15: *The MU model (dashed) was compared with the proposed MGU model (solid) by computing the absolute difference error for all slices in the two scans. This shows that the MGU model is better than the MU model for describing the background signal in PC-MRA speed images by an average of 13%.*

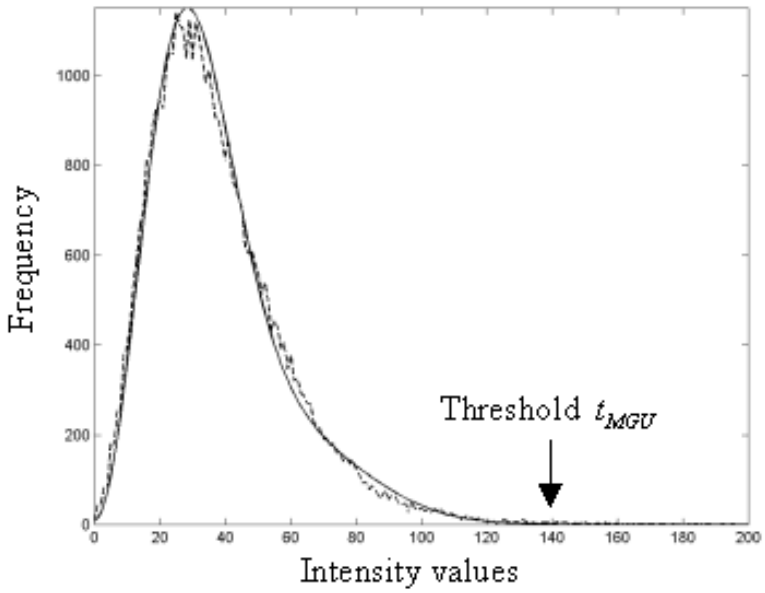

Figure 2.16: *Histogram of an MRA speed image (dashed) and the Maxwell-Gaussian-uniform (MGU) mixture model (solid). The threshold t_{MGU} found by using the MGU model is usually higher than the threshold t_{MU} found by using Maxwell-uniform (MU) mixture model. (as compared with Figure 2.17).*

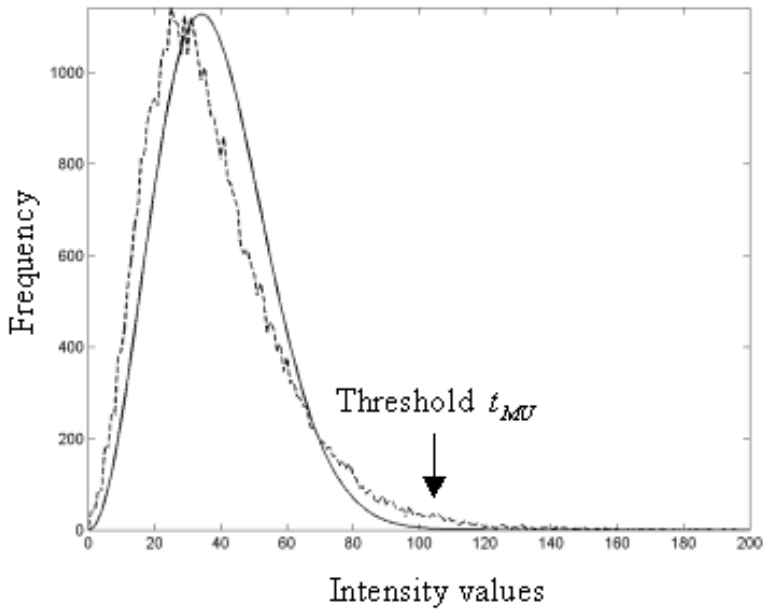

Figure 2.17: *Histogram of an MRA speed image (dashed) and the Maxwell-uniform (MU) mixture model (solid).*

t_{MU} found by using the already defined MU model. As shown in Figures 2.18a and 2.18b, fewer false positive voxels (misclassified vessel voxels) will be detected if the threshold t_{MGU} rather than t_{MU} is used in the segmentation process (the original MRA speed image is shown in Figure 2.6a). As such, the threshold t_{MGU} found by using the MGU model tends to be more correct.

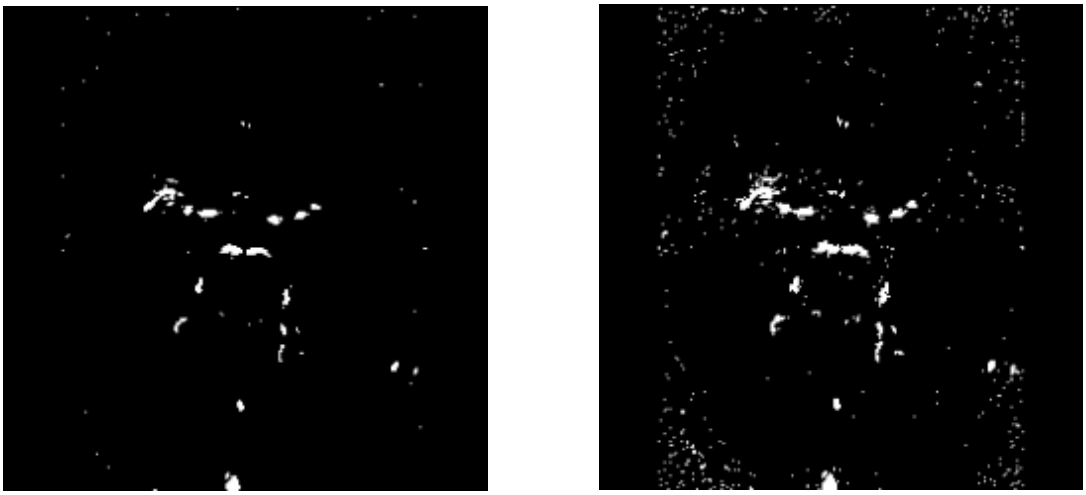

a. **b.**

Figure 2.18: *(a) A segmented image using a threshold t_{MGU} found by employing the MGU model. (b) A segmented image using a threshold t_{MU} found by employing the MU model. These figures show fewer false positive voxels (misclassified vessel voxels) detected when threshold t_{MGU} is used in the segmentation process (the original MRA speed image is shown in Figure 2.6a).*

2.6 Problem of segmentation based on speed information alone

Figures 2.19a and 2.19b show an MRA speed image and a binary-segmented image produced using the MGU model in a MAP classification method. The aneurysm is indicated by an arrow in the figure. The overall segmentation is good, except for the regions inside the aneurysm. Note that the resulting segmentation inside an aneurysm is adversely affected by the significant signal loss seen in the speed images. This results from low or complex flow within the aneurysm which causes some of the intensity values to drop as low as those of the background voxels. Consequently, the distinction between background and vessel voxels cannot be made on the basis of statistical treatment of the intensity values. This signal loss

phenomenon is common in large aneurysms and regions of low flow rate. Similar results are obtained in a second aneurysm shown in Figures 2.20a and 2.20b. We will discuss in detail how to overcome this problem in Chapter 4.

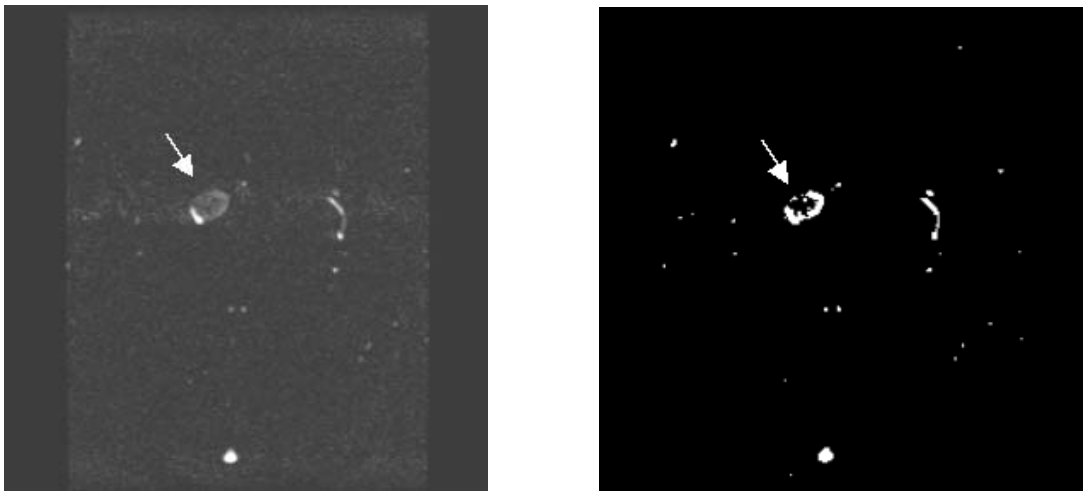

a. **b.**

Figure 2.19: *Patient 1: (a) An MRA speed image and (b) a binary-segmented image produced using the Maxwell-Gaussian-uniform (MGU) mixture model and a MAP classification method. The aneurysm is indicated by an arrow in the figure. It is noted that the resulting segmentation is adversely affected by the significant signal loss towards the centre of the aneurysm.*

2.7 Summary

In this chapter, we have derived a Maxwell-Gaussian-uniform mixture (MGU) model for modelling the background and vascular signal statistical characteristics of PC-MRA images generated by a phase-difference PC-MRA post-processing algorithm. The parameters of the MGU model were estimated automatically by using the Expectation-Maximisation (EM) algorithm, for which update equations were derived.

Experiments have been carried out on phantom and clinical images to illustrate the applicability of the MGU model, and show that the MGU model (a) fits better than the conventional Maxwell-uniform (MU) distribution the PC-MRA signal distribution, and (b) gives fewer false positive (misclassified as vessel) voxels in segmentation.

The experimental results further show that the overall segmentation is satisfactory. It should be pointed out that slow or complex flow can lead to low signal intensities in the

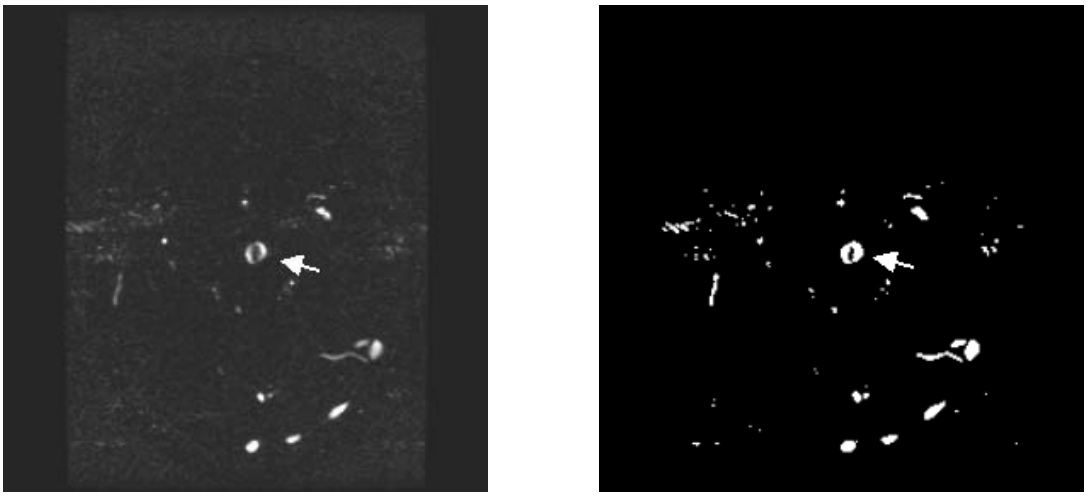

a. **b.**

Figure 2.20: *Patient 2.*

speed image, especially inside the aneurysm. This affects the segmentation result in these regions because the intensity values drop to almost the same level as the background (tissue) voxels. This lowers the SNR values and makes the vessel voxels hard to distinguish from the background voxels. Because vessels and aneurysms differ in shape and size, it is difficult to develop a simple but effective morphological means to improve segmentation. Rather than relying on the speed information alone, the available but unused information will be used to overcome this problem.

In the following chapters we propose to address this problem by introducing a "flow coherence" measure into the image segmentation process. This measure is introduced in the next chapter and explored in the context of a new image segmentation method in Chapter 4.

Chapter 3

Local phase coherence (LPC) measure

3.1 Introduction

As discussed in the previous chapter, the overall segmentation based on the proposed physics based statistical model (MGU model) is satisfactory (Quantitative comparisons will be presented in Section 4.4.3). However, the quality of the statistical segmentation will be affected by the significant signal loss due to the low flow or complex flow inside the vasculature. This leads to the incorporation of directional information, provided by the PC-MRA protocol, in the segmentation process so that the segmentation quality can be increased. In this chapter, we propose a new coherence measure to quantify locally coherent flow patterns, which is named the *local phase coherence* (LPC), and is extremely helpful in distinguishing locally coherent flow fields from (non-coherent) random flow fields. We hypothesise that this measure will be very useful for flow discontinuity and vessel detection, flow feature extraction. The application to vessel detection is explored in more detail in Chapter 4.

In Section 3.2, we briefly review related coherence measurements based on: (a) the deviation of vector directions from their mean vector [73] and (b) the ratio of the length of the net flow vectors to the total vector length [43, 81]. We show that these two apparently different measures are similar and in fact are related by a simple non-linear relationship. Conceptually, within a given window, these measures compute the "dispersion" of flow vector directions, and assign higher values to locally coherent flow patterns and lower values to random flow patterns. However, *one drawback is that these measures assume that flow vectors are spatially*

independent of each other, making them incapable of unambiguously capturing information about the spatial correlations of flow vectors. This can lead to an inherent ambiguity in coherence values because the same coherence value can be assigned to two different groups of flow vectors having the same orientation distribution, but with a different spatial arrangement.

In Section 3.3, to overcome this deficit, we introduce a new concept of spatial dependence between flow vectors in the local coherence measure, which is similar to the idea of enhancing spatial relationship (co-occurrence matrix) in texture analysis [35]. We then present a formal definition of the LPC measure based on the dot products of the neighbouring flow vectors within a window. This measure describes how the flow vectors cohere with each other, and more importantly incorporates the spatial dependence between the flow vectors explicitly.

In Section 3.4, we use synthetic images to evaluate and compare the performance of the LPC measure and the related coherence measures. Specifically, we compute the coherence maps for the synthetic images using the different coherence measures, perform segmentation between coherent and random regions, and measure the segmentation error. We find that (a) the LPC measure is more robust to noise than other coherence measures, and also (b) when the SNR is low, segmentation using the LPC measure gives a more accurate segmentation result for distinguishing coherent regions from random regions than a segmentation using speed information alone, as described in Chapter 2. In Section 3.5, we demonstrate the applicability of the proposed LPC measure for enhancing locally coherent vessel voxels in phantom and clinical images. Conclusions are presented in Section 3.6.

3.2 Related coherence measures

This section briefly reviews previously proposed and related coherence measurements based on: (a) the deviation of vector directions and (b) the ratio of the length of the net flow vectors to the total vector length, and discusses the differences and similarities between the two different coherence measurements.

3.2.1 Measurement based on deviation of vector directions

Given a group of flow vectors, $V \in \{v_1, ..., v_N\}$, where $v_i = (v_i^x, v_i^y, v_i^z)^T$, it is natural to evaluate their flow coherence by finding their mean vector and measuring the deviation (or the 'spread') of vector directions from the mean vector. Rao and Jain [73] suggested projecting

the flow vectors onto the mean vector using the dot-product operation. This leads to the coherence measure CM_{dev} defined as,

$$CM_{dev} = \frac{\sum_{i \in W} v_i \cdot \bar{v}}{\sum_{i \in W} ||v_i||}, \tag{3.1}$$

where v_i represents any vector inside a window W and $\bar{v}$ represents the mean vector, which is given by

$$\bar{v} = \frac{\sum_{i \in W} v_i}{N}, \tag{3.2}$$

where N is the number of flow vectors inside the window W. It is noted that v_i are normalised vectors, i.e. $||v_i|| = 1$, for $i = 1 \ldots N$, because it is intended to measure the directional information alone [73]. Another reason for normalising the vectors is to avoid any vector with relatively large magnitude dominating the local coherence measurement. From Equations 3.1

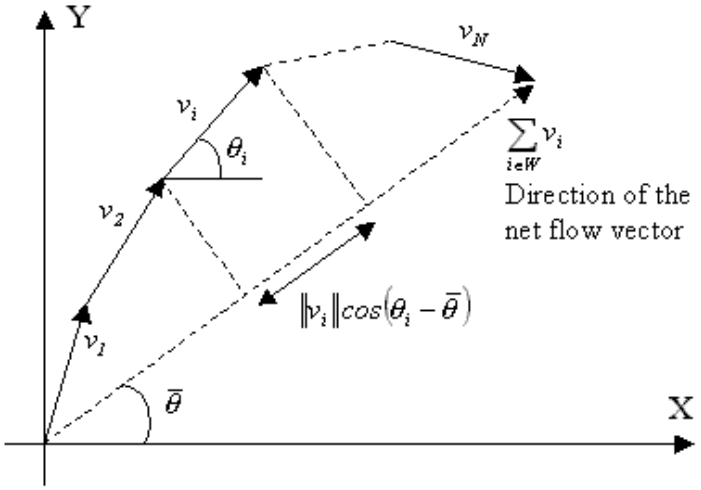

Figure 3.1: *This figure shows that the length of the net flow vector* $\sum_{i \in W} v_i$ *is the sum of the projections* $\sum_{i \in W} ||v_i|| \times cos(\theta_i - \bar{\theta})$ *of all individual vectors* v_i *onto the direction of the net (mean) flow vector, where* $||v_i|| = 1$ *and* N *is the number of vectors in a window* W*.*

and 3.2, the coherence measure CM_{dev} can be rewritten as

$$CM_{dev} = \frac{1}{\sum_{i \in W} ||v_i||} \sum_{i \in W} \frac{||\sum_{j \in W} v_j||}{N} \times cos(\theta_i - \bar{\theta}), \tag{3.3}$$

where θ_i and $\bar{\theta}$ represent the orientation of any flow vector v_i and the mean vector $\bar{v}$ respectively, as shown in Figure 3.1 (although the flow vectors are inherently in 3D, they are plotted in 2D for illustration only). It is also shown in Figure 3.1 that the length of the net flow

vector $\sum_{i\in W} v_i$ is the sum of the projections $\sum_{i\in W} ||v_i|| \times cos(\theta_i - \bar{\theta})$ of all individual vectors v_i onto the direction of the net flow vector, where $||v_i|| = 1$ and N is the number of vectors in a window W. Hence, $||\sum_{j\in W} v_j|| = \sum_{i\in W} cos(\theta_i - \bar{\theta})$ in Equation 3.3. Since vectors are normalised, then $\sum_{i\in W} ||v_i|| = N$. The coherence measure CM_{dev} can be re-expressed as

$$CM_{dev} = \frac{||\sum_{i\in W} v_i||^2}{N^2}, \tag{3.4}$$

which is bounded by a range between 0 and 1, i.e. $CM_{dev} \in [0 \dots 1]$

3.2.2 Measurement based on ratio of the length of the net flow vectors to the total vector length

Another approach to measuring flow coherence was proposed by Summers et al. [81]. The coherence measure is defined as

$$CM_{ratio} = \frac{||\sum_{i\in W} v_i||}{\sum_{i\in W} ||v_i||}, \tag{3.5}$$

where v_i represents a normalised vector inside a window W. The coherence measure CM_{ratio} represents the ratio of the length of the net flow vectors to the total vector length. Since vectors are normalised, the coherence measure CM_{ratio} can be rewritten as

$$CM_{ratio} = \frac{||\sum_{i\in W} v_i||}{N}, \tag{3.6}$$

which is bounded by a range between 0 and 1, i.e. $CM_{ratio} \in [0 \dots 1]$.

It is clear, from Equations 3.4 and 3.6, that the two apparently different coherence measures, CM_{dev} and CM_{ratio}, are related non-linearly by

$$CM_{dev} = (CM_{ratio})^2. \tag{3.7}$$

This relationship is illustrated in Figure 3.2, which shows that CM_{ratio} shows a greater sensitivity to low coherence than CM_{dev}, giving a high-pass-filter effect. Therefore, in theory, CM_{dev} is better than CM_{ratio} because the values of coherence measure of the background random regions are suppressed relatively. This relationship will be manifested in the experimental results presented in Section 3.4.

3.3 Local phase coherence (LPC) measure

In this section, we propose a new measure, namely *local phase coherence* (LPC), to quantify the degree of coherence of local flow velocities. Although other coherence measures have

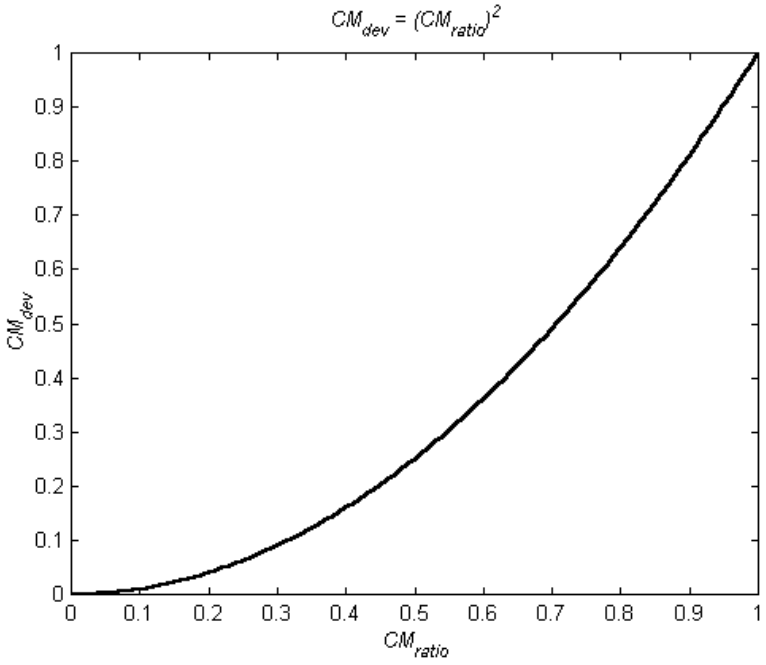

Figure 3.2: *This figure shows the relationship between* CM_{dev} *and* CM_{ratio}, $CM_{dev} = (CM_{ratio})^2$.

been proposed in earlier works, as described in the Section 3.2, little attention has been paid to treating the coherence and random flow patterns as regions of texture. A texture-based approach [34, 35] emphasises the spatial relationships (or inter-relationships) between adjacent voxels. A coherent flow texture corresponds to slight changes in the flow directions between the adjacent flow vectors in a window W, whereas a random flow texture corresponds to large changes in the flow directions between adjacent flow vectors in W. The flow direction changes can be calculated using the dot product operation between the two neighbouring flow vectors. This section begins by illustrating the problems of the lack of spatial dependence in the coherence measures and then defines the proposed LPC measure.

3.3.1 The need for the enhancement of spatial relationships

For the coherence measures CM_{dev} and CM_{ratio}, proposed in earlier work, the measures are independent of the relative positions of the flow vectors. As such, different flow patterns, with the same orientation distribution, will be given the same value of coherence. Figure 3.3 illustrates this. In this example, it can be seen that the flow pattern in Figure 3.3a

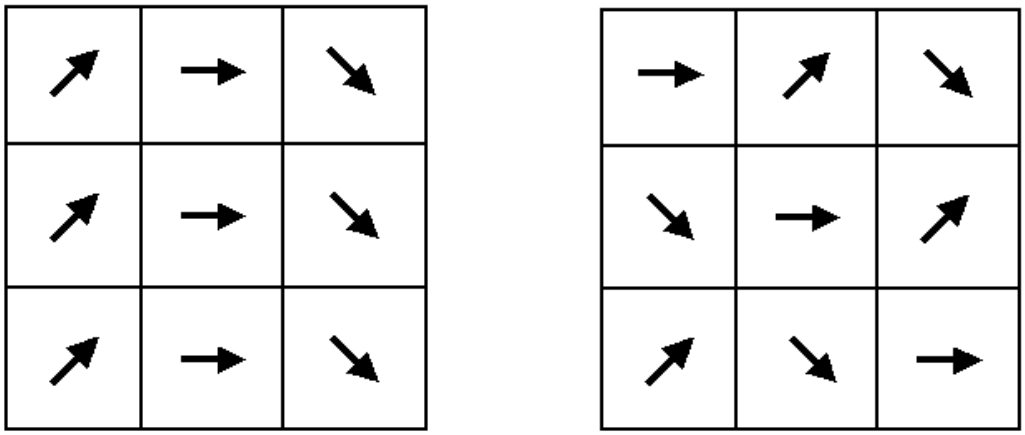

a. *More coherent and less random pattern.* **b.** *Less coherent and more random pattern.*

Figure 3.3: *This figure shows two flow patterns, where (a) is more coherent than (b). However, if we calculate the degree of coherence using CM_{dev} and CM_{ratio}, as described in the Section 3.2, we find that $CM_{dev} = 0.64$ and $CM_{ratio} = 0.8$ for both flow patterns. It reveals the deficiency of these measures in characterising the coherent and random flow patterns.*

is intuitively more coherent than the flow pattern in Figure 3.3b. However, if we examine the orientation distribution of these two patterns, we find that both patterns have the same orientation distribution consisting of (a) three flow vectors pointing toward the North East direction ($\frac{\pi}{4}$), (b) three flow vectors pointing toward East direction (zero radian), and (c) three flow vectors pointing toward South East direction ($-\frac{\pi}{4}$). These two regions differ only by having different relative positions of the vectors. If we calculate the degree of coherence using CM_{dev} and CM_{ratio}, we find that $CM_{dev} = 0.64$ and $CM_{ratio} = 0.8$, and the same value assigned for the two different flow patterns. This lack of distinction reveals the deficiency of these measures in characterising the coherent and random flow patterns.

3.3.2 Defining LPC measure

To overcome the above drawback, in this section, we propose a new coherence measure based on the use of spatial correlation. Given a window W_s with a centre on voxel s, each voxel in W_s contains a normalised vector $v = \{v^x, v^y, v^z\}^T$, indicating the flow direction, a number of pairs of adjacent vectors can be formed in W_s. The LPC measure at s is defined as the sum of dot products of these adjacent vector pairs.

Formally, we may loosely follow the notations used by Geman and Geman [28] in letting

$Z_n = \{1, \ldots, n\}$ represent a regular lattice structure with n voxels (or pixels), and n be the number of voxels in an image. Let $S = \{s_i | i \in Z_n\}$ be a set of voxels, $V = \{v_i | i \in Z_n\}$ be the corresponding set of flow vectors, and $\mathcal{N} = \{\mathcal{N}_i | i \in Z_n\}$ be a neighbourhood system for S. Let W_s be a window at voxel $s \in S$ containing a subset of voxels of S, i.e. $W_s \subset S$. The neighbourhood system at s is given by

$$\mathcal{N}_s(c) = \{s_i, s_j \in W_s \mid 0 < ||s_i - s_j||^2 \leq c\}. \tag{3.8}$$

Note that c specifies the order of the neighbourhood system. For example, when $c = 1$, it is a first-order neighbourhood system because every voxel inside W_s forms a pair with its nearest neighbour, as shown in Figure 3.4a, in which W_s is a 3x3 window mask in a slice. It becomes a second-order neighbourhood system when $c = 2$, as shown in Figure 3.4. The LPC measure is defined as

$$CM_{lpc}(c) = \sum_{s_i, s_j \in W_s, \mathcal{N}_s(c)} v_i \cdot v_j. \tag{3.9}$$

In a slice, the number of adjacent vector pairs for $c = 1$ and $c = 2$ are 12 and 20, respectively. CM_{lpc} is bounded by the size of the set $\mathcal{N}_s$, i.e. $CM_{lpc} \in [-\mathcal{N}_s, \mathcal{N}_s]$. For instance, the value range of CM_{lpc} is between -12 and 12 when $c = 1$, and -20 and 20 when $c = 2$. In this thesis, a 3x3 window mask is used in a slice (or 3x3x3 in 3D) for reasonable localisation of the measure and for the speed of computation.

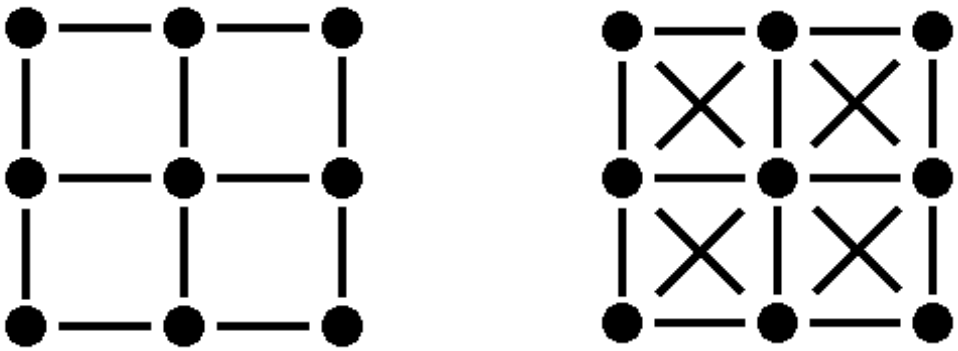

a. 1^{st} *order neigbourhood system.* **b.** 2^{nd} *order neigbourhood system.*

Figure 3.4: *The neigbourhood system* $\mathcal{N}_s$.

Having defined the LPC measure, its similarities and differences can be highlighted by comparison with the two coherence measures, CM_{dev} and CM_{ratio}. While these gave values of 0.64 (CM_{dev}) and 0.8 (CM_{ratio}) for both the examples in Figures 3.3a and 3.3b, while

the corresponding values of the LPC measure are 0.90 and 0.78 respectively when $c = 2$ and 0.92 and 0.72 respectively when $c = 1$. This implies that the LPC measure can better discriminate between the coherent flow patterns and the random flow patterns. A more detailed comparison of their performances will be presented in the next section.

3.4 Experimental results

In this section, we present the results from a number of experiments aimed at comparing the performance of the three different coherence measures, CM_{dev}, CM_{ratio} and CM_{lpc}, on synthetic images.

3.4.1 Synthetic images

There are three major advantages of using synthetic images for comparison of the performances. Firstly, the true flow pattern and the true signal-to-noise ratios (SNR) of the images is known and can be controlled for a quantitative comparison. Secondly, given that the true flow pattern is known, the histograms of individual regions can correctly represent the statistical characteristics of each region in the pattern for segmentation. This means, using the synthetic images, we can have complete knowledge about the probabilistic structure of this supervised two-category classification problem [21]. Finally, the synthetic images are always "clean" and free from image artifacts. The evaluated performance should represent the optimal performance of the coherence measures.

The synthetic images consist of two 256×256 flow patterns: (a) vertical straight tubes and (b) circular tubes with 8 and 4 pixel width, as shown in Figures 3.6a and 3.6b respectively. The typical size of PC-MRA images is 256×256 voxels and the size of vessels ranges, on average, from 8 voxels for large vessels to 4 (or even fewer) voxels for small vessels, as shown in Figure 3.5. The simulated parameters were therefore chosen to mimic the clinical case. The white strips in Figures 3.6a and 3.6b represent the positions and regions of the simulated flow, while the black strips represent the background regions. The total areas of the white and black strips are the same in each image. In Figure 3.6a, the simulated "flow" runs from the top to bottom direction, while in Figure 3.6b, it is in the clockwise direction.

For the purpose of image synthesis, we assume that each component is corrupted by Gaussian noise with zero mean and the same standard deviation σ [37]. In Figure 3.6a, the

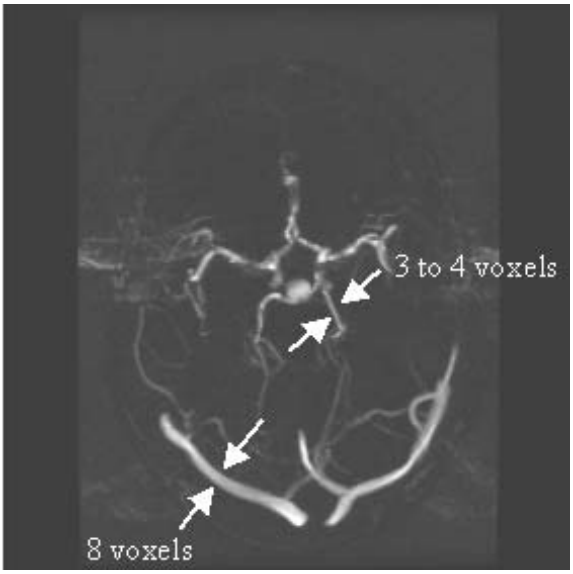

Figure 3.5: *Width of vessels.*

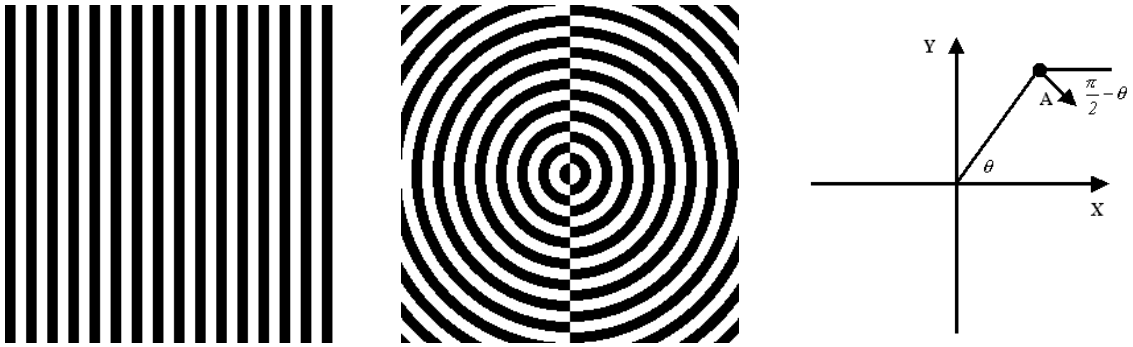

a. *Vertical straight tubes.* **b.** *Circular tubes.* **c.** *The coordinate system.*

Figure 3.6: *True patterns of the synthetic images (tubes are 8 pixel width) and the coordinate system.*

flow vector inside the tubes is given by

$$v_x = n_x, \quad v_y = -A + n_y, \quad v_z = n_z, \tag{3.10}$$

where A represents the true flow magnitude, n_x, n_y and n_z are the zero-mean Gaussian noise components with the same standard deviation σ. The flow vector in the background is given by the same set of equations, except that A is set to zero. SNR is then given by

$$SNR = \frac{A}{\sigma}, \tag{3.11}$$

where σ is set to 28 (on average, σ is found to be about 28 in the clinical PC-MRA images from our datasets). Similarly, the tube flow vector in Figure 3.6b is given by

$$v_x = A \times sin\theta + n_x, \quad v_y = -A \times cos\theta + n_y, \quad v_z = n_z, \tag{3.12}$$

where θ is defined in Figure 3.6c. The magnitude (or the speed) of the flow at each voxel is given by $m = (v_x^2 + v_y^2 + v_z^2)^{\frac{1}{2}}$. Figures 3.7a and 3.7b show the speed images of the synthetic flow patterns (SNR = 3). As with clinical practices, voxels with high flow rates are assigned intensity values higher than those assigned to the voxels with low flow rates. The histograms corresponding to these simulated images are plotted in Figures 3.7c and 3.7d respectively. The background distributions overlap heavily with those of the tubes because of the low SNR (SNR=3). Segmentation was then performed using the MAP (Maximum *A-Posteriori*) method on the histograms of vessel and background voxels in the speed images [21], which chose the intersections of the histograms as the threshold. Figures 3.7e and 3.7f show that, when the SNR is low, segmentation results based on the speed information alone are not very encouraging.

3.4.2 Error measurements and results

Given that the true pattern is known, the segmentation (or classification) error can be accurately calculated by counting the number of misclassified pixels, which is given by

$$\text{Segmentation error} = \frac{\text{Number of misclassified pixels}}{\text{Total number of pixels in the image}} \times 100\%. \tag{3.13}$$

The segmentation errors of the speed images (SNR = 3), as shown in Figures 3.7e and 3.7f, using the speed information (histograms) alone are 15.08% and 14.86% for the vertical straight tubes and circular tubes respectively. The high segmentation error rates reveal that segmentation using speed information alone is inadequate when the SNR is low.

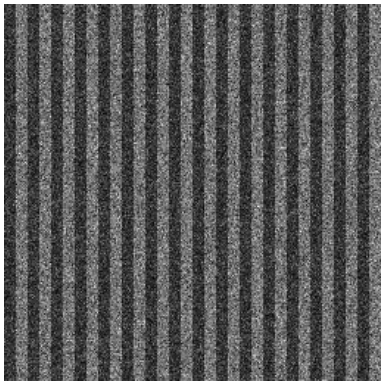

a. *Speed image.*

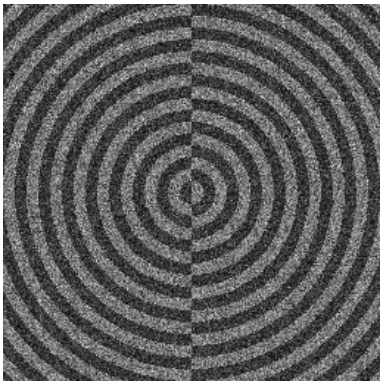

b. *Speed image.*

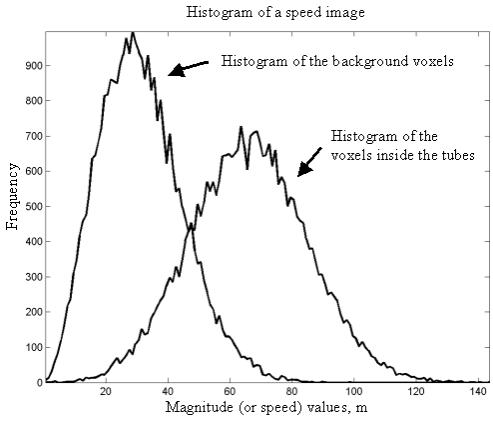

c. *Speed image histogram (vertical tubes).*

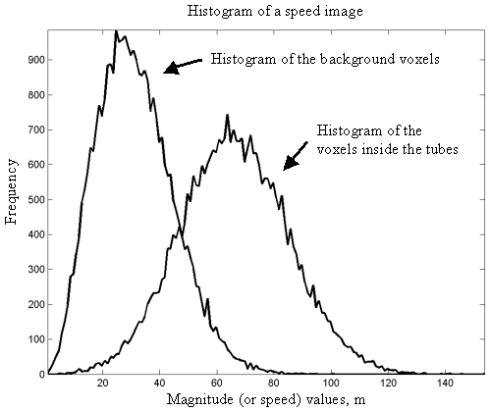

d. *Speed image histogram (circular tubes).*

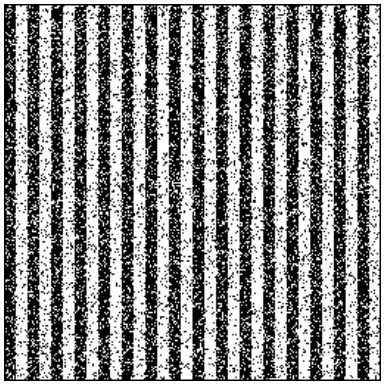

e. *Segmented image using speed information alone. Segmentation error = 15.08%.*

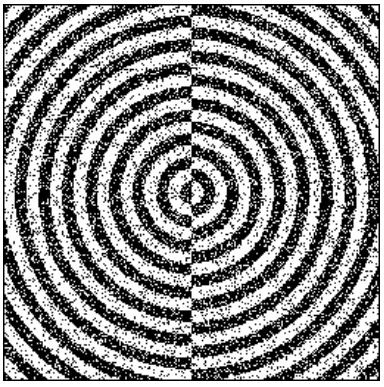

f. *Segmented image using speed information alone. Segmentation error = 14.86%.*

Figure 3.7: *Speed images of the synthetic flow patterns (SNR = 3, tubes were 8 pixel width), their histograms and segmented images using speed information alone.*

Segmentation based on the four different coherence measures were compared: CM_{dev} (Equation 3.1), CM_{ratio} (Equation 3.6), $CM_{lpc}(c = 1)$ and $CM_{lpc}(c = 2)$ (Equation 3.9). For each coherence measure, e.g. $CM_{lpc}(c = 2)$, the coherence maps for the two synthetic images (vertical and circular tubes) were calculated on a voxel-by-voxel basis. Examples for $CM_{lpc}(c = 2)$ are shown in Figures 3.8a and 3.8b. We then generated histograms of the background and tube regions from each of the corresponding coherence maps, as plotted in Figures 3.8c and 3.8d for $CM_{lpc}(c = 2)$. The background and tube histograms were then used for thresholding the coherence maps using the MAP classification method. The thresholded images for $CM_{lpc}(c = 2)$ are shown in Figures 3.8e and 3.8f. It is observed that these two thresholded images match the true flow patterns (Figures 3.6a and 3.6b) better than the segmented images obtained using speed information alone (Figures 3.7e and 3.7f). Specifically, the segmentation errors are 3.71% and 4.84% for the vertical straight tubes and circular tubes respectively. Compared to the segmentation errors using speed information alone (15.08% for vertical tubes and 14.86% for circular tubes), it is clear that segmentation using flow coherence information gives a higher segmentation accuracy when the SNR is low. For the sake of comparison, Table 3.1 gives the segmentation errors of $CM_{lpc}(c = 2)$, $CM_{lpc}(c = 1)$, CM_{ratio} and CM_{dev}, and reveals that CM_{lpc} gives smaller segmentation error than CM_{ratio} and CM_{dev}.

Tube types	$CM_{lpc}(c = 2)$	$CM_{lpc}(c = 1)$	CM_{ratio}	CM_{dev}
Vertical	3.71%	4.02%	6.47%	6.30%
Circular	4.84%	5.25%	6.23%	6.29%

Table 3.1: Segmentation errors of $CM_{lpc}(c = 2)$, $CM_{lpc}(c = 1)$, CM_{ratio} and CM_{dev}

It is interesting to see that the segmentation errors change significantly when the SNR increases (from SNR = 2 to SNR = 7). The segmentation errors of the four different coherence measures are plotted in Figure 3.9. Figure 3.9 shows the transition from (a) when the SNR was low, the quality of segmentation using flow coherence information is better than that using speed information alone; to (b) when the SNR was high, segmentation using speed information alone is better than that using flow coherence information.

The two major behaviours seen in segmenting these images may be understood as follows. Firstly, speed histograms overlap heavily when the SNR is low, making the MAP segmentation

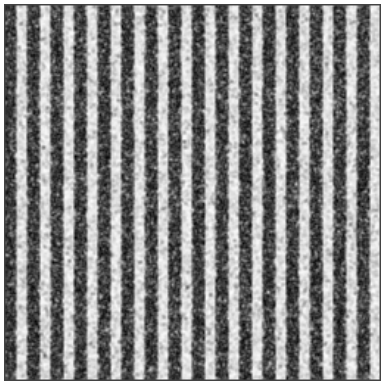

a. *Map of coherence $CM_{lpc}(c = 2)$ of the vertical straight tubes.*

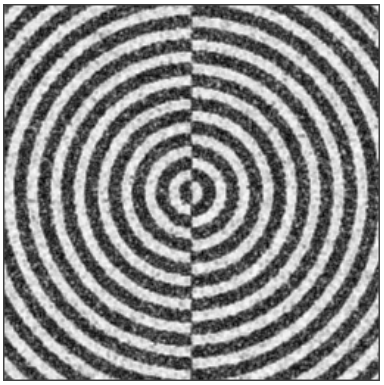

b. *Map of coherence $CM_{lpc}(c = 2)$ of the circular tubes.*

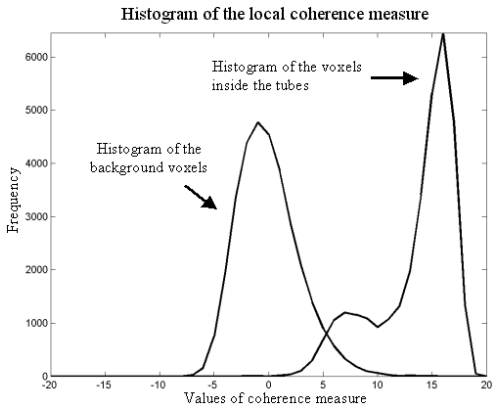

c. *Histogram of $CM_{lpc}(c = 2)$.*

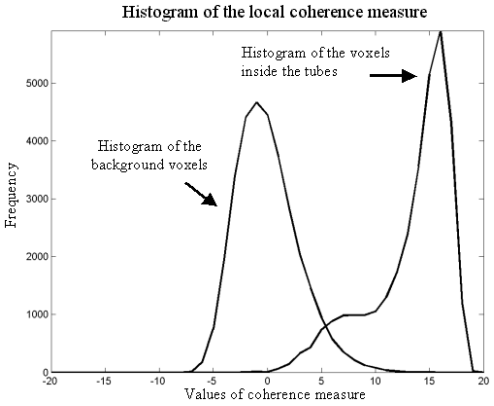

d. *Histogram of $CM_{lpc}(c = 2)$.*

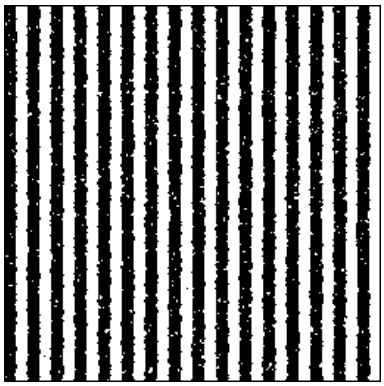

e. *Segmented image using $CM_{lpc}(c = 2)$. Segmentation error = 3.71%.*

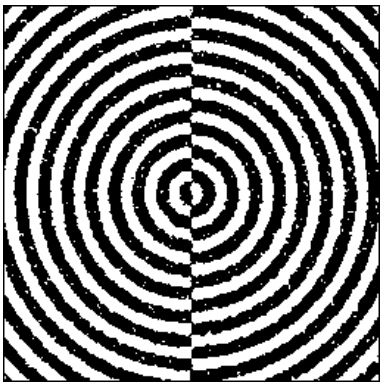

f. *Segmented image using $CM_{lpc}(c = 2)$. Segmentation error = 4.84%.*

Figure 3.8: *Coherence measure, its histogram and segmented image of the vertical straight tubes and circular tubes. (SNR = 3, tubes were 8 pixel width)*

based on speed information problematic and increasing the segmentation error. On the other hand, when the SNR is low, the spatial correlation of flow vectors provides more robust information than the speed information for segmentation with a noisy background. Secondly, speed histograms become well separated when the SNR is high. As such, the segmentation error using speed information is enormously reduced. The segmentation error using flow coherence information, however, is kept constant because of the inevitable errors made at the tube boundaries (flow discontinuities) and the inherent random coherence flow patterns in the background.

Figure 3.9 shows that, among the four different coherence measures, $CM_{lpc}(c = 2)$ and $CM_{lpc}(c = 1)$ give better overall segmentation results than CM_{dev} and CM_{ratio} in the two synthetic images with the tube width set to 8 and 4 pixels. Although $CM_{lpc}(c = 2)$ gives a smaller segmentation errors than $CM_{lpc}(c = 1)$, the difference between $CM_{lpc}(c = 1)$ and $CM_{lpc}(c = 2)$ is relatively small. The difference between them will be manifested when they are tested in the 3D synthetic images presented in the next section.

3.4.3 Three-dimensional LPC measure

Although the synthetic images in the previous section are in 2D, the LPC measure is inherently a general measure that can be applied in any higher dimension. This section shows how to apply the LPC measure in 3D and, as in the previous section, compares its performance with the previously described measures, CM_{dev} and CM_{ratio}.

The extension to 3D is naturally done by applying a 3x3x3 window cube in an image volume. The size of the neighbourhood system, as defined in Equation 3.8, is then increased. The numbers of adjacent vector pairs $|\mathcal{N}_s|$ for $c = 1$ and $c = 2$ are 54 and 158 respectively, which substantially increases the computational load. In the experiments outlined below, we used the same synthetic flow patterns but extended the patterns into 3D (straight and circular cylindrical tubes) with SNRs ranging from 2 to 7. The tube diameters were 8 and 4 voxels, and the image volume sizes were 256x256x(8+2) and 256x256x(4+2) respectively (the extra two image slices are the top and bottom background slices).

Figure 3.10 summarises the segmentation results using the four different coherence measures, CM_{dev}, CM_{ratio}, $CM_{lpc}(c = 1)$ and $CM_{lpc}(c = 2)$. Note that the vertical axes have been rescaled compared to Figure 3.9. In general, the results in Figure 3.10 are comparable to the results in Figure 3.9, which show the applicability of the LPC measure to the 3D pat-

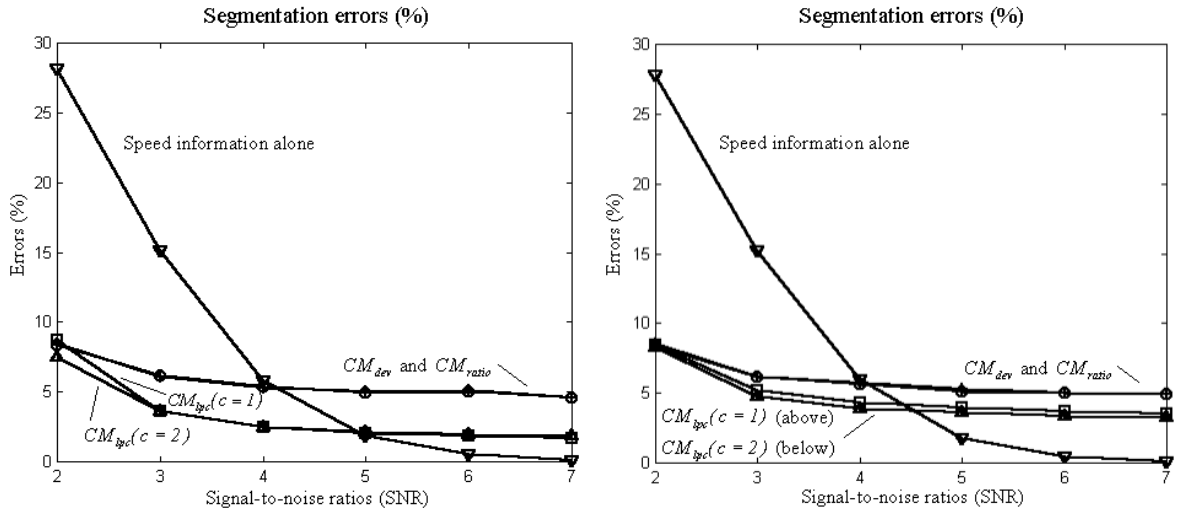

a. *Vertical straight tubes (8 pixel width)* **b.** *Circular tubes (8 pixel width)*

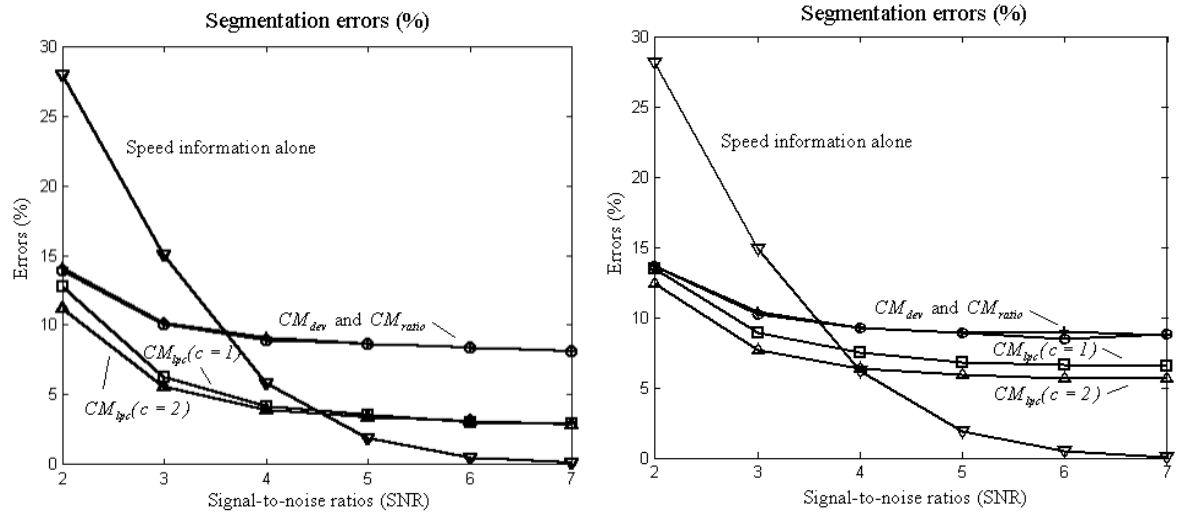

c. *Vertical straight tubes (4 pixel width)* **d.** *Circular tubes (4 pixel width)*

Figure 3.9: *Errors of segmentation using two-dimensional flow coherence information from the synthetic images (vertical and circular tubes).*

terns, and reveal that the LPC measures, especially the second order LPC measure (c=2), perform better than the two other measures, CM_{dev} and CM_{ratio}, and the first order LPC measure $CM_{lpc}(c = 1)$. Note that, between $CM_{lpc}(c = 1)$ and $CM_{lpc}(c = 2)$, the second order neighbourhood system gives more flow coherence evidence to the coherence measure, which makes the measure more robust to noise. It is observed that the overall segmentation errors are lower than those in Figure 3.9 (all vertical axes have been rescaled) because, in 3D patterns, the ratio of the flow boundary (flow discontinuity) voxels to the total voxels is lower than that in 2D.

3.5 Application to PC-MRA images

The proposed coherence measure has been applied to a number of clinical PC-MRA images. Figure 3.11 shows that flow vectors inside the vessels are locally coherent, whereas flow vectors outside the vessels are random. It is also worth pointing out that, as it is illustrated in the figure, flow vectors are likely to be dependent inside vessels. If a flow vector inside a vessel is pointing in a direction v, its neighbouring flow vectors should have a high probability of pointing in the same direction v. This is consistent with the results of clinical flow studies [29, 50, 80] and simulations of computational fluid dynamics (CFD) [13, 24, 64]. For this reason, we can hypothesise that the local coherent flow pattern becomes a useful feature for distinguishing the vascular voxels from the background voxels in PC-MRA images.

To illustrate the applicability of the LPC measure, we applied the second order LPC measure $CM_{lpc}(c = 2)$ to phantom and clinical images. A 180^o U-bend tube with 8mm diameter (SST phantom, ISMRM Flow and Motion Study Group, Stanford CA) was scanned using the PC-MRA protocol on a 1.5T GE MR scanner at the Department of Clinical Neuroscience, King's College London, United Kingdom. The data volume size was $256 \times 256 \times 81$ voxels with voxel dimensions of $0.625 \times 0.625 \times 1.3mm^3$. The flow rate was constant and set at $300mms^{-1}$. The scan details were as follows: axial scan, TE/TR = $7.3/20ms$, flip angle 18^o, 1 signal average, FOV: $22 \times 16cm^2$, VENCS: $400mms^{-1}$ and acquisition matrix: 256×160 pixels.

Figure 3.12a shows a speed image corresponding to a cross-section of the joining arc of the U-bend tube, in which the fluid was flowing into the left tube and flowing out from the right tube. This figure also shows that the intensity values in the middle are low and

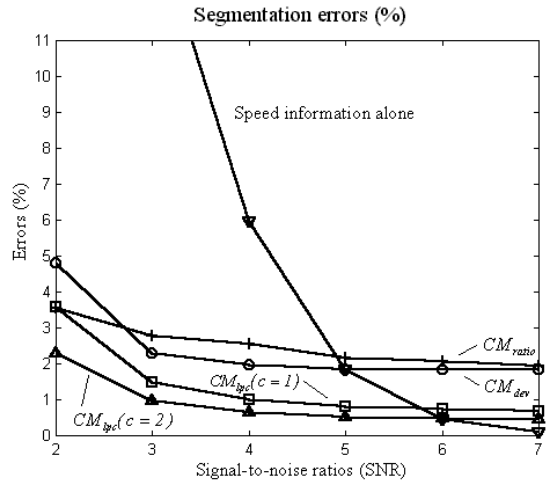

a. *Vertical straight tubes (8 voxel width)*

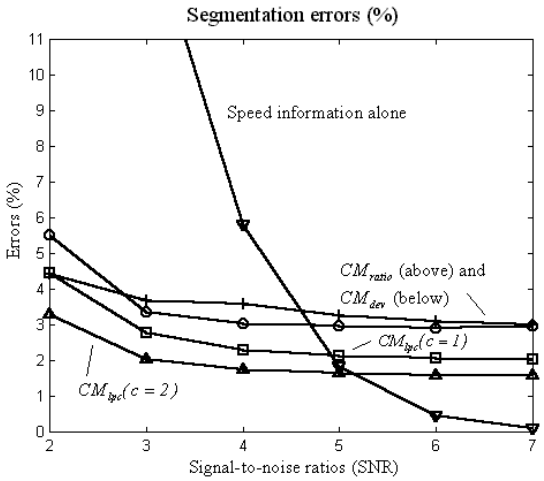

b. *Circular tubes (8 voxel width)*

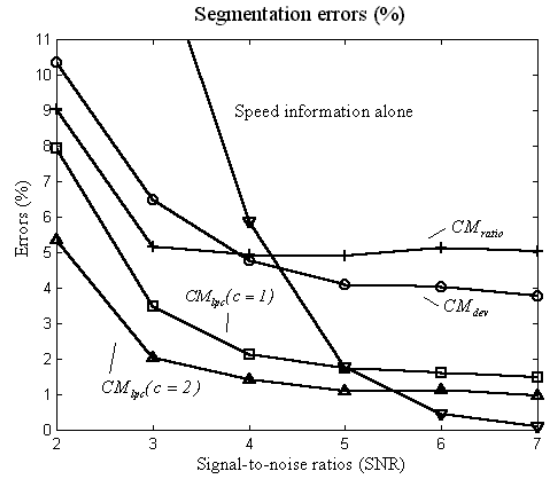

c. *Vertical straight tubes (4 voxel width)*

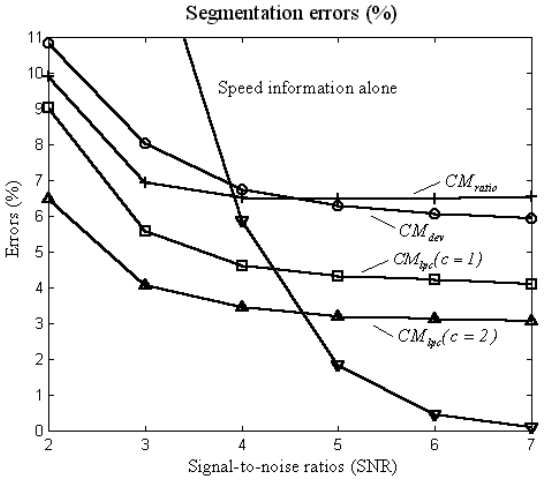

d. *Circular tubes (4 voxel width)*

Figure 3.10: *Errors of segmentation using three-dimensional flow coherence information from the synthetic images (vertical and circular tubes). Note that, relative to Figure 3.9, all vertical axes have been rescaled.*

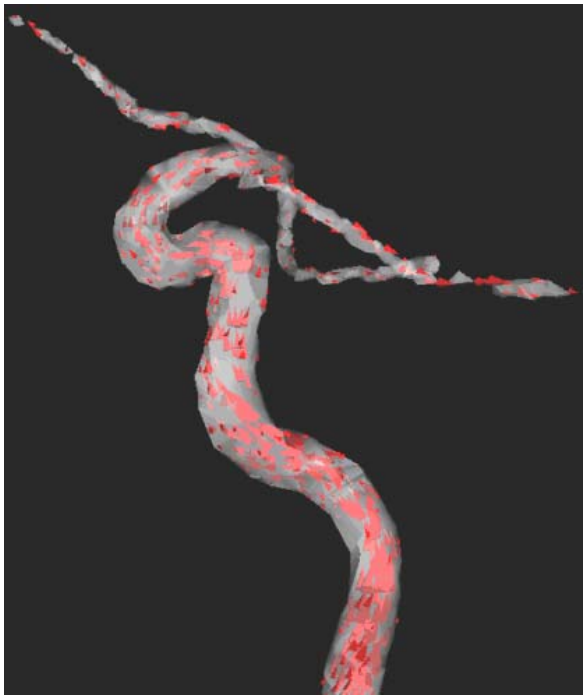

Figure 3.11: *This figure shows that flows inside the vessels are locally coherent.*

a. *Speed image.*

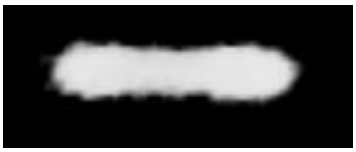

b. *Local phase coherence map.*

c. *ROIs in the speed image.*

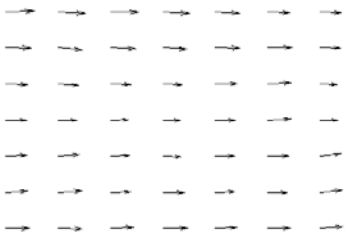

d. *Flow field (ROI-A: Inside the tube)*

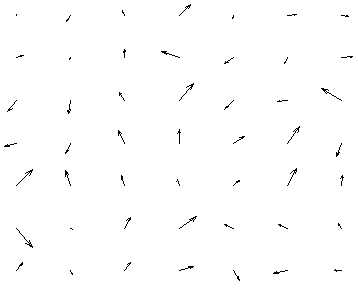

e. *Flow field (ROI-B: Background)*

Figure 3.12: *Speed image, local phase coherence map and flow fields of a* 180^o *U-bend tube.*

that some of the voxels have intensity values almost as low as the background. However, as shown in Figure 3.12b, the 3D LPC map shows a more homogeneous appearance than the corresponding speed image shown in Figure 3.12a. In particular, the region inside the tube is more uniform. Figure 3.12c shows the positions of two regions of interest (ROI) selected for visualisation of the local velocities and flow fields. The components in the xz plane (Figures 3.12d and 3.12e) demonstrate that the flow is coherent inside the tube and random in the background. The SNRs (= *mean*/*variance*) of the regions of interests, ROI-A and ROI-B in Figure 3.12c, are 4.2 and 2.2 respectively.

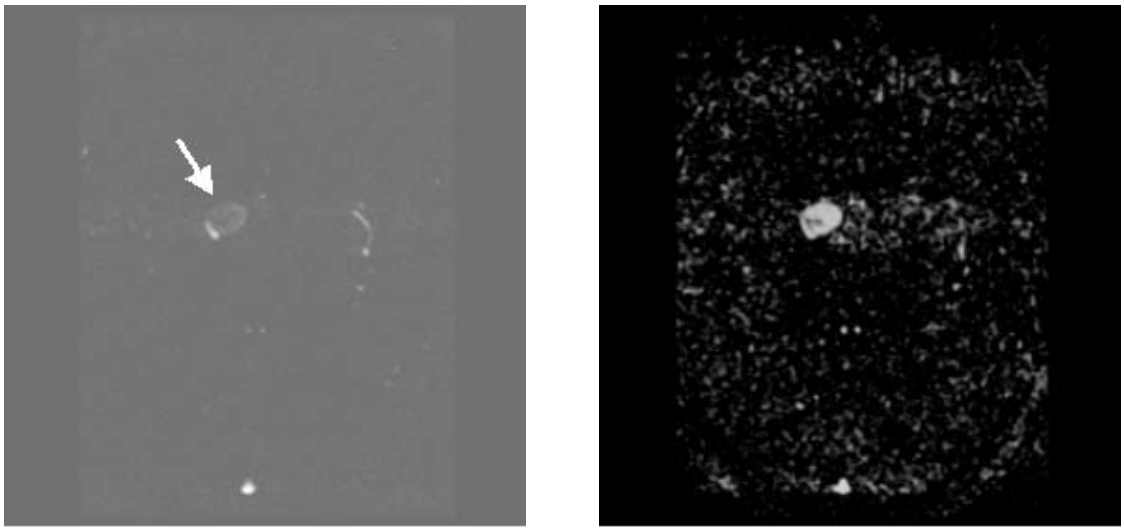

a. *Speed image.* **b.** *Local phase coherence map.*

Figure 3.13: *Clinical speed image and local phase coherence map.*

Figure 3.13a shows a clinical speed image of a patient with an aneurysm (indicated by the arrow) scanned using the PC-MRA protocol on a 1.5T GE MR scanner at King's College London (The scan details can be found in Section 6.4.1). The arrow indicates an intracranial aneurysm with a pronouncedly inhomogeneous appearance on the speed image. Figure 3.13b shows its corresponding LPC map. It is observed that the voxels inside both the aneurysm and vessels exhibit high LPC and form piece-wise homogeneous regions, whereas the non-vessel voxels have relatively low and random LPC. Figure 3.14 shows the ROIs in the speed image, in which the SNRs of the regions of interest, ROI-A and ROI-B, are 3.6 and 1.8 respectively.

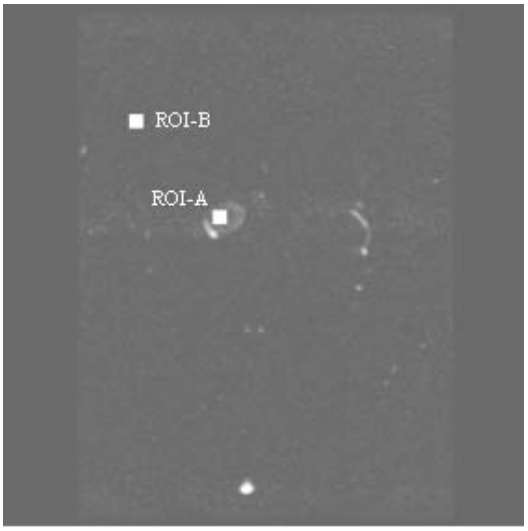

Figure 3.14: *ROIs in the speed image.*

3.6 Summary

In this chapter, we have presented a new local coherence measure, namely the *local phase coherence* (LPC) measure, which greatly enhances the spatial correlations of the neighbouring flow vectors. We have demonstrated that the proposed LPC measure is useful in separating local coherent flow fields from random flow fields. Although the experiments carried out in the chapter are in 2D and 3D, it is straightforward to apply the LPC measure to any higher dimension as well. Moreover, since the LPC measure computes the spatial correlation by using the dot product operation, which is a relative measure based on the angular difference between two vectors, the LPC measure is orientation invariant. Note that the proposed LPC measure is not restricted to normalised vector fields. The LPC measure could be weighted by the flow magnitude at the centre of the window mask, which is given by

$$CM_{lpc}(c = 1 \ or \ c = 2) = |v_s| \cdot \sum_{s_i, s_j \in W_s, \mathcal{N}_s} v_i \cdot v_j, \tag{3.14}$$

where v_s represents the vector at the centre of the window W_s. The LPC measure is potentially useful for flow discontinuity and vessel detection, flow feature extraction in flow-like patterns and optical flow fields.

We have carried out experiments on synthetic images to evaluate and compare the performance of the LPC measure and two other related coherence measures that have appeared in the literature. The experimental results show that (a) when the SNR is low, the segmentation

using the flow coherence measure is more accurate than the segmentation using the speed information alone; (b) the LPC measure outperforms other coherence measures assuming that flow vectors in a field are dependent, and (c) the second order LPC measure (c=2) performs better than the first order LPC measure (c=1) because it gives more evidence of flow vector correlations.

On the other hand, when the SNR is high, simple segmentation using a threshold based on the speed information alone outperforms that using the coherence measure. In Chapter 4 we investigate the idea of a single segmentation process to achieve better segmentation results using both speed and flow coherence information.

Chapter 4

A probabilistic framework for combining speed and flow coherence information

4.1 Introduction

The concept of data fusion is to aggregate data having complementary characteristics acquired from different sources so that better quality information can be achieved. The data sources can be the outputs of feature extraction methods (e.g. edge or optical flow), or sensing and imaging devices (e.g. laser or ultrasound rangefinders, MR and CT). To increase segmentation quality for objects having real flow fields (e.g. vessels or pipes) or objects having flow-like features (e.g. edges or optical flow fields), this chapter introduces a probabilistic data fusion framework for combining *speed* (or flow magnitude) and *flow coherence* information, which have been described in Chapters 2 and 3 respectively.

As illustrated in Chapter 3, segmentation using speed information alone performs well when the SNR is high because the background and object histograms are well separated. However, when the SNR is low, the background and object histograms start to overlap, which makes the speed information unreliable. The flow coherence measure introduced in Chapter 3 compensates for the deficiency of the speed information and yields more reliable information for segmentation when the SNR is low. As such, the benefit of aggregating speed and flow coherence information is that a better segmentation algorithm, which performs well

for both low and high SNR values, can be achieved.

In our method, a probabilistic framework is employed for data fusion because it provides a consistent framework for (a) enhancing the local relationships between the voxels through the prior probability, i.e. the MRF-Gibbs distributions, (b) modelling knowledge of the image formation process through the likelihood function, i.e. the MGU statistical model in Chapter 2, and (c) making the minimum risk decision, i.e. MAP estimation, given that the prior probability and likelihood function are known.

Experiments have been carried out on synthetic and clinical images. The results show that the new segmentation approach outperforms segmentation using either speed or flow coherence information alone by giving higher segmentation accuracy at both low and high SNR values.

4.2 Integration using a probabilistic framework

In this section, we begin by introducing a powerful probabilistic framework, namely the MAP estimation, which is commonly used in solving computer vision and statistical problems. We then discuss the use of Markov random fields (MRF) models to estimate the MAP solution in a more robust and efficient manner, and enhance the local relationships between sites (pixels or voxels). A brief explanation of the typical minimisation methods for the MAP-MRF estimation follows. Finally, we show how to incorporate the speed (or flow magnitude) and flow coherence information as *a priori* knowledge in the MAP-MRF estimation so that the segmentation error can be reduced.

4.2.1 Maximum *a posteriori* (MAP) estimation

Maximum *a posteriori* (MAP) estimation has been a useful statistical tool in solving computer vision problems, such as object and pattern classification [21, 38, 10], and image restoration [28, 9] because it makes a decision with minimum risk [10, 53]. Given that the posterior probability is known, the MAP estimation classifies the image voxels with minimum error of probability [52].

Let $S = \{s_i | i \in Z_n\}$, where $Z_n = \{1, \ldots, n\}$, represent a regular lattice structure with n sites. Let $\mathcal{X} = \{x_i | i \in Z_n\}$ and $\mathcal{Y} = \{y_i | i \in Z_n\}$ be the true image and the observed image respectively, where x_i can be equal to one of the labels in $L = \{1, 2, \ldots, m\}$, y_i represents one

of the observed values, e.g. intensity $\{0, \ldots, I_{max}\}$, and m is equal to the number of possible classes. Let $\Omega_{\mathcal{X}} = L \times \cdots \times L = L^n$ be the sample space of $\mathcal{X}$, $\mathcal{X} \in \Omega_{\mathcal{X}}$, and $\Omega_{\mathcal{Y}}$ be the observation space, $\mathcal{Y} \in \Omega_{\mathcal{Y}}$.

The MAP estimation, in principle, maximises the posterior probability $p(\mathcal{X}|\mathcal{Y})$ of the true image $\mathcal{X}$ given the observed image $\mathcal{Y}$, i.e. $p(\mathcal{X}|\mathcal{Y}) = p(x_1, \ldots, x_n|y_1, \ldots, y_n)$. Given that the prior probability $p(\mathcal{X})$ and likelihood function $p(\mathcal{Y}|\mathcal{X})$ are known, the posterior probability can be estimated according to the Bayes' theorem,

$$p(\mathcal{X}|\mathcal{Y}) \propto p(\mathcal{X})p(\mathcal{Y}|\mathcal{X}), \tag{4.1}$$

where $p(\mathcal{X})$ represents the prior beliefs about the image, and $p(\mathcal{Y}|\mathcal{X})$ embodies the knowledge in image formation and noise properties. The MAP decision rule for the optimal solution $\hat{\mathcal{X}}$ is given by,

$$\hat{\mathcal{X}} = arg \max_{\mathcal{X} \in \Omega_{\mathcal{X}}} p(\mathcal{X})p(\mathcal{Y}|\mathcal{X}), \tag{4.2}$$

which, however, represents an exhaustive combinatorial optimisation problem because of the large search for $\mathcal{X}$ in $\Omega_{\mathcal{X}}$. The size of $\Omega_{\mathcal{X}}$ is equal to m^n, i.e. $|\Omega_{\mathcal{X}}| = m^n$. Typically, $m = 2$ if it is a binary segmentation problem and $n = 256 \times 256$. This means that it is almost impossible to search the whole sample space $\Omega_{\mathcal{X}}$ extensively for the optimal solution $\hat{\mathcal{X}}$, and we must therefore use the prior probability to constrain the solution.

For example, if the prior probability $p(\mathcal{X})$ is non-informative or uniformly distributed, then the MAP estimation is equivalent to the Maximum Likelihood Estimation (MLE). On the other hand, the prior probability can be informative and influential in the MAP estimation if appropriate *a priori* knowledge is incorporated [12]. Moreover, multiple prior information sources can be aggregated in the prior probability so that the uncertainty in the decision process can be reduced. An good example is the integration of intensity (pixel site) and edge (line site) information in the prior probability [28]. (see also [27] for another good example in surface reconstruction). This is the main idea used in this chapter.

4.2.2 Markov random field (MRF) models and Gibbs distributions

Markov random field (MRF) theory was introduced to the image processing community by Geman and Geman [28] for modelling the local relationships between image voxels so that the optimal solution of the MAP estimation could be obtained in a more robust and efficient manner, either by the simulated annealing algorithm (SA) [28] or the iterated conditional

modes (ICM) method [9]. Geman and Geman showed that the MRF model is an effective way of representing *a priori* knowledge. Moreover, Clark and Yuille [19] proposed using the MRF model for combining multiple information sources.

We assume that the local relationships between sites in S are described by a neighbourhood system $\mathcal{N}$, which is defined as

$$\mathcal{N} = \{\mathcal{N}_i | i \in Z_n\}, \tag{4.3}$$

where $\mathcal{N}_i \subseteq S$ represents a set of sites adjacent to the site s_i. There are two properties of $\mathcal{N}$. Firstly, site s_i is assumed not to belong to its neighbourhood set, i.e. $s_i \notin \mathcal{N}_i$, and secondly interactions between sites are bi-directional, i.e. $s_i \in \mathcal{N}_j \Leftrightarrow s_j \in \mathcal{N}_i$.

The definition of a *Markov random field*: given a neigbourhood system $\mathcal{N}$, $\mathcal{X}$ is an MRF if and only if two conditions are satisfied [28].

$$p(\mathcal{X}) > 0, \quad for\ all\ \mathcal{X} \in \Omega_{\mathcal{X}}\ and \tag{4.4}$$

$$p(x_i | x_j, i \neq j) = p(x_i | x_j, s_j \in \mathcal{N}_i), \tag{4.5}$$

where $i, j \in Z_n$. Equation 4.4, which is the *positivity* property of the MRF, states that any realisation of the field $\mathcal{X}$ is possible. Any field that satisfies this condition is also called a *random field* [48]. Equation 4.5 describes the *Markovian* property of the MRF, which denotes the individual conditional probability at each site and represents the *local characteristics* between sites. This states that the probability of an event at site s_i is dependent only on the events at the neighbouring sites s_j. According to [28, 8], *the joint probability $p(\mathcal{X})$ of any process satisfying Equation 4.4 is uniquely determined by the conditional probabilities specified in Equation 4.5.* This implies that if $\mathcal{X}$ is an MRF, the joint probability $p(\mathcal{X})$ (in Equation 4.4) of the variables x_i, $i \in Z_n$, can be derived from the individual conditional probabilities. However, the immediate question that follows is how to determine the conditional probabilities. By virtue of the Hammersley-Clifford theorem [8], the Gibbs distribution provides us with a practical way of specifying the conditional probabilities.

Hammersley-Clifford theorem: let $\mathcal{N}$ be a neighbourhood system. Then $\mathcal{X}$ is a MRF with respect to $\mathcal{N}$ if an only if $p(\mathcal{X})$ is a Gibbs distribution with respect to $\mathcal{N}$. A Gibbs distribution of $\mathcal{X}$ is given by,

$$p(\mathcal{X}) = \frac{1}{Z} \times e^{-\frac{U(\mathcal{X})}{T}}, \tag{4.6}$$

where T is a temperature parameter, $U(\mathcal{X})$ is the energy function and Z is a normalising

constant and is given by

$$Z = \sum_{\mathcal{X}' \in \Omega_{\mathcal{X}}} e^{-\frac{U(\mathcal{X}')}{T}}, \tag{4.7}$$

i.e. the normalising constant is the summation of all the values of possible realisations (or configurations). A clique c is a subset of sites, $c \subseteq S$, which can be a single-site clique $c \in \mathcal{C}_1 = \{s_i\}$, a pair-site clique $c \in \mathcal{C}_2 = \{s_i, s_j | s_i \textit{ and } s_j \textit{ are adjacent}\}$ or multiple-site clique. The energy is then defined as

$$U(\mathcal{X}) = \sum_{s_i \in \mathcal{C}_1} V_1(x_i) + \sum_{\{s_i, s_j\} \in \mathcal{C}_2} V_2(x_i, x_j) + \text{higher order energy terms}, \tag{4.8}$$

where V_1 and V_2 are potential functions. Note that the potential function V_2 enforces the Markovian property of the MRF by encoding the local dependence between adjacent sites s_i and s_j. In this thesis, the first order energy $U(\mathcal{X})$ (Ising model) is used because, in practice, it strikes a balance between the complexity of the local relationships and computational load. Specifically, the Ising model is employed, which includes either the nearest four neighbours in 2D, or the nearest six neighbours in 3D. Depending on the nature of applications and availability of parallel processors, higher energy models may be utilised to enhance higher order interactions between sites, e.g. second order dependence or triple-site clique $c \in \mathcal{C}_3 = \{s_i, s_j, s_k | s_i, s_j \textit{ and } s_k \textit{ are adjacent}\}$.

Suppose that the likelihood function $p(\mathcal{Y}|\mathcal{X})$ can be re-expressed by an MRF. From Equations 4.2 and 4.6, the MAP decision rule becomes

$$\hat{\mathcal{X}} = arg \max_{\mathcal{X} \in \Omega_{\mathcal{X}}} \left(\frac{1}{Z'} \times e^{-\frac{U(\mathcal{X}) + U(\mathcal{Y}|\mathcal{X})}{T}} \right), \tag{4.9}$$

where Z' is a normalising constant. This in turn leads to a new minimisation problem, and the MAP-MRF decision rule can then be re-expressed as

$$\hat{\mathcal{X}} = arg \min_{\mathcal{X} \in \Omega_{\mathcal{X}}} \left(\frac{U(\mathcal{X}) + U(\mathcal{Y}|\mathcal{X})}{T} \right) = arg \min_{\mathcal{X} \in \Omega_{\mathcal{X}}} \left(\frac{U(\mathcal{X}|\mathcal{Y})}{T} \right), \tag{4.10}$$

where $U(\mathcal{X})$, $U(\mathcal{Y}|\mathcal{X})$, $U(\mathcal{X}|\mathcal{Y})$ denote the prior, likelihood and posterior energies respectively.

The prior energy $U(\mathcal{X})$ represents a hierarchical interaction structure [28], which can be easily extended from a local dependence structure to a complete connected structure. In practice, only local relationships are incorporated in the prior energy. This makes the parallelisation of the optimisation algorithms feasible in principle. Moreover, the attractiveness of the MRF-Gibbs modelling lies in its exponential form because it turns a product of probability distributions into a sum of energy terms, which makes the quantitative analysis of

the optimal solution more mathematically tractable. For example, it gives quadratic energy terms if the distributions are Gaussian.

4.2.3 Optimisation methods for the MAP-MRF estimation

The derived objective function in Equation 4.10 can be optimised either by global methods or local methods. Global and local methods differ mainly in the nature of the solutions obtained. The former seeks the global minimum even though there are many local minima, whereas the latter finds the minimum locally, which could be the global minimum if there is only one minimum or if the initial estimate is very close to the global solution. A good review of a variety of optimisation methods can be found in a book by Li [48].

The simulated annealing (SA) algorithm is a global stochastic optimisation method, and was independently introduced by Kirkpatrick [42] and Černy [18]. SA is an iterative optimisation process based on a *Monte Carlo* technique, (*Metropolis algorithm* [60] or *Gibbs sampler* [28]), which randomly generates a large number of configurations $\mathcal{X} \in \Omega_{\mathcal{X}}$ at each step. According to the Metropolis algorithm, the next configuration $\mathcal{X}'$ is generated from the current configuration $\mathcal{X}$ using a perturbation mechanism, which changes randomly the current label of one site s_i into a new label by a small distortion, e.g. displacement of a neighbouring site $s_j \in \mathcal{N}_i$ [1]. If the energy change $U(\mathcal{X}'|\mathcal{Y}) - U(\mathcal{X}|\mathcal{Y})$ is negative, then the change is accepted. Otherwise, the change is accepted only if $e^{\frac{-(U(\mathcal{X}'|\mathcal{Y})-U(\mathcal{X}|\mathcal{Y}))}{T}} \geq random[0,1)$. In a simpler way, the Gibbs sampler, at a fixed T, generates the next configuration $\mathcal{X}'$ from the current configuration $\mathcal{X}$ by changing one site s_i into one of the labels in L randomly according to the local conditional probabilities[1] $p(x_i|s_i \in \mathcal{N}_i)$. Usually, at a fixed T, this "configuration changing" process is stopped if there is an adequate number of accepted changes or if it exceeds a fixed number of changes.

It has been shown by Geman and Geman [28] that employing either the Metropolis algorithm or the Gibbs sampler, and regardless of the initial configuration, *SA will converge to the globally optimal MAP solution* if each site is visited infinitely often and the temperature value T decreases gradually after each iteration step, according to a specific decreasing schedule $T(t)$, which satisfies two conditions: (a) $T(t) \rightarrow 0$ *as* $t \rightarrow \infty$; and (b) $T(t) \geq n\Delta/log\ t$, where

[1]For example, assumed that there are two labels, $\{0,1\}$, $p(x_i = 0|s_i \in \mathcal{N}_i) = 0.3$ and $p(x_i = 1|s_i \in \mathcal{N}_i) = 0.7$. If a random number is generated, which is ranged between 0 and 1, then label 0 is assigned if the number is between 0 and 0.3, and label 1 is assigned if the number is between 0.3 and 1.

n represents the total number of sites, t (≥ 2) denotes the number of iterations and

$$\Delta = (\max_{\mathcal{X}} U(\mathcal{X}|\mathcal{Y})) - (\min_{\mathcal{X}} U(\mathcal{X}|\mathcal{Y})). \tag{4.11}$$

In practice, to avoid a larger number of iterations in approaching the freezing point $T \rightarrow 0$, $T(t)$ is set to $C/log(1+t)$, where $C = 3$ or 4 [28]. SA iteratively seeks for a lower energy configuration in each step. However, depending on the current temperature value, it allows occasional increases in energy level to avoid local minima. The tradeoff is that a long computation time is incurred [9, 36].

Besag [9] proposed a deterministic local search method, namely iterated conditional modes (ICM). Unlike SA, ICM persistently seeks a lower energy configuration and never allows increases in energy, which guarantees a faster convergence rate. For example, in the segmentation of brain images, ICM converges within 10 iterations, whereas SA needs 1000 iterations [36]. It should be noted that the temperature value T is fixed throughout the entire searching process. ICM assumes that (a) the observed variables $\mathcal{Y} = \{y_i | i \in Z_n\}$ are conditionally independent, i.e. $p(\mathcal{Y}|\mathcal{X}) = \prod_{i=1}^{n} p(y_i|x_i)$ in Equation 4.2 and $U(\mathcal{Y}|\mathcal{X}) = \sum_{i=1}^{n} U(y_i|x_i)$ in Equation 4.10; and (b) the state of a site s_i depends only on the states of its adjacent sites $\mathcal{N}_i$ (Markovian property), i.e. $p(\mathcal{X}) = \prod_{i=1}^{n} p(x_i|s_i \in \mathcal{N}_i)$ in Equation 4.2 and $U(\mathcal{X}) = \sum_{i=1}^{n} U(x_i|s_i \in \mathcal{N}_i)$ in Equation 4.10. These two assumptions enable the maximisation of the local posterior probability $p(x_i|y_i, s_i \in \mathcal{N}_i)$ in each iteration step such that the overall posterior probability $p(\mathcal{X}|\mathcal{Y})$ can be optimised after a convergence has been reached. The local posterior probability, which is defined as

$$p(x_i|y_i, s_i \in \mathcal{N}_i) = p(x_i|s_i \in \mathcal{N}_i) p(y_i|x_i), \tag{4.12}$$

at a site s_i, is equivalent to the minimisation of its local posterior energy

$$U(x_i|y_i, s_i \in \mathcal{N}_i) = U(x_i|s_i \in \mathcal{N}_i) + U(y_i|x_i). \tag{4.13}$$

It is clear that the optimisation is entirely local and is extremely simple to implement.

In general, although SA may seem preferable because it guarantees convergence to the global optimal MAP solution, there are two advantages of using ICM. Firstly, by having a comprehensive knowledge of the image formation process and noise properties, as described in Chapter 2, the initial estimate of the true image $\mathcal{X}$ can be very close to the optimal solution. Compared with SA, consistent and fast convergence makes ICM more attractive in some time-critical applications.

Recently, new deterministic global methods have been developed for solving MRF problems in computer vision. Examples include the Exact MAP estimation algorithm [76, 41, 31], mean field theory [40, 22, 27] and the graduated non-convexity method [11]. However, some of these methods are in the early stages of development. To make the most of these methods, more detailed comparisons are necessary to understand their strengths and weaknesses.

4.2.4 Fusing speed and flow coherence information in the MAP-MRF prior energy

A priori knowledge is very important for solving statistical decision problems, like the MAP estimation in Equation 4.2, because it influences the determination of the posterior probability and in turn affects the decision certainty [12]. As pointed out in Section 4.2.2, the MRF prior energy $U(S)$ encodes the local relationships between sites, and in fact is a practical and effective way of aggregating multiple prior information [19, 53], such as intensity values, edges and other useful features.

Most prior works in MAP-MRF based data fusion are related to the combination of intensity and edge information. For example, Geman and Geman [28] proposed to combine pixel intensity values and binary edge values. The use of MAP-MRF models has been further investigated and applied in a variety of ways, such as surface reconstruction [27, 26], a weak membrane modelling [11], ill-posed problems in vision [53] and fusion of sensory information [19]. In general, the prior energy is given by,

$$U(\mathcal{X}) = \underbrace{\lambda \sum_{i \in Z_n} \sum_{s_j \in \mathcal{N}_i} (x_i - x_j)^2 (1 - l_i)}_{Spatial\ smoothing\ term} + \underbrace{\mu \sum_{i \in Z_n} l_i}_{Edge\ term}, \tag{4.14}$$

where $x_i \in L$, l_i ($\in \{0, 1\}$) represents a binary edge element between two neighbouring sites, λ and μ denote weights (constants) attached to each term. This form of prior energy smoothes the image locally when there is no existence of an edge element ($l_i = 0$), and preserves the image edges when an intensity discontinuity exists ($l_i = 1$). While minimising the prior energy, the second term becomes a penalty term to the line elements if μ is positive. A smoother image will be obtained if μ is large and positive.

In this chapter, by applying the concepts of data fusion, we propose a new flow coherence term in the MRF prior energy, based on the coherence measure presented in Chapter 3, such that the information about flow coherence and speed (or flow magnitude) can be effectively

incorporated into the *a priori* knowledge, and a better quality segmentation can be obtained.

Assume that there exists a flow field in an image, in which flow vectors with different flow magnitudes and directions are situated at the centre of the sites. Each site variable $x_i \in \mathcal{X}$ will be classified as one of the labels $\{0, 1\}$, where $x_i = 1$ if the site belongs to the object having locally coherent flow and relatively high flow magnitude, and $x_i = 0$ if the site belongs to the background with random and relatively low flow. Assume that the flow coherence $\mathcal{O}$ is a constant field rather than an MRF because the observed flow field is fixed during the energy minimisation process, and that x_i and o_i are located at the same site. Based on the coherence measure between the normalised flow vectors, a site is labelled as one, i.e. $o_i = 1$, if the flow vectors are locally coherent at x_i, or $o_i = 0$ if the vectors are locally non-coherent. Note that the MRF $\mathcal{X}$ can be initialised based on the statistics of the flow magnitudes, as described in Chapter 2. The goal is to partition an image into two separate and distinct regions: (a) the object and (b) the background based on the flow magnitudes and coherence.

The *a priori* knowledge is derived based on an observation that a site s_i is likely to belong to the object class, $x_i = 1$, if its neighbouring object sites and itself are locally coherent, i.e. $x_j = 1$, $o_i = 1$ and $o_j = 1$. The interactions between sites are described as follows. If $o_i = 0$, i.e. flow is not locally coherent at a site s_i, then the site belongs to background, i.e. $x_i = 0$. If $o_i = 1$, then the site s_i belongs to the object only if its adjacent sites belong to object $x_j = 1$ and are locally coherent $o_j = 1$. Otherwise, $x_i = 0$. The new prior energy term is then defined as

$$U(\mathcal{X}, \mathcal{O}) = \underbrace{\sum_{i \in Z_n} \sum_{s_j \in \mathcal{N}_i} \beta_1 (1 - x_i) x_j o_i o_j + \beta_2 x_i (1 - x_j o_i o_j)}_{\textit{Flow coherence term}}, \tag{4.15}$$

where β_1 and β_2 are positive weights, which need not sum to one, and $\mathcal{N}_i$ is the Ising first order neighbourhood system. The parameter β_1 controls the influence of the object-and-coherent sites in the interactions between the adjacent sites, while β_2 governs the weight of the background or non-coherent sites. Note that in similarity to the standard anisotropic Potts model, which weights cliques according to their orientations, β_1 and β_2 could be set to different values. For instance setting β_1 to a higher value than β_2 will enhance the interaction between the object-and-coherent sites [75, 48, 61]. For simplicity in the MRF model, only (but not limited to) the flow coherence term is included in the total prior energy in this work.

As such, from Equation 4.10, the MAP-MRF decision rule becomes

$$\hat{\mathcal{X}} = arg \min_{\mathcal{X} \in \Omega_{\mathcal{X}}} (U(\mathcal{X}, \mathcal{O}) + U(\mathcal{Y}|\mathcal{X})), \tag{4.16}$$

where $U(\mathcal{X}, \mathcal{O})$ is the flow coherence prior energy defined in Equation 4.15 and $U(\mathcal{Y}|\mathcal{X})$ is the likelihood energy. Note that the ICM method is employed in this work, i.e. T is constant in Equation 4.10 and, hence, is not included in Equation 4.16. Also, in this work, each site s_i contains likelihood energies for the background and vessel voxels, which are given by, according to Equation 2.13 in Section 2.3.5,

$$\text{For background voxel, } U(y_i|x_i = 0) = -\log\left(\frac{w_M f_M(y_i) + w_G f_G(y_i)}{w_M + w_G}\right) \text{ and } \tag{4.17}$$

$$\text{For vessel voxel, } U(y_i|x_i = 1) = -\log f_U(y_i), \tag{4.18}$$

respectively.

4.3 Experimental results on synthetic images

Recall from Chapter 3 that the speed information gives better segmentation results for high SNR regions, but becomes unreliable when the SNR level is low. The flow coherence measure compensates well for this deficiency and provides more reliable information for the segmentation of low SNR regions. On the other hand, segmentation using flow coherence information alone is not as good as that using the speed information alone in high SNR regions. To investigate a possible improvement on this by combining the methods, we implemented the MAP-MRF model using a first order neighbourhood system (Ising Model) and the new flow coherence prior energy aggregating the complementary speed and flow coherence information in a flexible and unified probabilistic framework. In this section, we present the implementation details, and experimental results based on the two synthetic images: the vertical straight tubes and circular tubes described in Section 3.4.1 (Figures 3.6a and 3.6b respectively).

4.3.1 Implementation details

This section will provide details of the implementation. The goal is to find an image $\hat{\mathcal{X}}$ with minimum energy configuration through an energy minimisation process using the ICM method, (described in Section 4.2.3) because of its fast convergence rate, simple implementation and the availability of a good initial estimate based on our knowledge of the image

formation process. T is set to 1 throughout the minimisation process [9]. The implementation process is outlined in Figure 4.1.

Each image is initially segmented using the EM algorithm with the utilisation of the MGU statistical model (Chapter 2). The result is then treated as an initial estimate for the MAP-MRF model, which iteratively maximises the posterior energy $U(\mathcal{X}|\mathcal{Y})$ and changes the site class $\{0, 1\}$ at each site according to the intensity $\mathcal{X}$ and flow coherence $\mathcal{O}$ information. The iteration process is repeated until the posterior energy is maximised and there is no change in site classes. The final estimate represents the output image. Convergence is normally reached after 10 iterations.

(1) Segment the image using the EM algorithm and MGU model.
Initial estimate $\mathcal{X}^0$ and likelihood energy $U(\mathcal{Y}|\mathcal{X})$ are obtained,
where $U(\mathcal{Y}|\mathcal{X}) = -log\ P(\mathcal{Y}|\mathcal{X})$, negative log of the likelihood function.
(2) Compute the coherence measure $CM_{lpc}(c = 2)$ at each site.
(3) Segment the image using $CM_{lpc}(c = 2)$. $\mathcal{O}$ is obtained,
where $o_i = 1$ and 0 represent coherent and non-coherent sites respectively, and
x_i and o_i are located at the same site position.
(4) Iterate for $k = 1, \ldots, MaxItn$: ($MaxItn$ = Maximum number of iterations)
(5) Iterate for $i = 1, \ldots, n$: (n = Total number of sites)
(6) $x_i^k = arg\ \min_{x_i^k \in L}(U(x_i^k|o_i, x_j^{k-1}, o_j) + U(y_i|x_i^k))$,
where
$U(x_i^k|o_i, x_j^{k-1}, o_j) = \sum_{s_j \in \mathcal{N}_i} \beta_1(1 - x_i^k)x_j^{k-1}o_io_j + \beta_2 x_i^k(1 - x_j^{k-1}o_io_j)$.
(7) Terminates if $\mathcal{X}^{k-1} = \mathcal{X}^k$ or $k = MaxItn$.
(8) Final estimate $\hat{\mathcal{X}} = \mathcal{X}^k$.

Figure 4.1: *Segmentation algorithm based on the MAP-MRF model using the flow coherence prior energy.*

4.3.2 Two-dimensional synthetic images

We segmented the two synthetic 2D images using different values of β_1 and a fixed value of β_2. β_2 was set to 1 throughout this thesis and, compared the differences in segmentation when β_1 was varied from 1 to 3. The segmentation performance was measured based on the ratio of the number of misclassified pixels to the total number of total voxels, which is given

by

$$\text{Segmentation error} = \frac{\text{Number of misclassified pixels}}{\text{Total number of pixels in the image}} \times 100\%. \tag{4.19}$$

Figure 4.2 shows that when $\beta_1 = 2$, segmentation errors are smaller than the other two values, $\beta_1 = 1$ and 3, over the whole range of SNR (from 2 to 7). As such, we set $\beta_1 = 2$ in this implementation. Note also that the difference in segmentation errors between $\beta_1 = 2$ and $\beta_1 = 3$ is small, and the discrepancy in segmentation errors between the values of β_1 is relatively small when the SNR is high. As with other MRF models [41, 31], the values of β_1 and β_2 are application dependent and should be carefully chosen when the proposed algorithm is utilised in other potential applications.

Figure 4.3 shows the results of the three different segmentation methods, based on (a) speed information alone, (b) flow coherence information alone using the second order local flow coherence measure $CM_{lpc}(c = 2)$, and (c) the MAP-MRF model using both speed and flow coherence information. A substantial improvement is shown in Figure 4.3, where the overall segmentation errors have been reduced and remain the lowest at all SNR values when the speed and flow coherence information is combined using the flow coherence prior energy in the MAP-MRF model.

4.3.3 Three-dimensional synthetic images

We extend the approach to 3D by applying the Ising model in three-dimensions, which includes the six first order neighbouring voxels $(x-1, y, z), (x+1, y, z), (x, y-1, z), (x, y+1, z), (x, y, z-1)$ and $(x, y, z+1)$. The benefit of a 3D analysis is that information exchange will be encouraged across the image slices rather than only within a slice in the 2D case so that, in our applications, vessels traversing in the through-plane direction can be identified.

As with the 2D application, shown in Figure 4.2, Figure 4.4 reveals that the overall segmentation errors of the 3D synthetic images are lowest when β_1 and β_2 are set to 2 and 1 respectively. With these values of β_1 $(= 2)$ and β_2 $(= 1)$, the results in Figure 4.5 demonstrate that the MAP-MRF model with the flow coherence prior energy gives a better performance overall than the segmentations using speed information alone and flow coherence information alone.

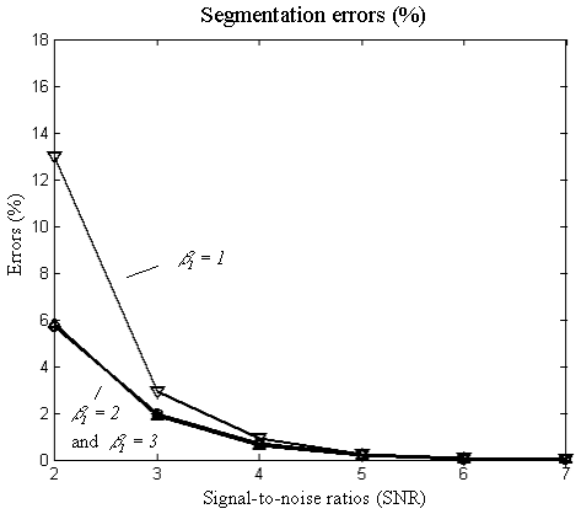

a. *Vertical straight tubes (8 pixel width)*

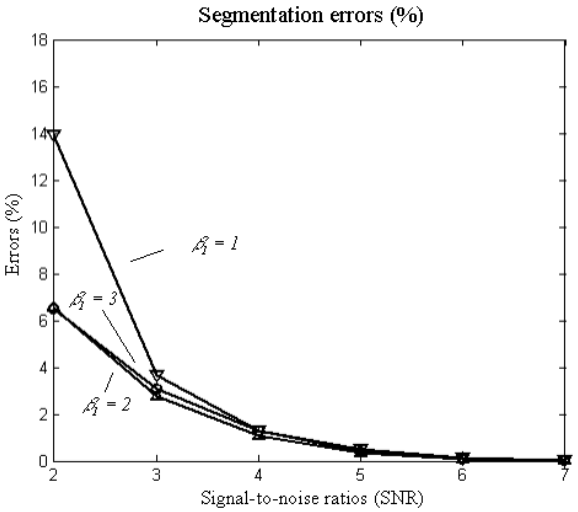

b. *Circular tubes (8 pixel width)*

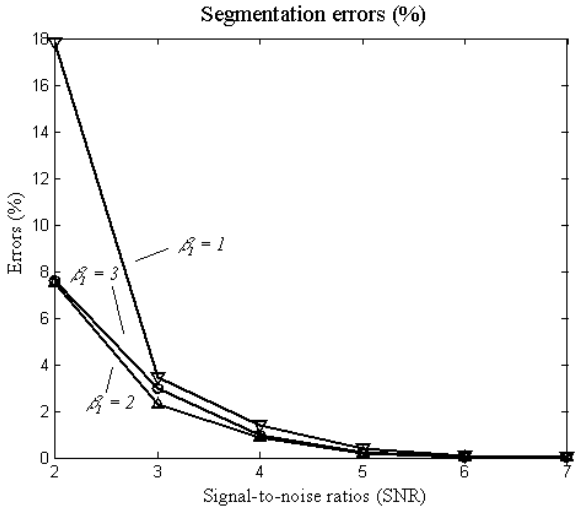

c. *Vertical straight tubes (4 pixel width)*

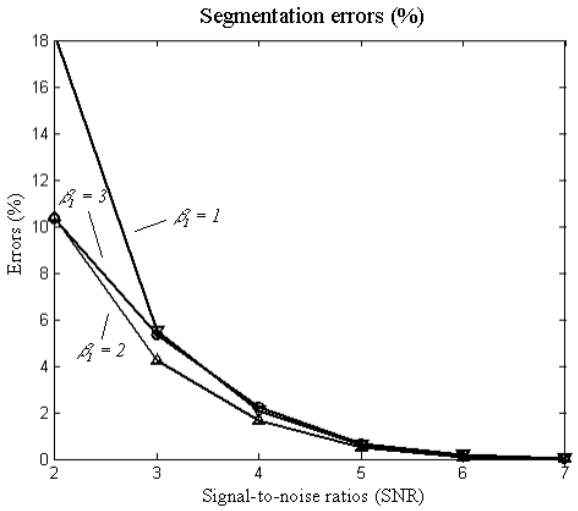

d. *Circular tubes (4 pixel width)*

Figure 4.2: *Segmentation errors in the 2D synthetic images (vertical and circular tubes) with different values of* $\beta_1 = 1, 2, 3$ *for a fixed value of* $\beta_2 = 1$.

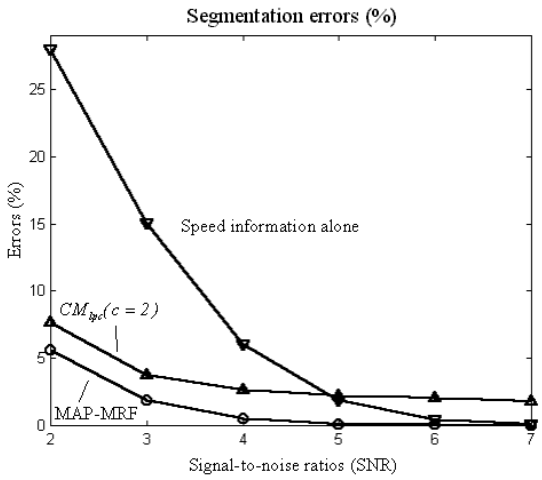

a. *Vertical straight tubes (8 pixel width)*

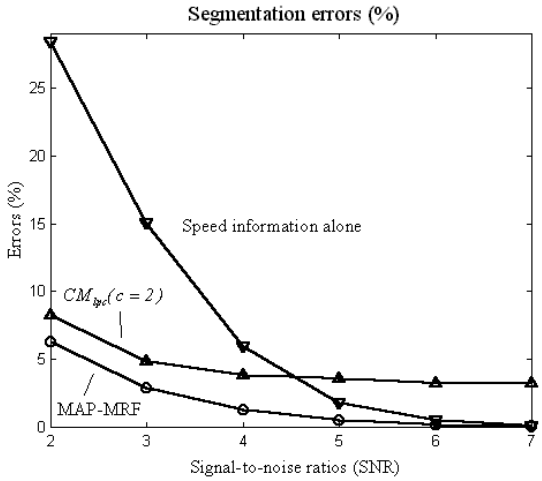

b. *Circular tubes (8 pixel width)*

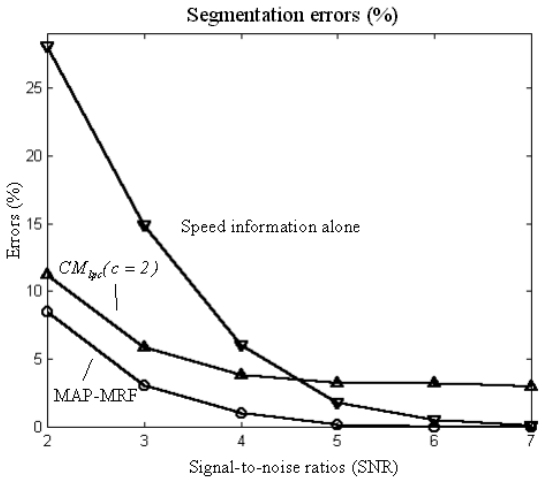

c. *Vertical straight tubes (4 pixel width)*

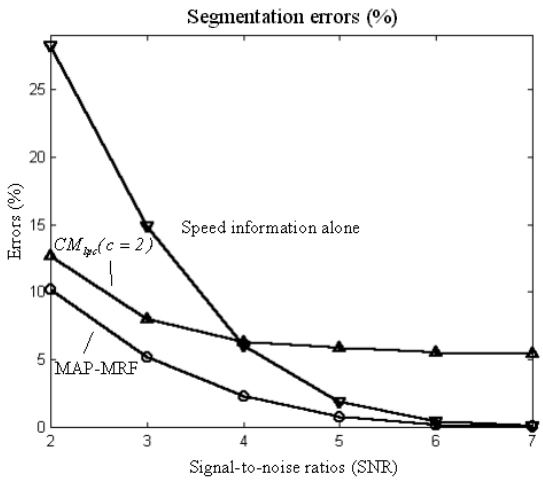

d. *Circular tubes (4 pixel width)*

Figure 4.3: *Comparison on the results based on (1) segmentation using speed information alone, (2) segmentation using flow coherence information alone, and (3) segmentation using both speed and flow coherence information. All segmentations were done on the 2D synthetic images (vertical and circular tubes).* $\beta_1 = 2$ *and* $\beta_2 = 1$.

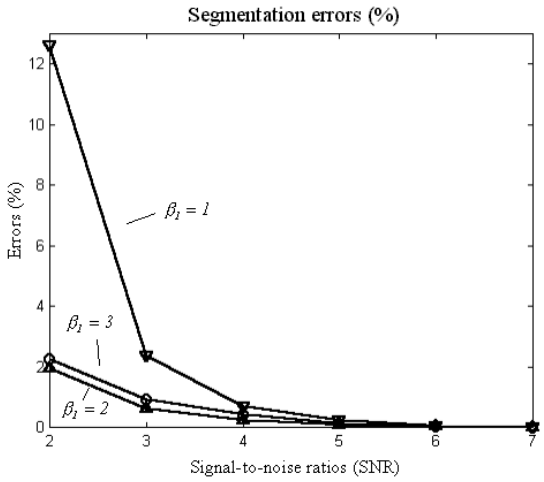

a. *Vertical straight tubes (8 voxel width)*

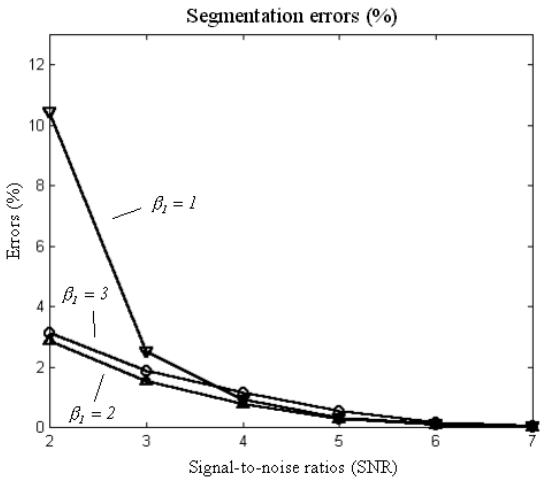

b. *Circular tubes (8 voxel width)*

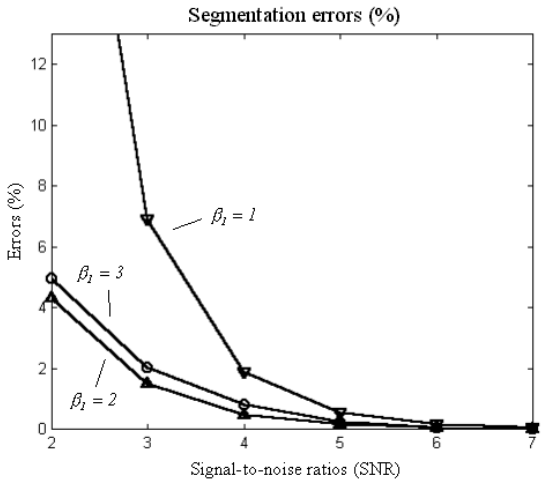

c. *Vertical straight tubes (4 voxel width)*

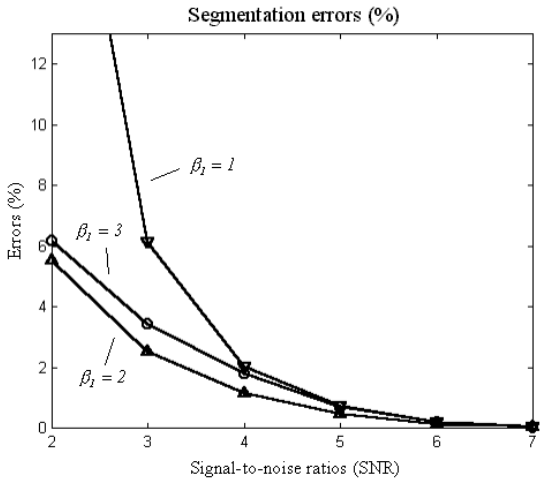

d. *Circular tubes (4 voxel width)*

Figure 4.4: *Segmentation errors on the 3D synthetic images (vertical and circular tubes). Different values of* $\beta_1 = 1, 2, 3$ *and fixed value of* $\beta_2 = 1$.

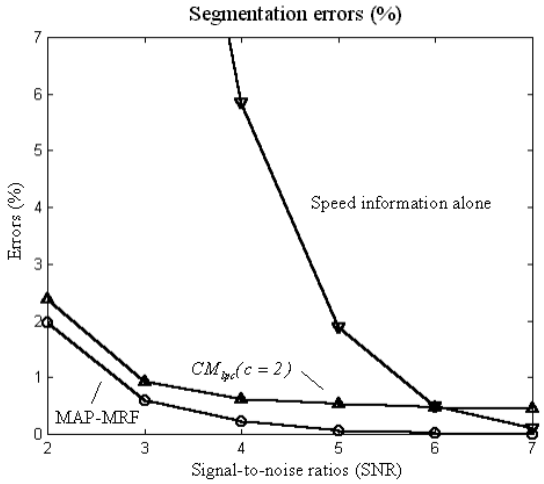

a. *Vertical straight tubes (8 voxel width)*

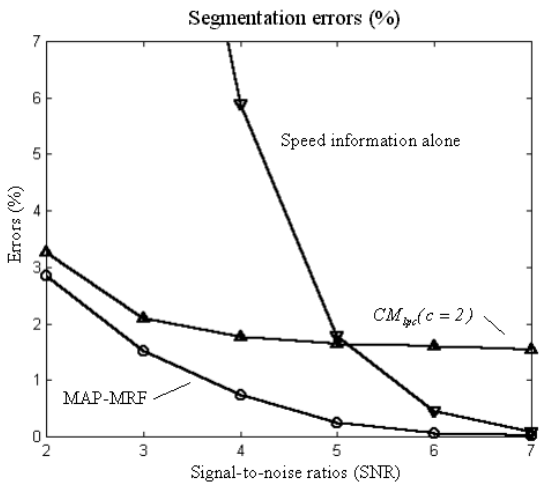

b. *Circular tubes (8 voxel width)*

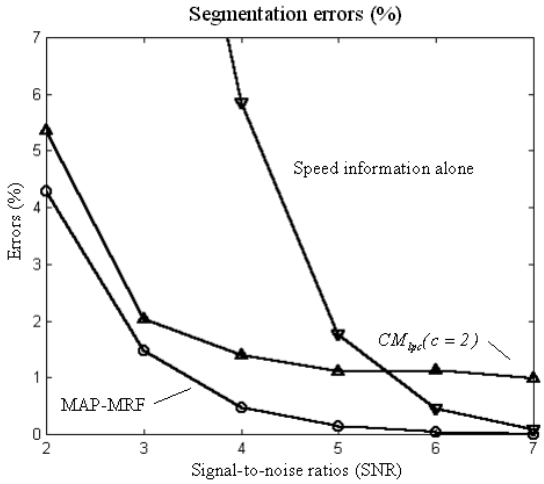

c. *Vertical straight tubes (4 voxel width)*

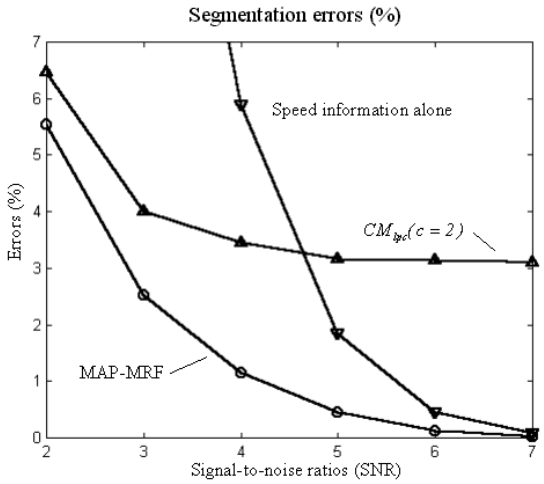

d. *Circular tubes (4 voxel width)*

Figure 4.5: *Comparison on the results based on (1) segmentation using speed information alone, (2) segmentation using flow coherence information alone, and (3) segmentation using both speed and flow coherence information. All segmentations were done on the 3D synthetic images (vertical and circular tubes).* $\beta_1 = 2$ *and* $\beta_2 = 1$.

4.4 Application to PC-MRA images

In this section, we apply the MAP-MRF approach to the segmentation of PC-MRA images. We begin by presenting an automatic threshold determination method for the classification of coherent and non-coherent voxels in the LPC map. Segmentation results on the PC-MRA images are then presented. Finally, the performance of the MAP-MRF method is evaluated by using a geometrically accurate tube.

4.4.1 Automated threshold determination for the LPC map

A typical LPC map and its histogram are shown and plotted in Figures 4.6a and 4.6b respectively. Note that the second order LPC measure, $CM_{lpc}(c = 2)$, is used and, therefore, the values of LPC range from -158 to 158. Figure 4.6b shows that the histogram is right-shifted and skewed.

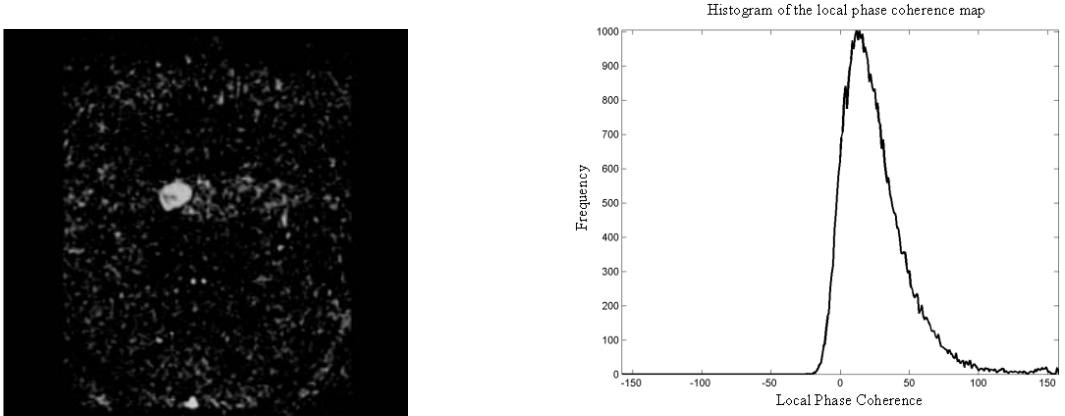

a. *Local phase coherence map.*

b. *Histogram of the local phase coherence map.*

Figure 4.6: *Local coherence map and its histogram.*

In fact, the LPC histogram can be described by three classes: background with low LPC, brain tissue with slightly higher LPC, and vessel with extremely high LPC, as illustrated in Figures 4.7a and 4.7b. The background (B) and brain tissue (T) histograms overlap heavily because of the non-stationary, but slightly coherent, motion of the non-vessel brain tissue. In contrast, the vessel (V) histogram is separated clearly from the background (B) and brain tissue (T) histogram. The point of separation - the desired threshold - is indicated approximately by an arrow in Figure 4.7b (midway between T and V histograms).

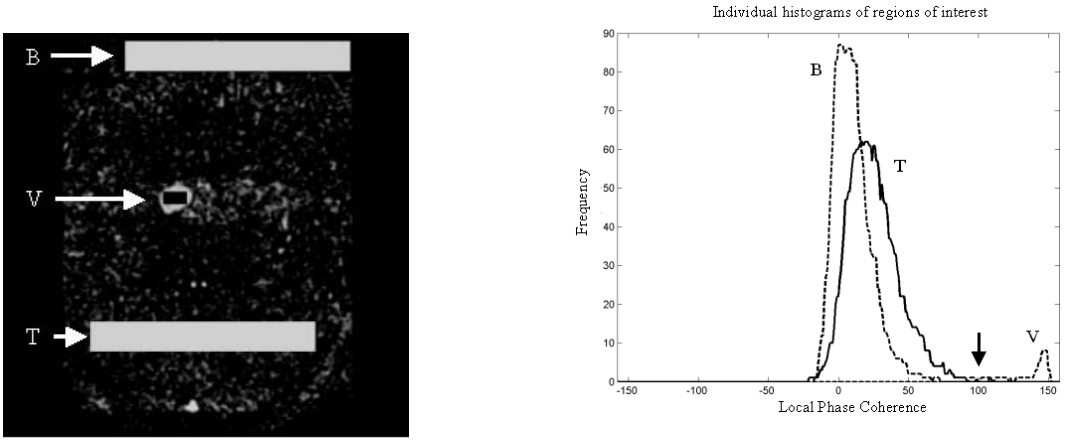

a. *Regions of interest.* **b.** *Individual histograms of regions of interest.*

Figure 4.7: *Regions of interest and their histograms.*

In a similar way to Chapter 2, where we model the background and vascular signals in PC-MRA speed images, in LPC maps, we model the background, brain tissue and vessel regions with three separate Gaussian distributions. It is worth noting that theoretical modelling of the LPC histogram is extremely difficult because of the high correlation between the velocity random variables, and normalisation and dot product operations of the correlated variables when the coherence measure is calculated. We again use the EM algorithm [10] to fit the LPC histogram by a mixture of the three Gaussian distributions. Figure 4.8a shows the fitting of the triple Gaussian model (dashed line). The individual histograms of the Gaussian distributions are shown in Figure 4.8b.

We define the mean and standard deviation of the brain tissue distribution as μ_T and σ_T respectively, and use $\mu_T + \alpha \cdot \sigma_T$ as the non-vessel threshold (we set α equal to 3 in this thesis). A voxel with LPC above the non-vessel threshold is labelled as a coherent voxel. Otherwise, it is labelled as a non-coherent voxel. As shown in Figure 4.9, the coherent voxels form a number of vessel 'clusters', though there are some randomly distributed voxels due to random coherent noise, small coherent motion of the non-vessel tissue during scanning and ghosting artifacts. These 'outliers' can be ignored if they are far away and disconnected from the vasculature, and their intensity values in a speed image are low.

4.4.2 Segmentation results on PC-MRA images

For the sake of comparison, two clinical PC-MRA images (as shown in Figures 4.10a and 4.11a) were processed using the speed information alone. As described in Chapter 2, by the

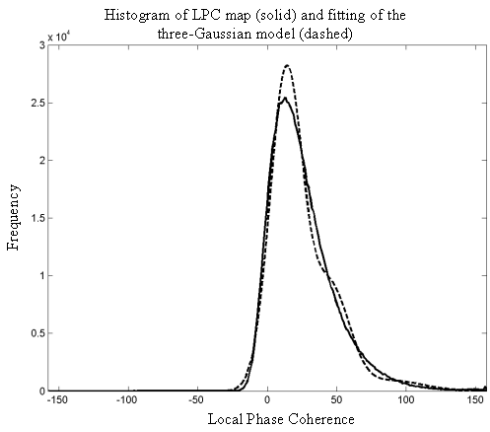

a. *Histogram of LPC map and fitting of the triple Gaussian model.*

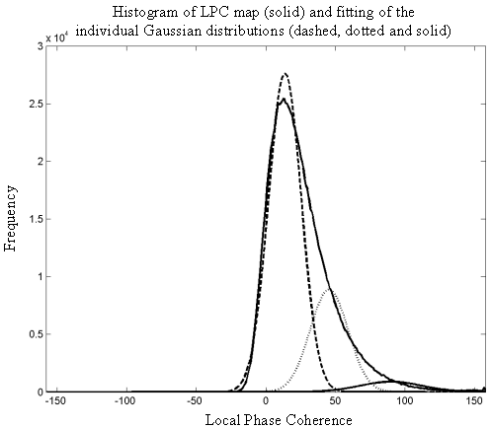

b. *Individual histograms of the Gaussian distributions.*

Figure 4.8: *LPC histogram and the triple Gaussian model.*

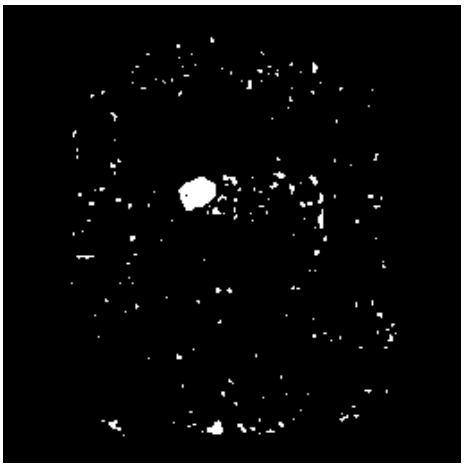

Figure 4.9: *Coherent voxels.*

results shown in Figures 4.10b and 4.11b, the aneurysms pointed at by the arrows are not completely segmented because of the low or complex flow inside the aneurysm. The results of applying the MAP-MRF segmentation algorithm combining speed and flow coherence information are shown in Figures 4.10c and 4.11c. It is clear that there are improvements in segmentation, especially inside the regions of the aneurysms. The differences between Figures 4.10b and 4.10c are highlighted in Figure 4.10d. Similarly, the differences between Figures 4.11b and 4.11c are highlighted in Figure 4.11d.

Note that there are few false negative voxels (two or three voxels) in the middle of the aneurysms. There are two major reasons for this. First, the flow rate was extremely low at the middle of the aneurysms, which can lead to serious corruption of the velocity field by noise. Secondly, a circular (or deformed circular) flow pattern was present with an associated singularity in the middle of the aneurysms. These factors affect the local phase coherence measure. However, the holes in the middle do not affect the quality of visualisation and can be removed easily. The segmentation processing time in these cases was fast, about 8 seconds per slice on a 500MHz PC (on average).

4.4.3 Performance of the MAP-MRF method

This section describes details of flow phantom experiments, and presents results related to a quantitative comparison between the MAP-MRF method and the segmentation based on speed information alone.

Flow phantom and measurement of error

The flow phantom is a geometrically accurate straight tube, which was made by using MR compatible materials (silicone elastomer, Sylgard 184, Dow Corning Corp, MI, USA). It was constructed using a lost metal technique based on a numerically controlled, milled mould [82]. The phantom provides accurately defined lumen dimensions, which are $8mm$ diameter and $400mm$ long for the tube within a silicon block of $400mm$ length and $100mm$ wide. The phantom was filled with saline flowing at a constant rate of $300mms^{-1}$. The phantom was scanned using the PC-MRA protocol on a 1.5T MR scanner (GE Sigma) at the Department of Neuroscience, King's College London, London. The image size was $256 \times 256 \times 40$ voxels and dimensions were $0.625 \times 0.625 \times 1.3mm^3$. The scan details were as follows: axial scan, TE/TR $= 7.3/20ms$, flip angle 18^o, 1 signal average, FOV: $22 \times 16cm^2$, VENCS: $400mms^{-1}$

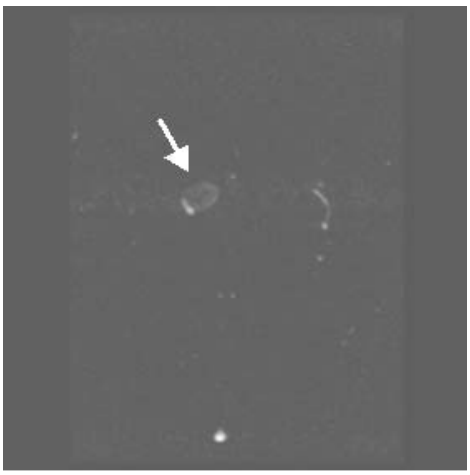

a. *Original speed image.*

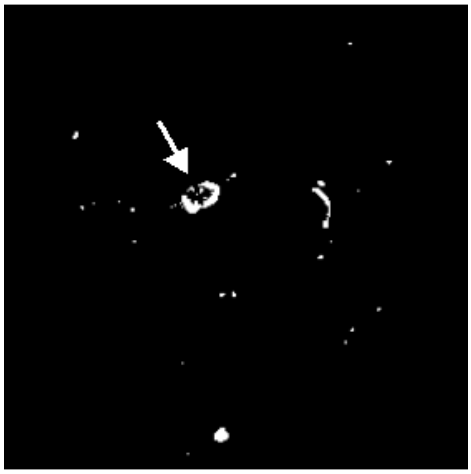

b. *Segmented image using speed information alone.*

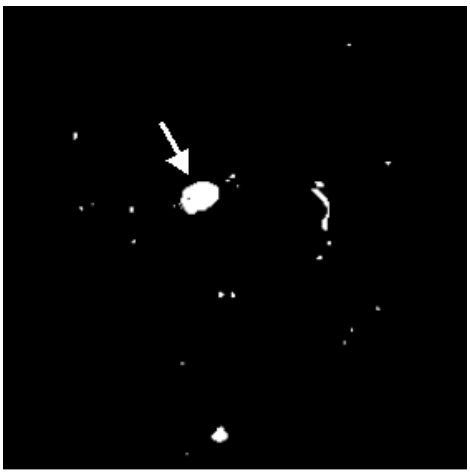

c. *Segmented image using speed and flow coherence information.*

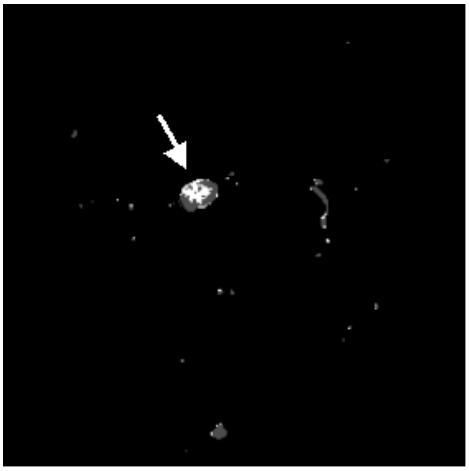

d. *Difference between (b) and (c).*

Figure 4.10: *Segmentation results and comparison.*

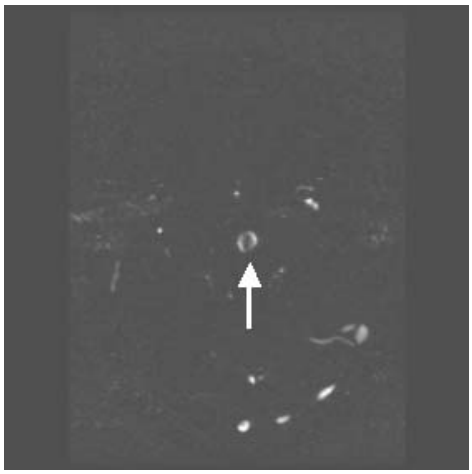

a. *Original speed image.*

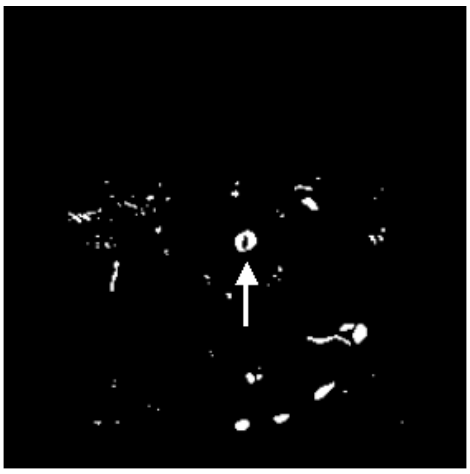

b. *Segmented image using speed information alone.*

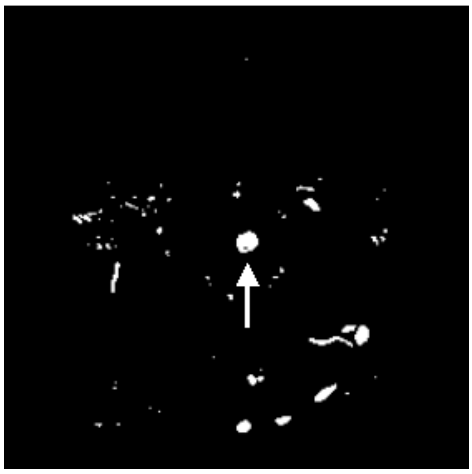

c. *Segmented image using speed and flow coherence information.*

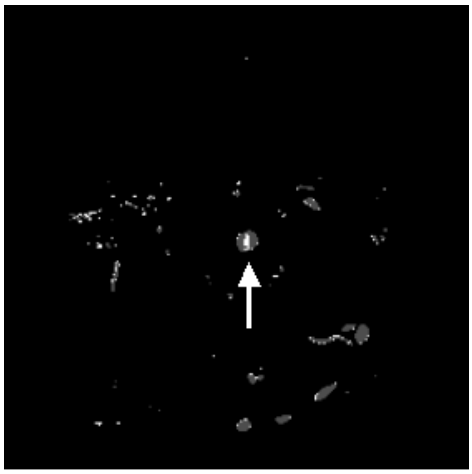

d. *Difference between (b) and (c).*

Figure 4.11: *Segmentation results and comparison.*

and acquisition matrix: 256×160 pixels.

Figure 4.12 shows a maximum intensity projection of the straight tube. The image has been cropped for the purpose of illustration. The left and right hand sides are the inflow and outflow regions respectively. Although the speed inside the tube remained constant during the experiments, the SNR was decreasing from the inflow region to the outflow region due to progressive saturation of fluid. Also, it is recognised that imperfections in velocity encoding due to non-linearities in the gradient systems can cause a position dependent deviation in the velocity images [7]. These two factors may influence the behaviour of the surface extraction method but were not taken into consideration in the experiments below.

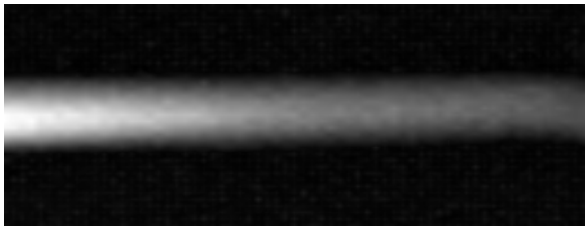

Figure 4.12: *Maximum intensity projection of the straight tube phantom. The left and right hand sides are the inflow and outflow regions respectively. (For the purpose of visualisation, the image has been interpolated linearly by adding 4 extra points between the sampled points.)*

We define the measurement error in a slice as the percentage difference between the estimated area and the true area of the straight tube,

$$\text{Error} = \frac{A_{estimated} - A_{true}}{A_{true}} \times 100\%, \tag{4.20}$$

where $A_{estimated}$ and A_{true} represent the estimated and true areas respectively. Since the true diameter is known ($8mm$), the true area A_{true} is $16\pi\ mm^2$. The estimated area $A_{estimated}$ is equal to the number of vessel voxels multiplied by the voxel size ($0.625^2\ mm^2$) in a slice. As such, the error is negative when $A_{estimated}$ underestimates the true area.

Results

Figure 4.13 shows the results of applying both methods on the straight tube flow phantom, where the area error defined in Equation 4.20 is used as the measure of comparison. This figure shows that the MAP-MRF based approach using both speed and flow coherence information gives higher segmentation accuracy (on average, -21.24% of the true area, underestimated)

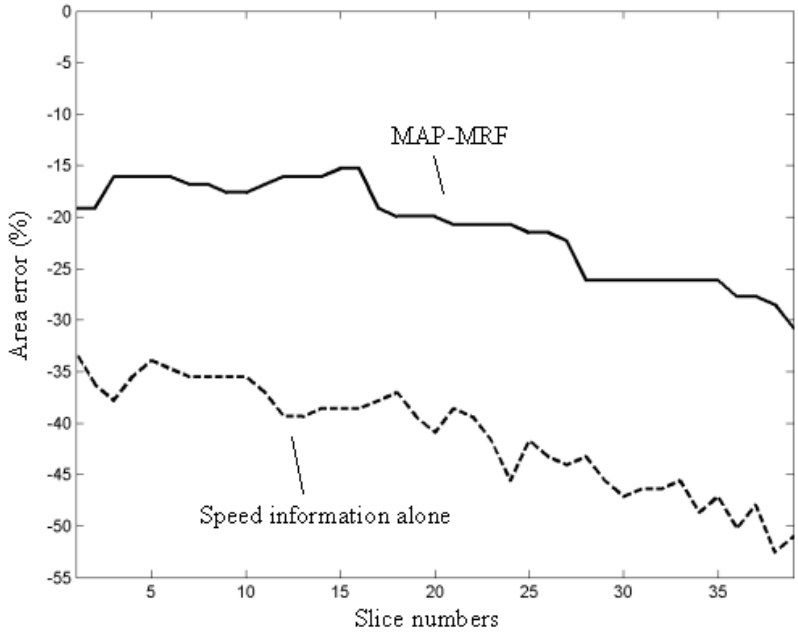

Figure 4.13: *This figure shows that the errors of area estimation (underestimation) are* -21.24% *and* -41.56% *for the MAP-MRF based approach and method using speed information alone respectively. The difference between two methods is* 20.32%.

than the segmentation method using speed information alone (on average, -41.56% of the true area, underestimated). The average difference between the two methods is 20.32%. Figure 4.14a shows an example speed image of the flow phantom data, in which the cross-section of the phantom is located at the centre. Figures 4.14b and 4.14c show the segmentation results of using speed information alone and the MAP-MRF method. The differences between these two images are highlighted and shown in Figure 4.14d, which reveals the advantage of using flow coherence information for segmenting the low SNR regions near the boundary of the tube.

4.5 Summary

As speed and flow coherence information appear to be inadequate when applied individually to segmenting objects with a wide range of SNR values, we have presented a general and efficient MAP-MRF framework for combining speed and flow coherence information for segmentation. Experiments on synthetic and clinical images show that the new method reduces segmentation errors across SNR values ranging from SNR $= 2$ to 7. Further, experiments on a geometrically

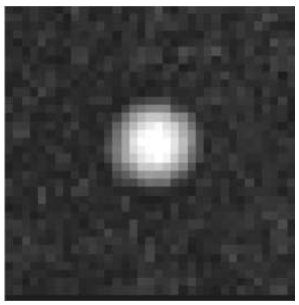

a. *Original speed image.*

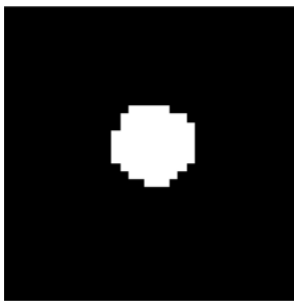

b. *Segmented image using speed information alone.*

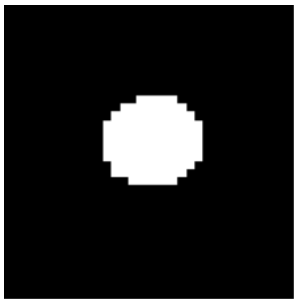

c. *Segmented image using speed and flow coherence information.*

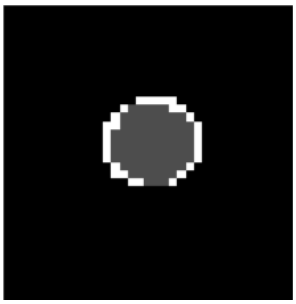

d. *Difference between (b) and (c).*

Figure 4.14: *Segmentation results and comparison.*

accurate straight tube shows that the MAP-MRF method is more accurate than the method using speed information alone by an average of 20.32%.

The new approach could be used not only for object segmentation with real flow patterns, but also applied to objects with flow-like patterns, e.g. for optical flow analysis. The flow magnitude and coherence in the optical flow field might provide useful cues for the segmentation of optical flow on a local level. A potential application could be for smoothing the flow field. This could be achieved by dividing the flow coherence field $\mathcal{O}$ into three separate MRFs for each directional component rather than a fixed field in the energy minimisation process in order to encourage smoothness of the flow vectors inside the object. A smoothness constraint similar to the continuity equation for an optical flow field [38] could be used. As such, a smooth flow field could be obtained in a unified and consistent probabilistic framework after segmentation.

Chapter 5

Surface extraction using a sub-voxel level set approach

5.1 Introduction

Extracting a surface from MRA data is clinically an important step because the extracted 3D surface provides a radiologist with essential visual and quantitative information about the 3D shape, size and position of an aneurysm and the vasculature in the vicinity of the aneurysm. This information is very useful for both diagnosis and treatment of aneurysms as well as other arterial diseases.

This chapter presents a variational framework for vascular reconstruction based on probabilities of vessel and background obtained by using an MRF model (Chapter 4), which itself exploits the physics-based MGU statistical model (Chapter 2) and the local phase coherence (LPC) measure (Chapter 3). Thus this chapter unifies all the ideas developed in this thesis so far. The framework employs the concept of region statistics in the vascular reconstruction process [89] and searches for an optimal surface by maximising the vascular and background posterior probabilities inside and outside a given surface respectively.

The framework is implemented by using a variation of the level set method [4]. It provides a number of attractive features, which are very useful in this application. Firstly, the vascular surface is represented implicitly in an Eulerian framework, rather than in a Lagrangian framework as in [20]. As such, parameterisation of the surface can be avoided. This greatly simplifies the implementation of the 3D surface extraction method and helps surface smoothing because surface curvature can be easily computed. Moreover, the level set method

is flexible in handling multiple objects and their topological changes. Secondly, unlike the standard level set method [66], the new implementation is run in sub-voxel resolution mode so that the extracted surface is located at the exact position, where the speed function $\mathcal{F}$ (or driving force) on the surface is equal to zero [4].

Traditionally, intensity gradient-based (or edge-based) approaches to vascular segmentation and reconstruction have been popular [57, 49, 84, 87] possibly because edge-based active contour methods have proved successful in other areas of medical image analysis. However, in PC-MRA images, due to the relatively low flow rate and the highly curved nature of many brain vessels, the true intracranial vessel boundaries may not have a high SNR or intensity gradient. Consequently, conventional edge-based methods often do not work well in this application. We will return to this point later in this chapter, where we compare the accuracy of the level-set MAP-MRF method with a level-set intensity gradient-based approach.

Experiments have been carried out using a geometrically accurate flow phantom. The results of the experiments show that (a) for PC-MRA images, surface boundaries extracted from the sub-voxel based method are clearly defined in a voxel and smoother than the voxel-based equivalent method (a typical result is shown in Figure 5.1), and the reconstruction accuracies of the sub-voxel level-set MAP-MRF method and the voxel-based equivalent method are comparable; and (b) the sub-voxel level set MAP-MRF method can achieve a higher reconstruction accuracy in PC-MRA images than a sub-voxel level-set intensity gradient-based approach.

a. **b.**

Figure 5.1: *A typical result of the flow phantom experiment is shown. (a) and (b) shown surface boundaries extracted by using the voxel-based level-set MAP-MRF approach and the sub-voxel level-set MAP-MRF approach respectively. It is observed that the surface boundary in (b) is clearly defined in a voxel and smoother than that in (a).*

5.2 Surface extraction based on vascular and background probabilities

To extend the segmentation developed in the preceding chapters, we consider a variational framework for vascular reconstruction. In this framework, a surface, which separates the vascular and background regions, is deformed in order to maximise the total probabilities of vessel and background inside and outside the surface. Using the divergence theorem, we derive the equation of surface motion given the initial surface.

Definitions: Let $\mathcal{S}(\vec{u},t)$ be a family of parameterised surfaces, where $\vec{u}$ and t are space and time parameters respectively, and $t \in [0,\infty)$. In 3D, $\vec{u} = (u,v) \in [0,1] \times [0,1]$ and $\mathcal{S}(\vec{u},t) : [0,1] \times [0,1] \times [0,\infty) \rightarrow \Re^3$. Let $I : \Omega \rightarrow \Re^+$ be an image volume, and Ω be an open set of $\Re^3$. We assume that there are two distinct regions (inside and outside the vasculature) in the image volume, which are separated by the surface $\mathcal{S}$. Let R_i and R_o be inside and outside regions representing the vascular region and background region respectively.

The vascular reconstruction is formulated as a global energy minimisation problem, which makes use of the intensity statistics of the inside and outside regions. The probabilistic energy functional $E_{prob}(t)$ is given by

$$E_{prob}(t) = \int_{R_i} -P_v \cdot dV + \int_{R_o} -P_b \cdot dV, \tag{5.1}$$

where dV is a volume element in the Euclidean space, P_v and P_b represent the posterior probabilities of the vessel and background at each voxel respectively, which are estimated by using the MRF model. Minimising the probabilistic energy E_{prob} represents finding an optimal surface for which the total posterior probability is at a maxima.

Given a surface $\mathcal{S}$, we apply the steepest-descent method to search for the local minimum of $E_{prob}(t)$, i.e. we look for a minimum of $E_{prob}(t)$ closest to $\mathcal{S}$ along the straight line in the direction of $-\frac{dE_{prob}(t)}{dt}$ [44]. According to Appendix C, a partial differential equation can be derived which governs the surface motion, and is given by

$$\frac{\partial \mathcal{S}}{\partial t} = (P_v - P_b)\ \hat{n}, \tag{5.2}$$

where $\hat{n}$ is the outward unit normal of the surface $\mathcal{S}$ and $-1 \leq P_v - P_b \leq 1$. We will refer to $P_v - P_b$ as the *"statistical force"*. Equation 5.2 describes a motion equation of the surface $\mathcal{S}$, which controls the motion of the surface towards the local minimum of $E_{prob}(t)$ over time. When convergence is reached, i.e. $\frac{dE_{prob}(t)}{dt} = 0$, the final surface describes the vascular shape.

Equation 5.2 can be implemented using the level-set method [78], which will be described in more detail in Section 5.3. The level set method requires an initial surface $\mathcal{S}_0 = \mathcal{S}(t = 0)$ as a starting point for the evolution equation of the surface $\mathcal{S}$. The choice of the initial surface can greatly affect the convergence rate as determined by Equation 5.2. In our case, we construct the initial surface $\mathcal{S}_0$ near the optimal solution using the voxel-based MAP method on the probabilistic maps of vessel and background obtained by using the MRF model. We have found that convergence of the evolution equation is usually reached after 8 iterations.

Our approach is related to work in 2D image segmentation proposed by Zhu-Yuille [89] and Paragios-Deriche [70], which minimises the negative logarithm of the posterior probability. Compared with their methods, there are two main advantages to our approach. The first is that it works in 3D. A proof of the applicability of the method to 3D is given in Appendix C. The second advantage is that our method provides a linear bound on the statistical force, $P_v - P_b \in [-1, 1]$, because we do not use logarithms of probability to define it, e.g. $logP_v - logP_b$. This means that the statistical force does not require normalisation and is stable even when the probabilities, P_v or P_b, are close to zero.

As proposed by Mumford and Shah [62], irregular boundaries (especially obtained from the probabilistic maps [89]) can be smoothed by introducing a smoothing term (also called a *regularising term*) to the minimisation problem. As such, a surface area energy term E_{area} is included for smoothing of the object shape, and is given by

$$E_{area}(t) = \int \int_{\mathcal{S}(\vec{u},t)} dA, \tag{5.3}$$

where $\mathcal{S}(\vec{u}, t)$ represents a simple, closed surface if t is fixed, dA is an element of area (in the Euclidean sense). Given a surface $\mathcal{S}$, we apply the steepest-descent method to search for the local minimum of $E_{area}(t)$. According to [77], we obtain a partial differential equation

$$\frac{\partial \mathcal{S}}{\partial t} = -\kappa \hat{n}, \tag{5.4}$$

where $\hat{n}$ is an outward unit normal to $\mathcal{S}$ and κ is the mean curvature in 3D, i.e.

$$\kappa = \frac{\kappa_1 + \kappa_2}{2}, \tag{5.5}$$

where κ_1 and κ_2 represent the maximum and minimum principal curvatures respectively [25]. Equation 5.4, therefore, describes a motion equation of the surface $\mathcal{S}$ for minimising the total surface area, which deforms the surface according to the magnitude of the mean

curvature along the normal direction. As such, motion of a highly curved surface patch will be encouraged, whereas motion of a flat surface (with low curvature) will be relatively small.

Finally, the total energy E_{total} is a weighted sum of the probabilistic energy E_{prob} and the smoothing energy E_{area}, which is given by

$$E_{total}(t) = W_{prob} \cdot E_{prob}(t) + W_{area} \cdot E_{area}(t), \tag{5.6}$$

where W_{prob} and W_{area} are weights attached to the respective energy terms. From Equations 5.2 and 5.4, the equation of motion becomes

$$\frac{\partial \mathcal{S}}{\partial t} = [\underbrace{W_{prob}(P_v - P_b)}_{Probabilistic\ term} - \underbrace{W_{area}\ \kappa}_{Smoothing\ term}\ ]\ \hat{n}, \tag{5.7}$$

where the first term is based on vessel and background probabilities and the second term is a smoothing term based on the surface curvature.

5.3 Level set methods

The level set method has been shown to be a promising approach, especially for 3D surface reconstruction of complex objects [51]. The major attractions of the level set method are (a) its simple and implicit form for representing the evolving surface, in an Eulerian framework which works in a fixed coordinate system, and (b) its flexibility in handling multiple objects and topological changes of the object surfaces. These factors make the implementation easier. Recently, level set methods have recently been extended to run in sub-voxel resolution so that the extracted surface is located at the exact position, where the speed function $\mathcal{F}$ on the surface is equal to zero [4]. In particular, as described in Equation 5.7, $\mathcal{F}$ relates to a difference between probabilities of vessel and background, and the surface curvature for regularisation. For the purpose of illustration, in this section, we briefly present the key ideas of the method in 2D. An extension of these ideas into 3D is then presented. A more detailed description of the methods can be found in [78].

Similar to the definitions in Section 5.2, let $\mathcal{C}(u,t)$ be a family of parameterised closed contours, where u and t are space and time parameters respectively, and $t \in [0,\infty)$. In 2D, $u \in [0,1]$ and $\mathcal{C}(u,t) : [0,1] \times [0,\infty) \rightarrow \Re^2$. The initial contour is given by $\mathcal{C}_0 = \mathcal{C}(u, t=0)$. Let $\mathcal{F}$ be a speed function defined on $\mathcal{C}$, which controls the speed of $\mathcal{C}$ in the normal direction. The speed function $\mathcal{F}$ needs to be recalculated after the position of $\mathcal{C}$ has been changed. The

equation of motion is given by

$$\frac{\partial \mathcal{C}}{\partial t} = -\mathcal{F}\hat{n}, \tag{5.8}$$

where $\hat{n}$ represents the outward unit normal to $\mathcal{C}$.

The concept of the 2D level set method is to build a 3D surface ϕ, which is one dimension higher than the number of dimensions of $\mathcal{C}$, and to represent $\mathcal{C}$ as a zero-level set of ϕ. This is illustrated in Figures 5.2a and 5.2b shows a cross-section of the surface ϕ. In general, motion of the contour can be tracked by the evolution of the level set function ϕ. Merging and splitting of the contour can also be handled naturally.

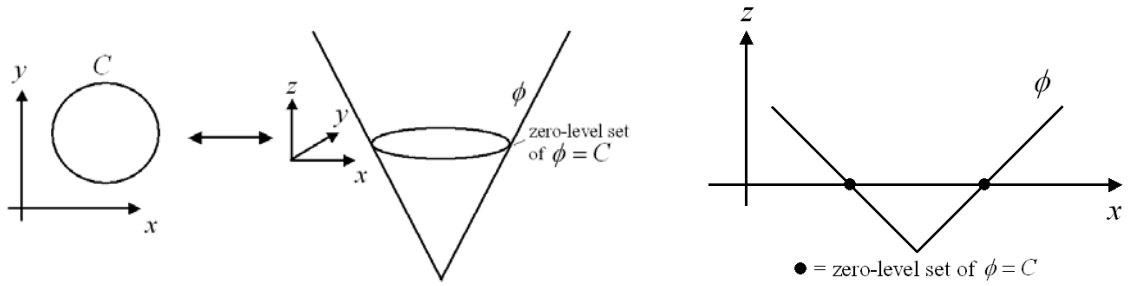

a. **b.**

Figure 5.2: *(a) In the level set method, a 2D contour is equivalent to a zero-level set of a 3D surface ϕ. (b) Cross-section of the level set function ϕ.*

According to [78], the level set function ϕ is commonly defined as a signed distance function, and is given by

$$\phi(x, y, t = 0) = \pm dis(x, y, \mathcal{C}_0), \tag{5.9}$$

where *dis* represents a distance function from a point (x, y) to the contour $\mathcal{C}_0$ which ensures that ϕ does not become too flat or too steep near the contour $\mathcal{C}_0$ [65] and ϕ is positive if the point is outside the contour and negative inside the contour. Also, ϕ satisfies $|\nabla\phi| = 1$ for simple and computationally fast initialisation of ϕ [78, 65]. By applying the chain rule of differentiation to Equation 5.9, the evolution equation of the level set function (and the contour) is given by

$$\phi_t + \mathcal{F}|\nabla\phi| = 0, \tag{5.10}$$

where an initial level set function $\phi(x, y, t = 0)$ is given and $\mathcal{F}$ can be any (positive or negative) speed function on the contour along the normal direction.

There are a number of geometric properties of the level set function ϕ, which can be easily

derived, according to [78]. For instance

$$\hat{n} = \frac{\nabla\phi}{|\nabla\phi|}, \tag{5.11}$$

$$\kappa = \nabla \cdot \frac{\nabla\phi}{|\nabla\phi|}, \tag{5.12}$$

where $\hat{n}$ represents the normal vector and κ is the curvature of each level set.

The extension to 3D is straightforward. The evolving surface $\mathcal{S}$ represented by Equation 5.7 is embedded implicitly as a zero level set of a four dimensional hypersurface $\phi : (x, y, z, t) \rightarrow \Re$ and t is any particular time, i.e.

$$\mathcal{S} = \{(x, y, z, t) \mid \phi(x, y, z, t) = 0\}, \tag{5.13}$$

where ϕ is a signed distance function and $|\nabla\phi| = 1$. The initial surface $\mathcal{S}_0$ is given by $\phi(x, y, z, t = 0) = 0$. At a fixed time t, $\phi < 0$ when (x, y, z) is inside the surface $\mathcal{S}$ and $\phi > 0$ when (x, y, z) is outside the surface $\mathcal{S}$. The deformation of the surface $\mathcal{S}$ is achieved by evolving the signed distance function ϕ. The definitions of the level set surface normal and curvature are given in Equations 5.11 and 5.12 respectively. In particular, the curvature κ in 3D is set to the mean curvature [78], which is given by

$$\begin{aligned}\kappa &= \nabla \cdot \frac{\nabla\phi}{|\nabla\phi|}, \\ &= \frac{(\phi_{yy} + \phi_{zz})\phi_x^2 + (\phi_{xx} + \phi_{zz})\phi_y^2 + (\phi_{xx} + \phi_{yy})\phi_z^2 - 2\phi_x\phi_y\phi_{xy} - 2\phi_x\phi_z\phi_{xz} - 2\phi_y\phi_z\phi_{yz}}{(\phi_x^2 + \phi_y^2 + \phi_z^2)^{3/2}}.\end{aligned} \tag{5.14}$$

Finally, Equation 5.7 can be rewritten in the level set formulation, which for our problem is given by

$$\phi_t + [W_{area}\ \kappa - W_{prob}(P_v - P_b)]\ |\nabla\phi| = 0. \tag{5.15}$$

It can be observed from the above Equation that, the surface deformation will stop if $W_{area}\ \kappa - W_{prob}(P_v - P_b) = 0$. In other words, the stopping criterion of the deforming surface is based on the region intensity statistics inside and outside of the propagating surface, and the surface curvature. However, if the smoothing term, $W_{area}\ \kappa$, is very small, the deformation will stop if the probability of vessel P_v is roughly equal to the probability of background P_b.

5.3.1 Numerical schemes for the level set methods

This section presents stable numerical schemes, as proposed by Sethian [78], for solving Equation 5.10, which is recalled here

$$\phi_t + \mathcal{F}|\nabla\phi| = 0,$$

where the initial level set function $\phi(x, y, t = 0)$ is given and $\mathcal{F}$ can be any (positive or negative) speed function on the contour. In our application, according to Equation 5.7, $\mathcal{F}$ will be equal to $[W_{area}\ \kappa - W_{prob}(P_v - P_b)]$.

It is assumed that the level set function ϕ is initialised as a signed distance function (more details about the initialisation will be given in Section 5.3.2). Let $\mathcal{F}_{xyz}$ and ϕ_{xyz} be the values of the speed function and level set function at a position (x, y, z) respectively. Further, let

$$D^{+x}u = \frac{u(x+\Delta x, y, z, t) - u(x, y, z, t)}{\Delta x}, \tag{5.16}$$

$$D^{-x}u = \frac{u(x, y, z, t) - u(x-\Delta x, y, z, t)}{\Delta x}, \tag{5.17}$$

$$D^{+y}u = \frac{u(x, y+\Delta y, z, t) - u(x, y, z, t)}{\Delta y}, \tag{5.18}$$

$$D^{-y}u = \frac{u(x, y, z, t) - u(x, y-\Delta y, z, t)}{\Delta y}, \tag{5.19}$$

$$D^{+z}u = \frac{u(x, y, z+\Delta z, t) - u(x, y, z, t)}{\Delta z}, \tag{5.20}$$

$$D^{-z}u = \frac{u(x, y, z, t) - u(x, y, z-\Delta z, t)}{\Delta z}, \tag{5.21}$$

where u is an arbitrary function and Δx, Δy, and Δz are one cell size in the x, y and z directions, respectively. The update of ϕ is given by

$$\phi^{n+1}_{xyz} = \phi^n_{xyz} - \Delta t[max(\mathcal{F}_{xyz}, 0)\nabla^+ + min(\mathcal{F}_{xyz}, 0)\nabla^-], \tag{5.22}$$

where n represents the iteration number, ϕ^n_{xyz} represents the value of ϕ at a position (x, y, z) after the n^{th} iteration, Δt denotes a time step for each iteration, and

$$\begin{aligned}\nabla^+ &= [max(D^{-x}\phi^n_{xyz}, 0)^2 + min(D^{+x}\phi^n_{xyz}, 0)^2 \\ &+ max(D^{-y}\phi^n_{xyz}, 0)^2 + min(D^{+y}\phi^n_{xyz}, 0)^2 \\ &+ max(D^{-z}\phi^n_{xyz}, 0)^2 + min(D^{+z}\phi^n_{xyz}, 0)^2]^{1/2}\ and\end{aligned} \tag{5.23}$$

$$\begin{aligned}\nabla^- &= [max(D^{+x}\phi^n_{xyz}, 0)^2 + min(D^{-x}\phi^n_{xyz}, 0)^2 \\ &+ max(D^{+y}\phi^n_{xyz}, 0)^2 + min(D^{-y}\phi^n_{xyz}, 0)^2 \\ &+ max(D^{+z}\phi^n_{xyz}, 0)^2 + min(D^{-z}\phi^n_{xyz}, 0)^2]^{1/2}.\end{aligned} \tag{5.24}$$

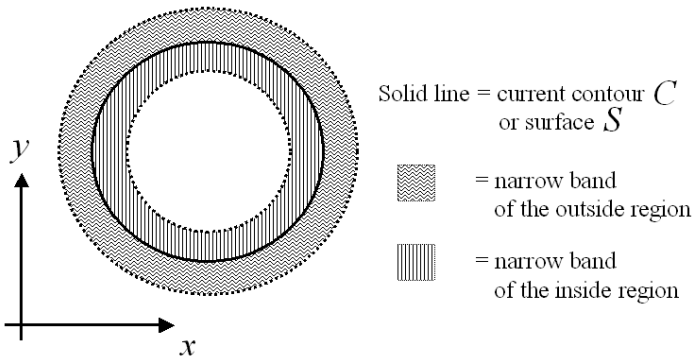

Figure 5.3: *This figure illustrates that, to increase the implementation speed, the narrow band method can be used to constrain propagation to a small surrounding region "near" the current contour or surface [3]. In our application, we set the narrow band as a two-voxel band for both inside and outside of the current surface, i.e. a 4 pixel width from the inside to outside of the surface, and let the narrow band regions (including interior and exterior narrow band regions) be* Ω'.

To increase the implementation speed, the narrow band method can be used to constrain propagation to a small surrounding region *"near"* the current contour or surface [3]. This is illustrated in Figure 5.3. In our application, we set the narrow band as a two-voxel band for both inside and outside of the current surface, i.e. a 4 pixel width from the inside to outside of the surface, and let the narrow band regions (including interior and exterior narrow band regions) be Ω'.

To ensure the stability of the numerical updates, a Courant, Friedrichs and Lewy (CFL) condition is employed to ensure that the surface will not advance more than one voxel in each time step [78]. Therefore, Δt is set in Equation 5.22 under the condition that

$$\max_{\Omega'} |\mathcal{F}\Delta t| \leq 1. \tag{5.25}$$

Since the value of $\mathcal{F}$ varies inside the narrow band regions, the value of Δt is set according to Equation 5.25 after all voxels in the narrow band regions are scanned.

5.3.2 Building ϕ and $\mathcal{F}$ to sub-voxel accuracy

As mentioned earlier, the motion of a contour or surface can be tracked by the evolution of the level set function ϕ, which is updated according to Equation 5.22. The level set function ϕ and speed function $\mathcal{F}$ need to be re-built or re-initialised after every numerical update (or

a certain number of updates). This is because, after several numerical updates, the signed distance condition, $|\nabla\phi| = 1$, of ϕ may be violated. Also, since the surface is advancing from the current position, the speed function will no longer reflect the true speed values.

Previous sub-voxel implementations have been presented (e.g. [4, 78]) mainly for the 2D case. However we present a method for building the level set function ϕ and the speed function $\mathcal{F}$ to sub-voxel accuracy in 3D. There are two benefits to running at sub-voxel resolution. Firstly, the stopping position of the level set function ϕ can be calculated accurately according to Equation 5.15. As such, the final position of the evolving surface will be placed exactly in a voxel where $W_{area}\ \kappa - W_{prob}(P_v - P_b) = 0$. Secondly, the evolving surface will not oscillate near the energy minimum position, i.e. the surface will stop at the exact position where the total energy term is at a minima.

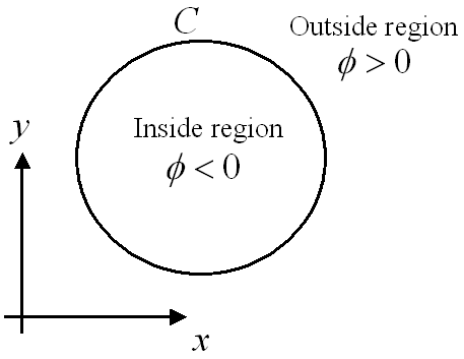

Figure 5.4: *The re-initialisation process is divided into two sub-processes. One for the outside region of the contour $\mathcal{C}$ in 2D or surface $\mathcal{S}$ in 3D and another for the inside region.*

We divide the re-initialisation process into two sub-processes. One for outside region of the contour or surface and another for inside region, as shown in Figure 5.4. We will present only the sub-process for the outside region as the corresponding sub-process for the inside region can be implemented analogously.

We follow loosely the notations in [4], let ϕ^n be the current level set function after the n^{th} iteration of the numerical update, and ϕ^{temp} be the re-initialised level set function. Also, assume that ϕ^n does not satisfy the condition, $|\nabla\phi| = 1$, of the signed distance function. The goals of the rebuild are then as follows. Firstly, the level set function ϕ^{temp} will be re-initialised so that the signed distance condition is satisfied. Secondly, once the value of ϕ^{temp} is calculated, the magnitude of the speed function $\mathcal{F}$ on ϕ^{temp} can then be computed based on the true speed values.

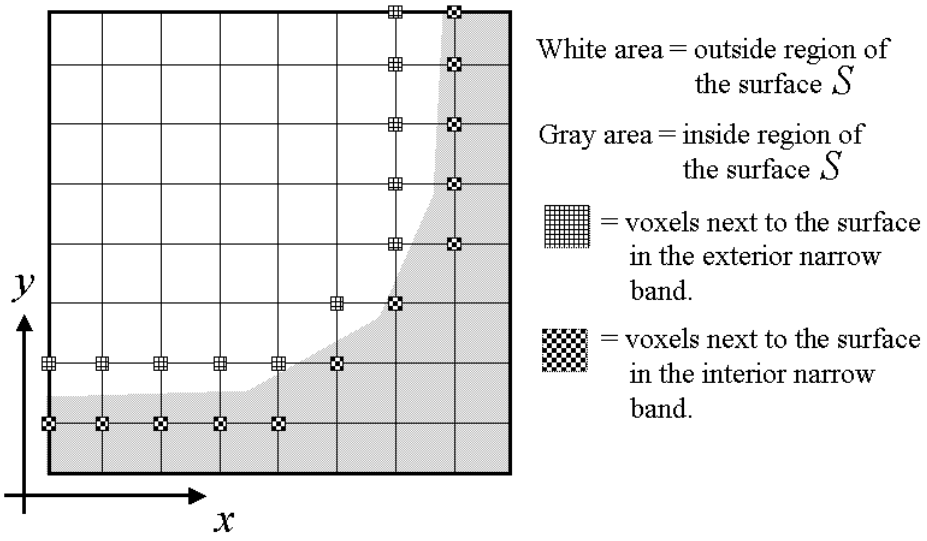

Figure 5.5: *Illustration of a contour or surface at the narrow band voxels (within one voxel distance).*

inside or outside of the contour.

First of all, we identify all voxels located next to the surface (within one voxel distance), as shown in Figure 5.5. For each of these voxels, we compute the exact distance from the voxel to the surface based on its immediate neighbours within one voxel distance. For example, consider the 2D case, as shown in Figure 5.6a. Here the inside region of the surface is illustrated with grey colouring, the coordinates of the centre voxel are (x, y); the centre voxel is next to and outside the surface; and r and s represent the distances from the centre voxel to the surface along the x and y directions respectively. The closest distance ϕ^{temp} from (x, y) to the surface should satisfy

$$\left(\frac{\phi^{temp}}{r}\right)^2 + \left(\frac{\phi^{temp}}{s}\right)^2 = 1. \tag{5.26}$$

Another example is shown in Figure 5.6b, where ϕ^{temp} satisfies

$$\left(\frac{\phi^{temp}}{r}\right)^2 + \left(\frac{\phi^{temp}}{min(s_1, s_2)}\right)^2 = 1. \tag{5.27}$$

Let q be the distance to the surface along the z axis direction,

$$\eta_x = \begin{cases} 1, & if\ r_1 \leq \Delta x\ or\ r_2 \leq \Delta x, \\ 0, & otherwise, \end{cases} \tag{5.28}$$

$$\eta_y = \begin{cases} 1, & if\ s_1 \leq \Delta y\ or\ s_2 \leq \Delta y, \\ 0, & otherwise, \end{cases} \tag{5.29}$$

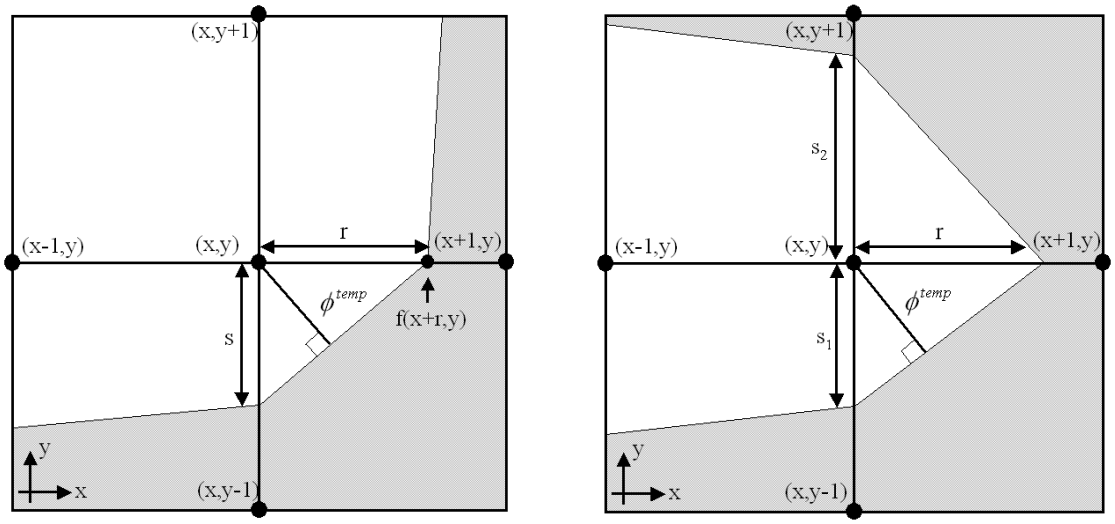

a. **b.**

Figure 5.6: *Two examples showing a voxel next to the surface $\mathcal{S}$ (inside region of the surface is gray in colour) and its distances, r and s, to the surface along the x and y axis directions respectively.*

$$\eta_z = \begin{cases} 1, & if\ q_1 \leq \Delta z\ or\ q_2 \leq \Delta z, \\ 0, & otherwise, \end{cases} \tag{5.30}$$

where the functions η_x, η_y and η_z act as the switch functions, which are turned on if the surface is within one voxel distance away from the current position in the respective directions. In 3D, the value of ϕ^{temp} should satisfy

$$\eta_x \left(\frac{\phi^{temp}}{r}\right)^2 + \eta_y \left(\frac{\phi^{temp}}{s}\right)^2 + \eta_z \left(\frac{\phi^{temp}}{q}\right)^2 = 1, \tag{5.31}$$

where $r = min(r_1, r_2)$, $s = min(s_1, s_2)$ and $q = min(q_1, q_2)$. Hence, we get

$$\phi^{temp} = \pm \sqrt{\frac{1}{\left(\frac{\eta_x}{r}\right)^2 + \left(\frac{\eta_y}{s}\right)^2 + \left(\frac{\eta_z}{q}\right)^2}}, \tag{5.32}$$

where ϕ^{temp} is positive for regions outside the surface and negative for regions inside the surface.

After all the voxels near the surface (within one voxel distance) have been initialised, we need to initialise the values of the speed function $\mathcal{F}$ near the surface S based on the true speed values f of the voxels [3]. In our application, the true speed value f will be equal to $[W_{area}\ \kappa - W_{prob}(P_v - P_b)]$ according to Equation 5.15. The speed function $\mathcal{F}$ based on f should then have zero value in the entire volume.

We now present a method, based on [3], for initialising the values of the speed function $\mathcal{F}$ near the surface S. A condition $\nabla\mathcal{F}\cdot\nabla\phi^{temp}=0$ is employed to ensure that the direction of change of speed function is perpendicular to the direction of the change of ϕ^{temp}. Therefore, all voxels along the normal direction of the current surface will evolve at the same speed, which is very useful for maintaining the stability of the method [4, 30].

In order to satisfy the condition $\nabla\mathcal{F}\cdot\nabla\phi^{temp}=0$, the value of the speed function f at voxel (x,y,z) should satisfy

$$\eta_x\cdot\frac{\partial\mathcal{F}}{\partial x}\cdot\frac{\partial\phi^{temp}}{\partial x}+\eta_y\cdot\frac{\partial\mathcal{F}}{\partial y}\cdot\frac{\partial\phi^{temp}}{\partial y}+\eta_z\cdot\frac{\partial\mathcal{F}}{\partial z}\cdot\frac{\partial\phi^{temp}}{\partial z}=0,$$

$$\frac{\eta_x(\mathcal{F}-f_r)}{r}\cdot\frac{\phi^{temp}}{r}+\frac{\eta_y(\mathcal{F}-f_s)}{s}\cdot\frac{\phi^{temp}}{s}+\frac{\eta_z(\mathcal{F}-f_q)}{q}\cdot\frac{\phi^{temp}}{q}=0, \tag{5.33}$$

where η_x, η_y and η_z are defined in Equations 5.28, 5.29 and 5.30 respectively; and r, s and q are defined in Equation 5.31;

$$f_r=\begin{cases} f(x-r_1,y,z), & if\ r_1\le r_2,\\ f(x+r_2,y,z), & otherwise,\end{cases} \tag{5.34}$$

$$f_s=\begin{cases} f(x,y-s_1,z), & if\ s_1\le s_2,\\ f(x,y+s_2,z), & otherwise,\end{cases} \tag{5.35}$$

$$f_q=\begin{cases} f(x,y,z-q_1), & if\ q_1\le q_2,\\ f(x,y,z+q_2), & otherwise,\end{cases} \tag{5.36}$$

The values of f are interpolated linearly from the neighbouring values on the grid, e.g. as shown in Figure 5.6b, the value of $f(x,y-s_1,z)$ is obtained by linearly interpolating the values between $f(x,y,z)$ and $f(x,y-\Delta y,z)$. Hence, re-arranging terms in Equation 5.33, we obtain

$$\mathcal{F}=\frac{\frac{\eta_x f_r}{r^2}+\frac{\eta_y f_s}{s^2}+\frac{\eta_z f_q}{q^2}}{\frac{\eta_x}{r^2}+\frac{\eta_y}{s^2}+\frac{\eta_z}{q^2}}. \tag{5.37}$$

For example, in the sample shown in Figure 5.6b, Equation 5.33 would become

$$\frac{(\mathcal{F}-f(x+r,y,z))}{r}\cdot\frac{\phi^{temp}}{r}+\frac{(\mathcal{F}-f(x,y-s_1,z))}{s_1}\cdot\frac{\phi^{temp}}{s_1}=0, \tag{5.38}$$

After all speed function values $\mathcal{F}$ and level set function values ϕ^{temp} of the voxels near the surface are calculated, the values $\mathcal{F}$ of other voxels in the exterior narrow band region can then be computed, according to the condition $\nabla\mathcal{F}\cdot\nabla\phi^{temp}=0$, while building the level set function ϕ^{temp} for other voxels in the exterior narrow band region. The fast marching

methods are used to initialise (a) the values of ϕ^{temp} under the condition $|\nabla\phi^{temp}| = 1$ and (b) the speed function values $\mathcal{F}$ under the condition $\nabla\mathcal{F} \cdot \nabla\phi^{temp} = 0$ in the exterior narrow band region [78].

For example, in 3D, if ϕ^{temp}_{xyz} at a position (x, y, z) is computed based on the values of $\phi^{temp}_{(x-1)yz}$, $\phi^{temp}_{x(y-1)z}$ and $\phi^{temp}_{xy(z-1)}$ by the fast marching method according to the condition $|\nabla\phi^{temp}| = 1$, then the value of $\mathcal{F}_{xyz}$ should satisfy $\nabla\mathcal{F} \cdot \nabla\phi^{temp} = 0$ and, therefore,

$$\frac{\mathcal{F}_{xyz} - \mathcal{F}_{(x-1)yz}}{\Delta x} \cdot \frac{\phi^{temp}_{xyz} - \phi^{temp}_{(x-1)yz}}{\Delta x} + \frac{\mathcal{F}_{xyz} - \mathcal{F}_{x(y-1)z}}{\Delta y} \cdot \frac{\phi^{temp}_{xyz} - \phi^{temp}_{x(y-1)z}}{\Delta y} + \frac{\mathcal{F}_{xyz} - \mathcal{F}_{xy(z-1)}}{\Delta z} \cdot \frac{\phi^{temp}_{xyz} - \phi^{temp}_{xy(z-1)}}{\Delta z} = 0. \tag{5.39}$$

Then $\mathcal{F}_{xyz}$ is given by

$$\mathcal{F}_{xyz} = \frac{\frac{\mathcal{F}_{(x-1)yz}}{\Delta x^2} + \frac{\mathcal{F}_{x(y-1)z}}{\Delta y^2} + \frac{\mathcal{F}_{xy(z-1)}}{\Delta z^2}}{\frac{1}{\Delta x^2} + \frac{1}{\Delta y^2} + \frac{1}{\Delta z^2}}. \tag{5.40}$$

The same procedure described above is repeated for the inside region of the surface after all voxels in the exterior narrow band region have been rebuilt. If the values of ϕ^{temp} and $\mathcal{F}$ are calculated for all voxels in the exterior and interior narrow band regions, then ϕ^{temp} is copied into ϕ^{n+1} for the next numerical update, as given by Equation 5.22, based on ϕ^{n+1} and $\mathcal{F}$.

5.4 Surface extraction based on intensity gradient

For the sake of comparison between the conventional intensity gradient-based approach and sub-voxel based level-set MAP-MRF method, this section begins by briefly introducing a level-set intensity gradient-based surface extraction method, and then discusses its potential problems for extracting object surfaces in PC-MRA images.

5.4.1 Geodesic active surfaces driven by a gradient function

The concept behind geodesic active surfaces is to minimise the weighted area of a surface by deforming the surface towards the lower weighted surface area direction [77]. The model was originally introduced by Malladi et al. [51] and Caselles et al. [17] in 2D for object boundary detection and reconstruction, and has been subsequently extended to 3D by Yezzi et al. [88] amongst others. A good discussion on geodesic methods can be found in [77].

In general, the geodesic active surface is attracted towards object boundaries by minimising the weighted area of the surface. The weight function becomes zero (or extremely small) when the surface arrives at the object boundary. Using the notation from Section 5.2, the weighted surface area is given by

$$A(t) = \int \int_{\mathcal{S}(\vec{u},t)} g(|\nabla \hat{I}|) dA, \tag{5.41}$$

where $\mathcal{S}(\vec{u}, t)$ represents a simple, closed surface if t is fixed, dA is an element of area in Euclidean space and $g(|\nabla \hat{I}|)$ is a function of intensity gradient, which is a monotonically decreasing function and becomes zero as the intensity gradient $|\nabla \hat{I}|$ tends to infinity, i.e. $g(|\nabla \hat{I}|) \to 0$ as $|\nabla \hat{I}| \to \infty$. If t is fixed, $A(t)$ gives the weighted surface area depending on the shape of the surface and the gradient function g. g is commonly chosen as

$$g(|\nabla \hat{I}|) = \frac{1}{1 + |\nabla \hat{I}|^p}, \tag{5.42}$$

where $\hat{I}$ is a smoothed version of I, e.g. a Gaussian filtered image, $p \in \Re$, and $|\nabla \hat{I}|$ is the intensity gradient of $\hat{I}$ [51, 17, 70].

Given a surface $\mathcal{S}$, we apply the steepest-descent method to search for the local minimum of $A(t)$, as given in Equation 5.41 [44]. According to [77], we obtain a partial differential equation

$$\frac{\partial \mathcal{S}}{\partial t} = -(g\kappa + \nabla g \cdot \hat{n})\hat{n}, \tag{5.43}$$

where $g = g(|\nabla \hat{I}|)$ for simplicity of notation, $\hat{n}$ is an outward unit normal to $\mathcal{S}$, κ is the mean curvature in 3D and is defined in Equation 5.5. The equivalent level set formulation of Equation 5.43 is given by

$$\frac{\partial \phi}{\partial t} + \left(g\kappa + \nabla g \cdot \frac{\nabla \phi}{|\nabla \phi|} \right) |\nabla \phi| = 0. \tag{5.44}$$

Recalling from Equation 5.10, the speed function $\mathcal{F}$ is equivalent to $\left(g\kappa + \nabla g \cdot \frac{\nabla \phi}{|\nabla \phi|} \right)$ in Equation 5.44. Similarly, the Equation 5.44 is solved by using the numerical scheme, as given in Equation 5.22 (Section 5.3.1).

Equation 5.43 describes a motion equation of the surface $\mathcal{S}$, which controls the deformation of the surface towards the local minimum of $A(t)$ over time. When convergence is reached, i.e. $\frac{dA(t)}{dt} = 0$, the surface at this point in time describes the object shape.

As such, in the model of geodesic active surfaces, it is normally assumed that the true object boundary has a high image gradient which delineates the shape of the object. However, for PC-MRA images, this is not the case and is discussed in detail in the next subsection.

5.4.2 Problems with the gradient-based approach applied to PC-MRA images

This subsection discusses problems with object reconstruction based on the intensity gradient function in PC-MRA images. In order to illustrate the problem, Figure 5.7a shows a PC-MRA speed image of the cross-section of a 8mm-diameter straight tube, which have been described in Section 4.4.3. The image size is 35×35 pixels and the resolution is $0.625 \times 0.625mm^2$. Figure 5.7b plots an intensity profile along the white horizontal line drawn in Figure 5.7a. From the intensity profile, it is observed that the left and right tube boundaries are roughly located at the pixel positions 12 and 25 respectively.

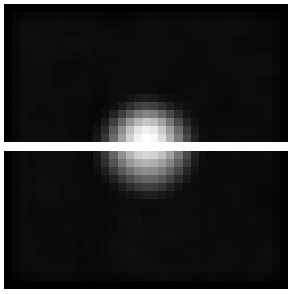

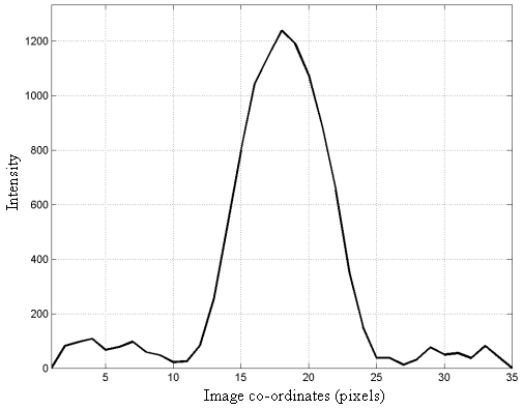

a. **b.**

Figure 5.7: *(a) A speed image of the cross-section of a 8mm-diameter straight tube, which is a geometrically accurate MR flow phantom with fluid running inside at a constant flow rate of* $300mms^{-1}$*. (b) The intensity profile along the white horizontal line shown in (a). From the intensity profile, it is observed that the left and right tube boundaries are roughly located at the pixel positions 12 and 25 respectively.*

We used a Gaussian filter (with a standard deviation set to 2) to smooth the speed image shown in Figure 5.7a . The intensity profile of the smoothed image $\hat{I}$ is shown in Figure 5.8a. Figure 5.8b plots the gradient values $|\nabla \hat{I}|$ of the intensity profile shown in Figure 5.8a. We employed the gradient function $g(|\nabla \hat{I}|)$ defined in Equation 5.42 and set $p = 0.01$ to achieve the highest contrast between the maximum and minimum of the gradient function values. A plot of the gradient function is shown in Figure 5.8c. This reveals that the minimum values of the gradient function are located at pixel positions 14 and 22 (pointed to by the arrows), which are located clearly inside the tube and are different from the observed tube boundaries

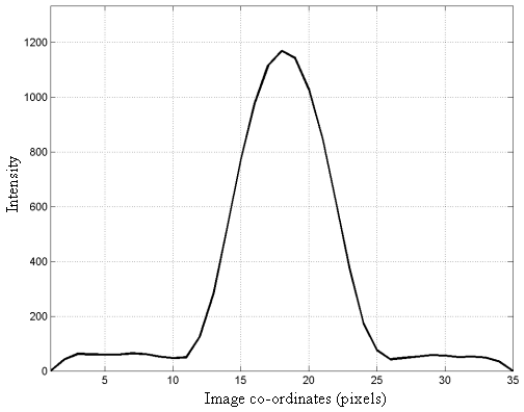

a.

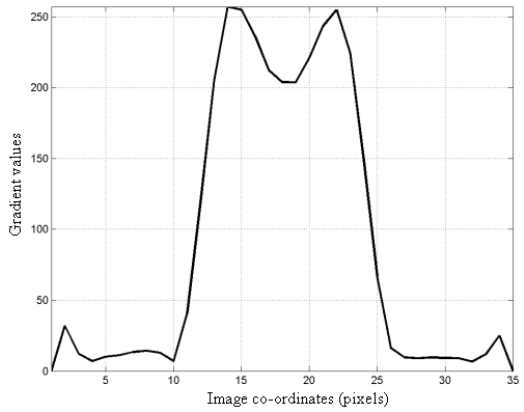

b.

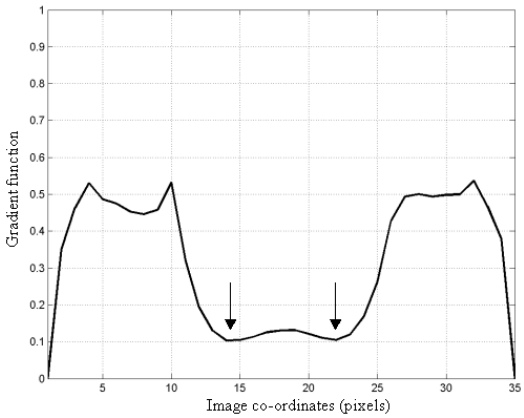

c.

Figure 5.8: *(a) Intensity profile of the smoothed image $\hat{I}$ of Figure 5.7a. (b) Gradient values $|\nabla \hat{I}|$ and (c) the corresponding gradient function $g(|\nabla \hat{I}|)$ of the smoothed intensity profile in (a). The arrows in (c) indicate the boundary positions located by the level-set intensity gradient-based approach.*

as shown in Figure 5.7b.

This is because the SNR is low, and there is a low rate of change of intensity values, near the boundary of the tube, which do not produce a sufficiently high gradient function for boundary detection. The low SNR and low rate of change of intensity values can be caused partly by the boundary layer[1] of the fluid flow.

We conclude from the above observation that an intensity gradient-based approach may not accurately detect the true tube (or vessel) boundary in PC-MRA speed images. A quantitative comparison between the sub-voxel level-set intensity gradient-based approach and the sub-voxel MAP-MRF approach will be presented next.

5.5 Experimental results

Based on the flow phantom experiments described in Section 4.4.3 in the previous chapter, this section presents results related to a quantitative comparison (a) between voxel and sub-voxel versions of the level-set MAP-MRF method and (b) between the sub-voxel level-set MAP-MRF method (Sections 5.2 and 5.3), and a sub-voxel level-set intensity gradient-based approach as described in Section 5.4.1. Note that a very similar voxel-based level-set intensity gradient-based approach has also been proposed and implemented by Lorigo et al. [49] for analysis of PC-MRA images.

Given an extracted surface $\mathcal{S}$, we define the measurement error in a slice as the percentage difference between the estimated area and the true area of the straight tube,

$$Error(\mathcal{S}) = \frac{A_{estimated}(\mathcal{S}) - A_{true}}{A_{true}} \times 100\%, \tag{5.45}$$

where $A_{estimated}(\mathcal{S})$ and A_{true} represent the estimated and true areas respectively. Recalling from Section 4.4.3, the true area A_{true} of the tube is $16\pi\ mm^2$. The estimated area $A_{estimated}(\mathcal{S})$ is equal to the number of voxels inside or on the extracted surface $\mathcal{S}$ multiplied by the voxel size in a slice. As such, the error $Error(\mathcal{S})$ is negative when $A_{estimated}(\mathcal{S})$ underestimates the true area. This error estimate will be used in subsequent analysis in Sections 5.5.1 and 5.5.2.

[1]The boundary layer of the fluid flow is a transition region, very close to the physical boundary of the tube (or vessel in our application) in which the fluid velocity increases rapidly from zero at the boundary to approach the velocity of the main stream in the tube.

5.5.1 Comparison between methods running in voxel resolution and sub-voxel resolution

We compared the performance between the level-set MAP-MRF methods running at (a) voxel resolution and (b) sub-voxel resolution. Both methods are based on the probabilities of vessel and background, estimated by using the MRF model (Chapter 4). The voxel-based method runs on the probabilistic maps and classifies voxels based on the MAP method in the image volume. The sub-voxel based method employs the level set method to deform the surface obtained from the probabilistic maps (posterior probabilities of the vessel and background) and positions the surface within voxels according to the probabilities in the neighbouring voxels and the local surface curvature. The sub-voxel based method was initialised with the surface of the voxel based method. After a local minimum was reached and the deformation of the surface terminated, the original volume was interpolated linearly by adding 4 extra points between any two voxel positions. The optimal surface was then extracted and regions inside represented vessels and outside represented background.

We empirically set the weights W_{prob} and W_{area} in Equation 5.7 equal to 1 and 0.1 respectively because, according our experience, W_{area} is set smaller than W_{prob} in order to preserve as much of the original shape as possible.

As shown in Figures 5.9a and 5.9b, the boundary extracted by the sub-voxel based method is clearly defined according to the probabilities of vessel and background, and smoother than the voxel-based method. A good and clear definition of surface boundary is important because it could help to improve measurements of the diameter and neck size of an aneurysm. Figure 5.10 shows that the area error estimations (underestimation) are -21.24% and -20.27% for the methods running in voxel and sub-voxel resolution respectively, which reveals that the accuracies of the sub-voxel based method and the voxel based method are comparable. Moreover, for the same experiment, Figure 5.11 shows the sum of the vascular probabilities inside and background probabilities outside of the surface, and demonstrates that convergence is reached quickly after one iteration (if a 0.1% of change is used as the threshold to indicate convergence), but also a small change is observed after a few iterations because of the surface adjustments caused by the curvature-based smoothing term. As such, in practice, we set the number of iterations to 8. For this dataset, it takes 5 seconds for $35 \times 133 \times 40$ voxels on a 500MHz PC.

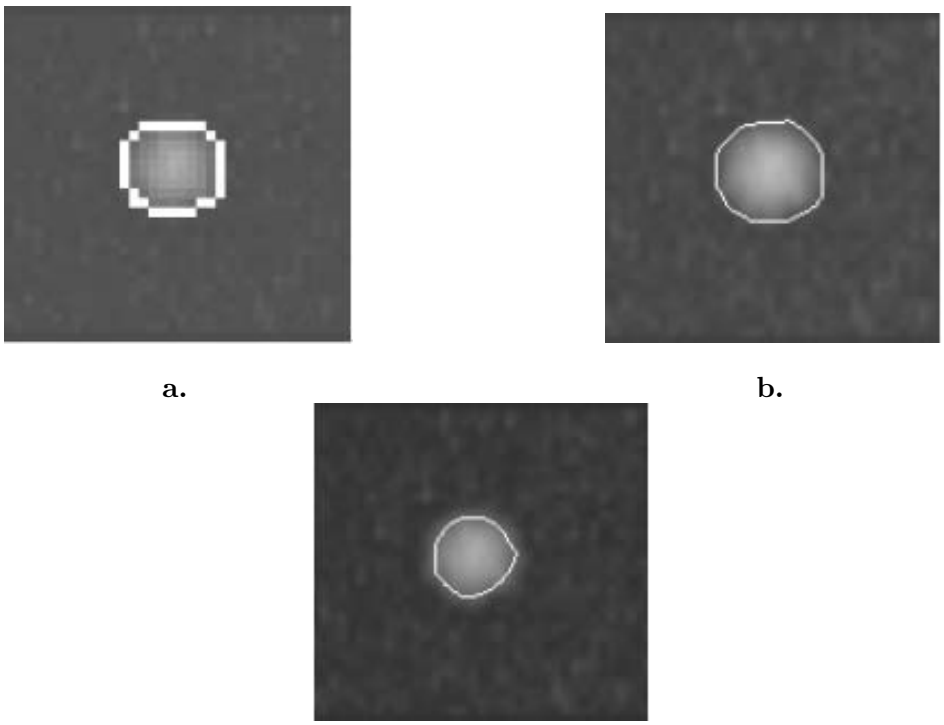

a. **b.**

c.

Figure 5.9: *Comparison of a cross-section of the surface at the same slice extracted by using (a) the voxel-based MAP-MRF approach (b) the sub-voxel level-set MAP-MRF approach, and (c) the sub-voxel level-set intensity gradient-based approach.*

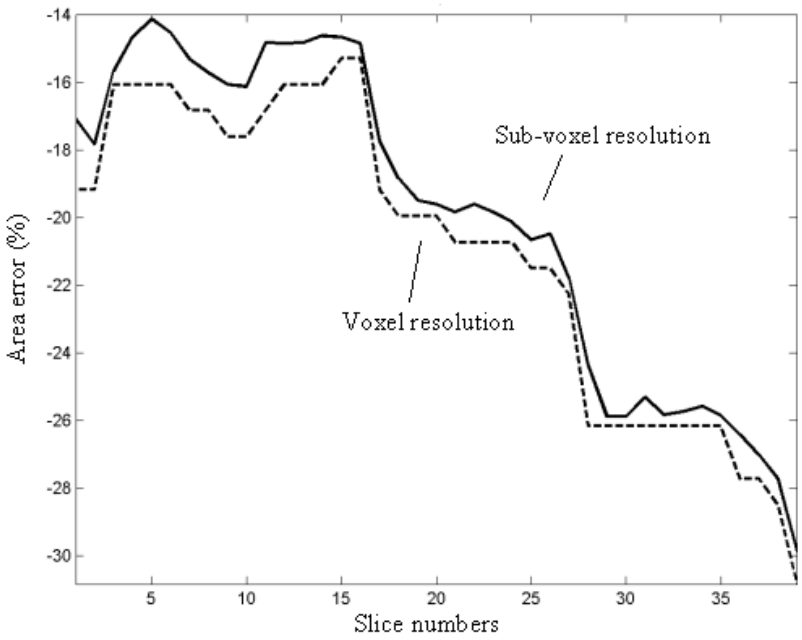

Figure 5.10: *Area errors of the method running in voxel resolution and the approach using the level set methods running in sub-voxel resolution. This figure shows that the errors of area estimation are* -21.24% *and* -20.27% *for the methods running in voxel and sub-voxel resolution respectively, and reveals that the accuracies of the sub-voxel based method and the voxel resolution method are comparable.*

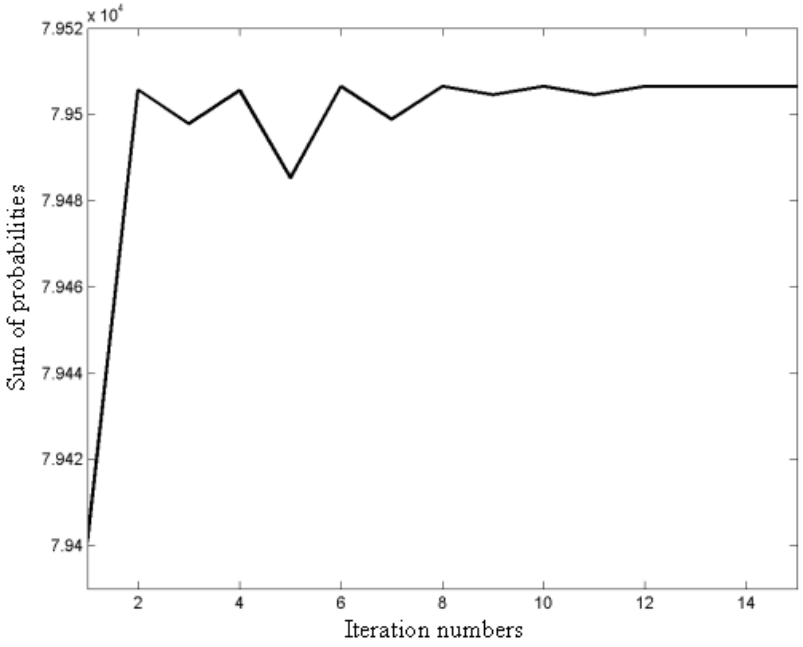

Figure 5.11: *A plot of the change of the total probabilities of vessel and background inside and outside the surface against the number of iterations of the level set method. Convergence is reached quickly after one iteration (if a* 0.1% *of change is used as the threshold to indicate convergence), but also a small change is observed after a few iterations because of the surface adjustments caused by the curvature-based smoothing term. As such, in practice, we set the number of iterations to 8. For this dataset, it takes 5 seconds for* $35 \times 133 \times 40$ *voxels on a 500MHz PC.*

5.5.2 Comparison between the level-set intensity gradient-based approach and sub-voxel based level-set MAP-MRF approach

Under the same experimental conditions as above, we compared a sub-voxel level-set intensity gradient-based approach and sub-voxel based level-set MAP-MRF method. Figure 5.12 shows the results of applying both methods on the straight tube flow phantom, where again we have used the area error as the measure of comparison. The sub-voxel based level-set MAP-MRF approach was found to give higher area estimate accuracy than the sub-voxel level-set intensity gradient-based approach by an average of 33.23%. Figures 5.9a and 5.9b show the contours found by using the sub-voxel level-set intensity gradient-based approach and sub-voxel based level-set MAP-MRF approach respectively on the same cross-section of the straight tube. This demonstrates that the sub-voxel based level-set MAP-MRF method gives more accurate vessel boundaries than the sub-voxel level-set intensity gradient-based approach.

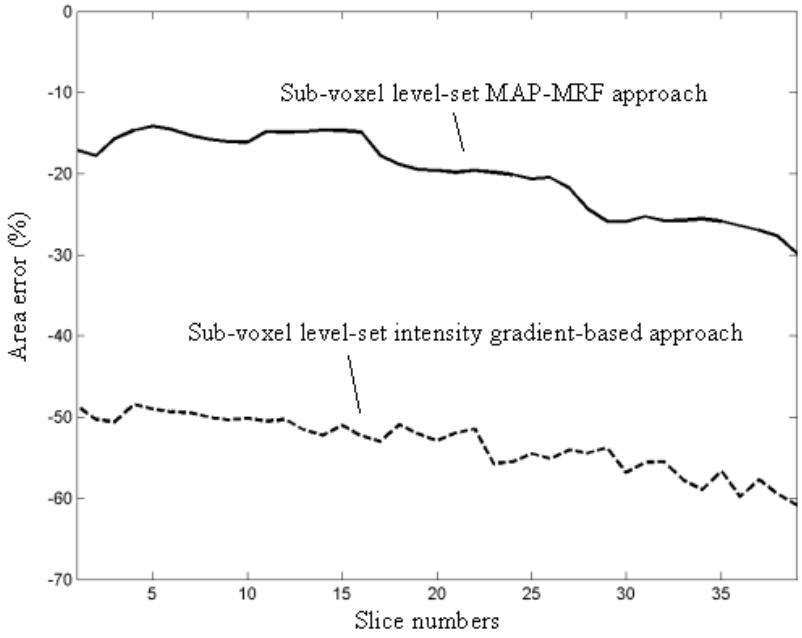

Figure 5.12: *In comparison, the errors of the area estimates (underestimation) are* -53.50% *and* -20.27% *for the sub-voxel level-set intensity gradient-based approach and sub-voxel MAP-MRF approach respectively.*

5.6 Summary

In this chapter, we have presented a surface extraction method based on the level set method that utilises the vascular and background probabilities obtained based on the MRF model. The attractiveness of the approach is that it uses intensity-based statistics of the vessel and background, and does not require intensity gradient information.

A geometrically accurate straight tube with fluid flowing at a constant rate inside was scanned. We used this scan to compare (a) the voxel and sub-voxel based level-set MAP-MRF methods, (b) sub-voxel level-set MAP-MRF method and the sub-voxel level-set intensity gradient-based approach. The experimental results show that the boundary extracted by the sub-voxel based method is clearly defined according to the probabilities of vessel and background, and smoother than the voxel-based method, and the accuracies of the sub-voxel based method and the voxel resolution method are comparable. The results also show that the sub-voxel based level-set MRA-MRF method is more accurate than the sub-voxel level-set intensity gradient-based approach by an average of 33.23% respectively. For the phantom dataset, the processing time for the sub-voxel level-set MRA-MRF method was 5 seconds (8 iterations) for $35 \times 133 \times 40$ voxels on a 500MHz PC.

The variational framework implemented by using the level set method is flexible, in which more information could be included easily in the same framework. In particular, the incorporation of information such as the true flow direction and local geometric structure (e.g. geometric tensor) may help surface propagation. Finally, the surface extracted by the level set method may be useful for 3D shape analysis and mesh generation for computational fluid dynamics (CFD) analysis [78].

Chapter 6

Clinical and phantom studies

6.1 Introduction

An integrated approach to reconstructing vessels in PC-MRA images has been presented in Chapters 2 to 5. This approach employs a Bayesian framework to combine the speed and flow coherence information in a PC-MRA dataset and uses a sub-voxel level set method to extract vascular surfaces. To assess the performance, in this chapter the approach has been applied to clinical and phantom datasets. In this chapter, we present the experimental results of the studies and discuss some properties of the approach.

The primary objective of the studies is to demonstrate the capabilities of the integrated approach in reconstructing normal vessels and aneurysms with relatively low signal-to-noise ratio (SNR) and low flow rate inside. These studies were conducted in collaboration with the Department of Neuroscience, King's College London, London and the Department of Radiology, Radcliffe Infirmary, Oxford, who helped with data acquisition.

This chapter is organised as follows. Firstly, in Section 6.2, the performance of the approach in reconstructing normal vessels is evaluated on two volunteer datasets. Then, in Section 6.3, an aneurysm phantom study is conducted so that the improvement in segmenting relatively low SNR and low flow regions, especially inside the aneurysm, can be compared with the known position and shape of the aneurysm. Finally, five clinical cases are presented in Section 6.4.

Regarding the implementation, the integrated approach was programmed in Visual C++ 6.0 with the use of MATLAB 6.0 Release 12 as an interface, and was run on a 500MHz PC in the Microsoft Windows NT environment with 512MB RAM.

6.2 Volunteer studies

In this section, the approach is tested on two volunteer PC-MRA scans, which were acquired on the Philips 1.5T ACS Gyroscan MR scanner at the Guy's Hospital, London.

Volunteer 1 was scanned in a sagittal direction. The scan details were as follows. The image size was $256 \times 256 \times 50$ voxels and dimensions were $0.86 \times 0.86 \times 1.0mm^3$. The other imaging parameters were: TE/TR = $6.2/14ms$, flip angle 20^o, 1 signal average, FOV: $20 \times 17.6cm^2$, VENCS: $450mms^{-1}$ and acquisition matrix: 256×160 pixels. The data processing window[1]: 170×142. Figures 6.1a and Figure 6.1b show the maximum intensity projection of the dataset and the corresponding view of the 3D reconstructed vasculature respectively. The individual processing times of the integrated approach were as follows. 1 second for the EM-based parameter estimation, 173 seconds for the computation of the 3D LPC maps, 37 seconds for the MAP-MRF algorithm (10 iterations, $\beta_1 = 2$ and $\beta_2 = 1$) and 236 seconds for the sub-voxel based level set method (8 iterations). Hence, the total time was 447 seconds (watch time). Figures 6.1c and 6.1d show one of the speed images and the contours generated by using the approach respectively. For the purpose of comparison, the contours are overlaid on the same speed image in the left hand figure.

The dataset of volunteer 2 was scanned in an axial direction. The scan details were as follows. The image size was $256 \times 256 \times 50$ voxels and dimensions were $0.94 \times 0.94 \times 1.2mm^3$. TE/TR = $11/24ms$, flip angle 20^o, 1 signal average, FOV: $12.8 \times 12.8cm^2$, VENCS: $200mms^{-1}$ and acquisition matrix: 256×160 pixels. The data processing window: 170×134 pixels. Figures 6.2a and 6.2b show the maximum intensity projection of the dataset and the corresponding view of the 3D reconstructed vasculature respectively. The individual processing times were as follows. 1 second for the EM-based parameter estimation, 165 seconds for the computation of the 3D LPC maps, 33 seconds for the MAP-MRF algorithm (10 iterations, $\beta_1 = 2$ and $\beta_2 = 1$) and 186 seconds for the sub-voxel based level set method (8 iterations). Hence, the total time was 385 seconds (watch time). Figures 6.2c and 6.2d show one of the speed images and the contours generated by using the approach respectively.

From Figures 6.1b and 6.2b, it is observed that all major arteries are clearly reconstructed

[1]Data processing window represents a region of interest (ROI), in which the integrated approach was applied. The ROI normally included the entire cross-section of the brain. The main purpose of applying the approach in an ROI was to shorten the computational time by not processing the non-interesting background of the images.

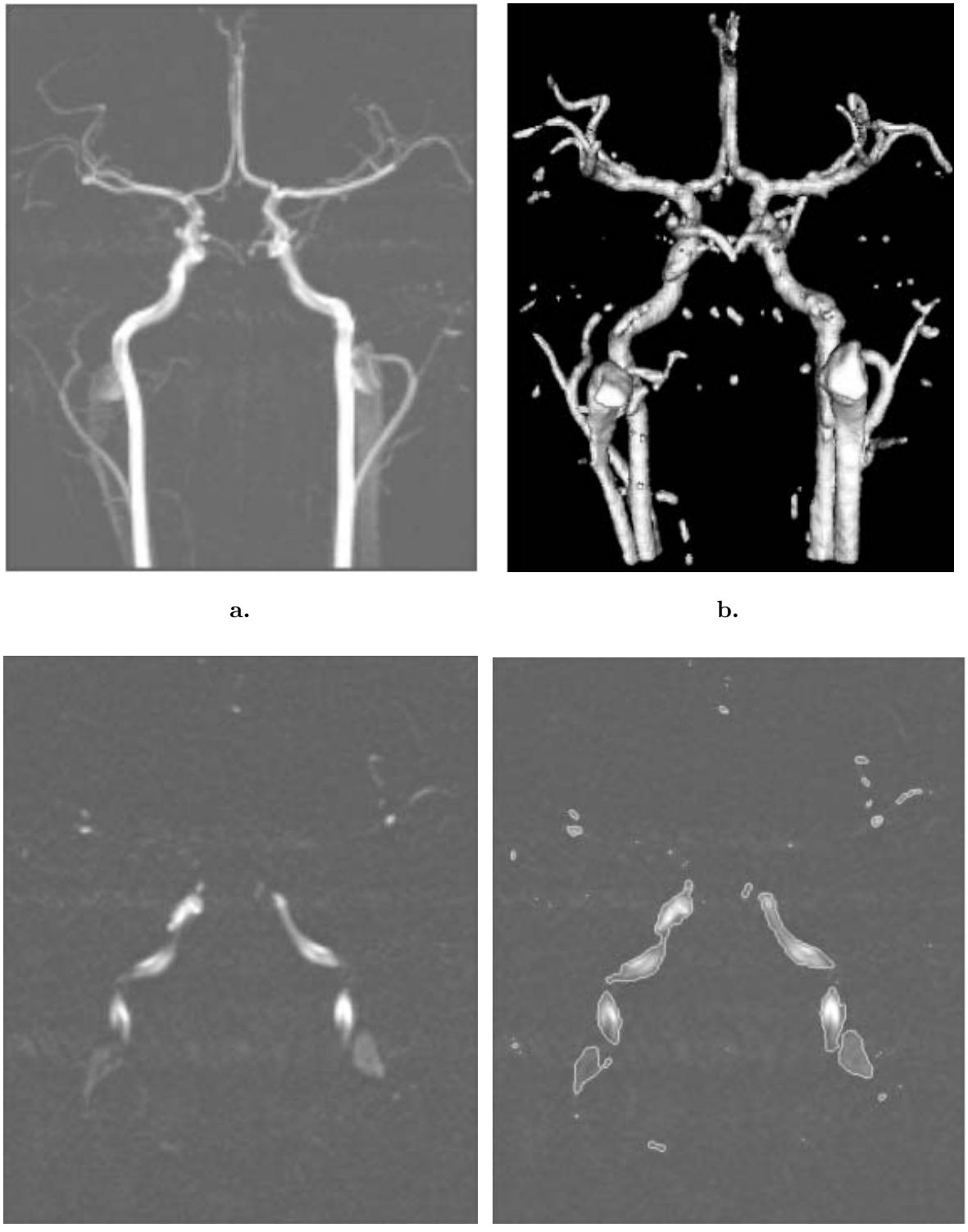

a. **b.**

c. **d.**

Figure 6.1: *Volunteer 1: (a) maximum intensity projection (MIP), (b) 3D reconstruction of the vasculature, (c) speed image and (d) contours generated by using the integrated approach.*

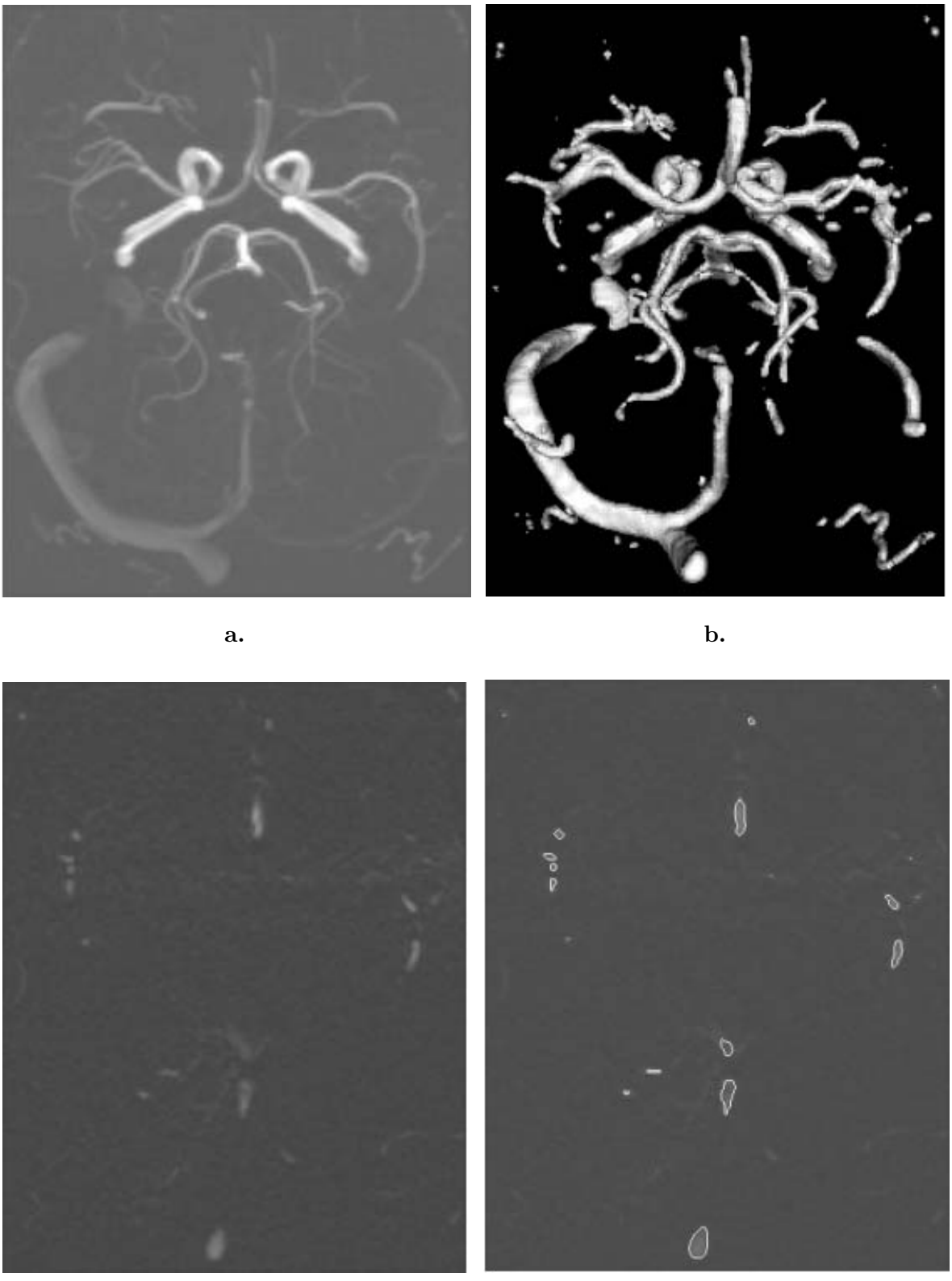

a. **b.**

c. **d.**

Figure 6.2: *Volunteer 2: (a) maximum intensity projection (MIP), (b) 3D reconstruction of the vasculature, (c) speed image and (d) contours generated by using the integrated approach.*

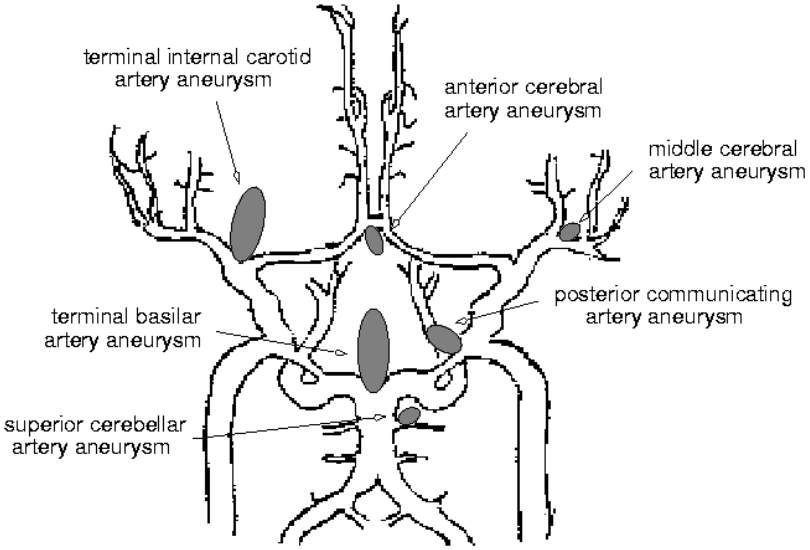

Figure 6.3: *Common sites of the aneurysms in the brain.*

by using the integrated approach, which are very important and useful to the diagnosis of intracranial aneurysms because common sites of the aneurysms are normally found on the major arteries [86, 14], as shown in Figure 6.3. It is also noted that small vessels with about one or two voxel width are not always reconstructed successfully because their SNR values are low and the 3D LPC measure may not give reliable information for vessels smaller than a $3 \times 3 \times 3$ window cube. This is an intrinsic limitation of the current approach. However, for the treatment of aneurysms, the current approach is adequate.

It is worth noting that the computational times for the EM-based parameter estimation and computation of 3D LPC measure are roughly the same for both scans because their implementation times are directly proportional to the number of voxels and the two scans have approximately the same number of processed voxels. On the other hand, the implementation time of the level set method for volunteer 1 is slightly longer than that of volunteer 2. This is because, in this application, the processing time of the level set method is dependent on the total surface area of the vessels. If the area is large, then more time is needed to initialise the signed distance level set surface in each iteration. Similar observations will be found in subsequent studies described later.

6.3 Phantom study

To illustrate the improvements obtained when the speed and flow coherence information are combined in the reconstruction process, the integrated approach was applied to an in-vitro silicon aneurysm phantom (Middle Cerebral Artery Bifurcation Aneurysm - MCA with one inlet (internal carotid artery) and three outlets (anterior cerebral, middle cerebral and posterior communicating arteries), as shown in Figure 6.4. This phantom was kindly provided by the Department of Neuroradiology, University Hospital of Geneva, Switzerland.

6.3.1 Setup and methods

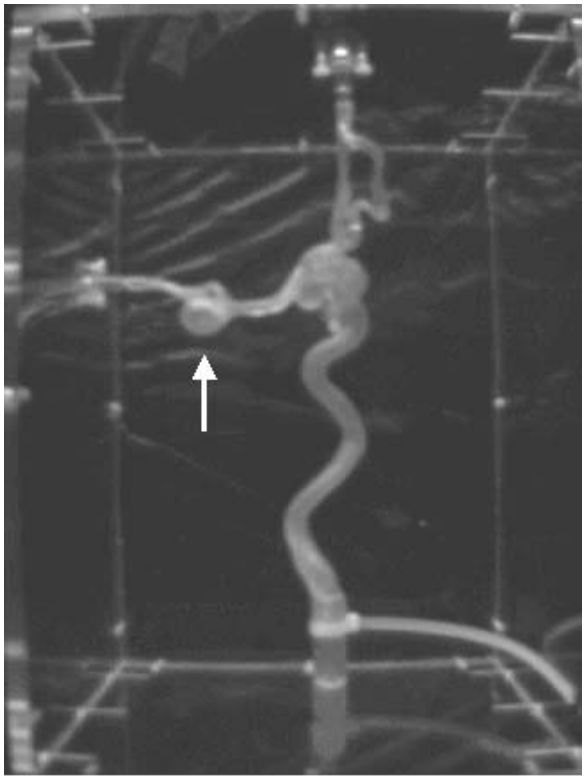

Figure 6.4: *Top view of the phantom and the perspex box. The arrow points to the middle cerebral aneurysm of the phantom.*

Pulsatile flow induces serious motion artifacts in the phantom. To alleviate this, it was firmly mounted inside a tailor-made, MR compatible perspex box[2] completely filled with gelatine, as shown in Figure 6.4. The working fluid was whole blood obtained from expired

[2]This perspex box was made in the Oxford University Engineering Department Workshop.

stocks of the blood bank of The Royal Free Hospital, London, and was pumped by a pulsatile blood pump (Harvard Apparatus Inc.). The flow rate was measured by an electromagnetic blood flow and velocity meter (MDL-1401). The mean flow rate was set to 300ml/min for this study [54].

The phantom was scanned using a PC-MRA protocol on a 1.5T GE MR scanner at the Department of Neuroscience, King's College London, London. The scan details were as follows. The data volume size was $256 \times 256 \times 23$ voxels with a voxel dimension of $0.8 \times 0.8 \times 1mm^3$. Axial scan, TE/TR = $6.8/18ms$, flip angle 20^o, 1 signal average, FOV: $22 \times 22cm^2$, VENCS: $400mms^{-1}$, acquisition matrix: 256×160 pixels. The data processing window: 91×105 pixels. The individual processing times were as follows. 1 second for the EM-based parameter estimation, 64 seconds for the computation of the 3D LPC maps, 12 seconds for the MAP-MRF algorithm (10 iterations) and 13 seconds for the sub-voxel based level set method (8 iterations). Hence, the total time was 90 seconds (watch time).

6.3.2 Results

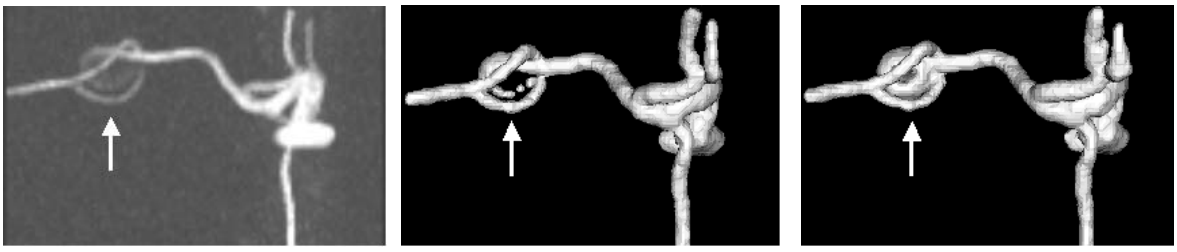

a. **b.** **c.**

Figure 6.5: *Aneurysm phantom: (a) maximum intensity projection, (b) 3D reconstruction using speed information alone and (c) 3D reconstruction using speed and flow coherence information. The arrow points to the aneurysm.*

To show the advantage of incorporating flow coherence information, the integrated approach using speed and flow coherence information was compared with an approach using the speed information alone.

Figures 6.5a and 6.6a show a maximum intensity projection of the phantom dataset and a closeup of the aneurysm respectively (the aneurysm is pointed to by an arrow in Figure 6.5a). In these two figures, the feeding (middle cerebral) vessel can be clearly seen because of its high intensity, whereas, the shape of the aneurysm is not obviously displayed because the

a. **b.** **c.**

Figure 6.6: *A closeup of the aneurysm phantom: (a) maximum intensity projection, (b) 3D reconstruction using speed information alone and (c) 3D reconstruction using speed and flow coherence information.*

flow rate inside is low and hence the intensity inside the aneurysm is low. 3D reconstructions of the vasculature and aneurysm based on the speed information alone are depicted in Figures 6.5b and 6.6b respectively. Observe that although the vessels are clearly reconstructed, the aneurysm is not well reconstructed due to its low intensity.

Figures 6.5c and 6.6c show the 3D reconstruction of vasculature and a closeup of the aneurysm based on the approach using speed and flow coherence information approach. The figures reveal that the shapes of the vessels and aneurysm are well delineated.

Figures 6.7a and 6.8a show two speed images of the phantom dataset, in which the cross-sections of the MCA aneurysm is pointed to by the arrows. As illustrated in Figures 6.7b and 6.8b, the contours generated by using speed information alone are drawn. Although the contours correctly delineate the large vessel (internal carotid) with high intensity in the right, the aneurysm is not well delineated.

Figures 6.7c and 6.8c show the local phase coherence (LPC) maps, in which the intensity value is directly proportional to the degree of flow coherence. Note that the regions inside the aneurysm are enhanced. As discussed in Chapter 4, flow coherence can provide additional and complementary information to flow magnitude in the segmentation process. As compared with Figures 6.7b and 6.8b, a significant improvement in delineating and detecting the aneurysms is achieved when the speed and flow coherence information are combined (Figures 6.7d and 6.8d). Note that, in this case, we set $\beta_1 = 3$ and $\beta_2 = 1$ in the MAP-MRF model to enhance the interactions between coherent vessel voxels. This is because the initial segmentation based on speed information alone is not very good (see Figures 6.7b and 6.8b),

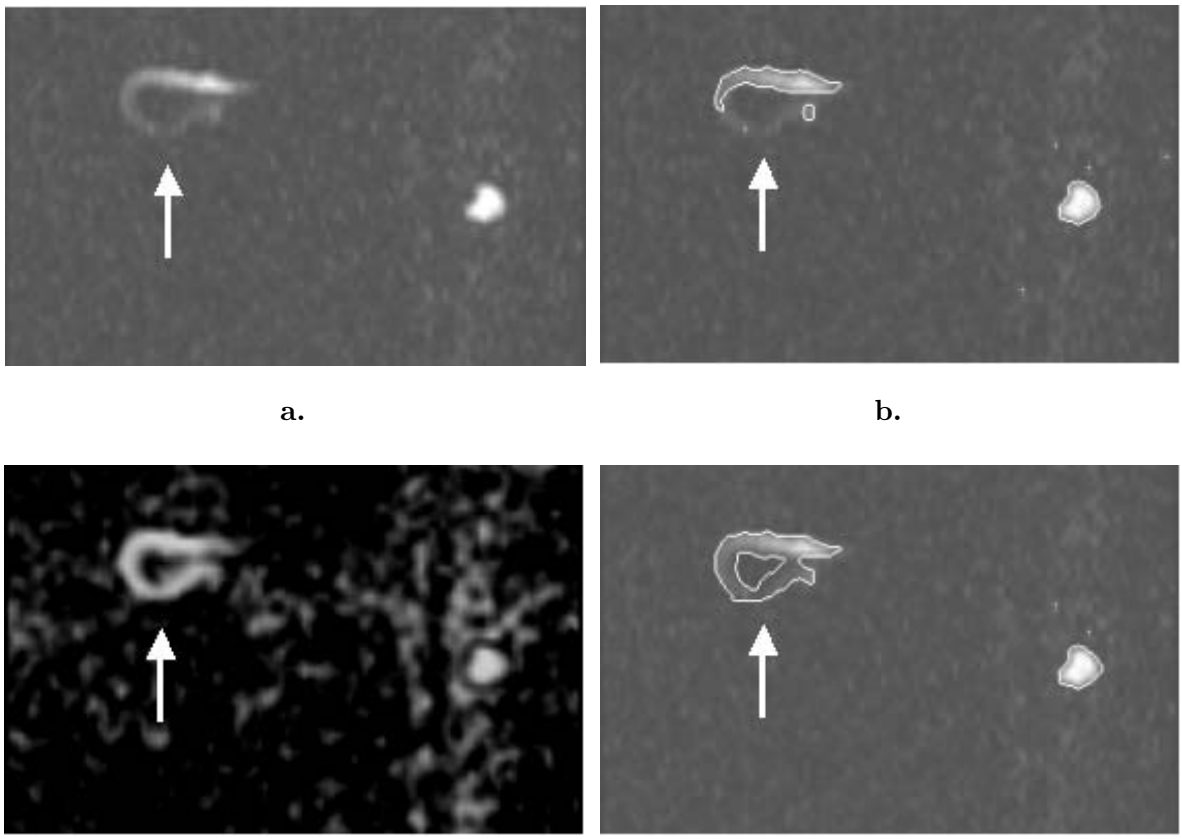

a. **b.**

c. **d.**

Figure 6.7: *Aneurysm phantom: (a) speed image, (b) contours generated by using the speed information alone, (c) LPC map and (d) contours generated by using the speed and flow coherence information.*

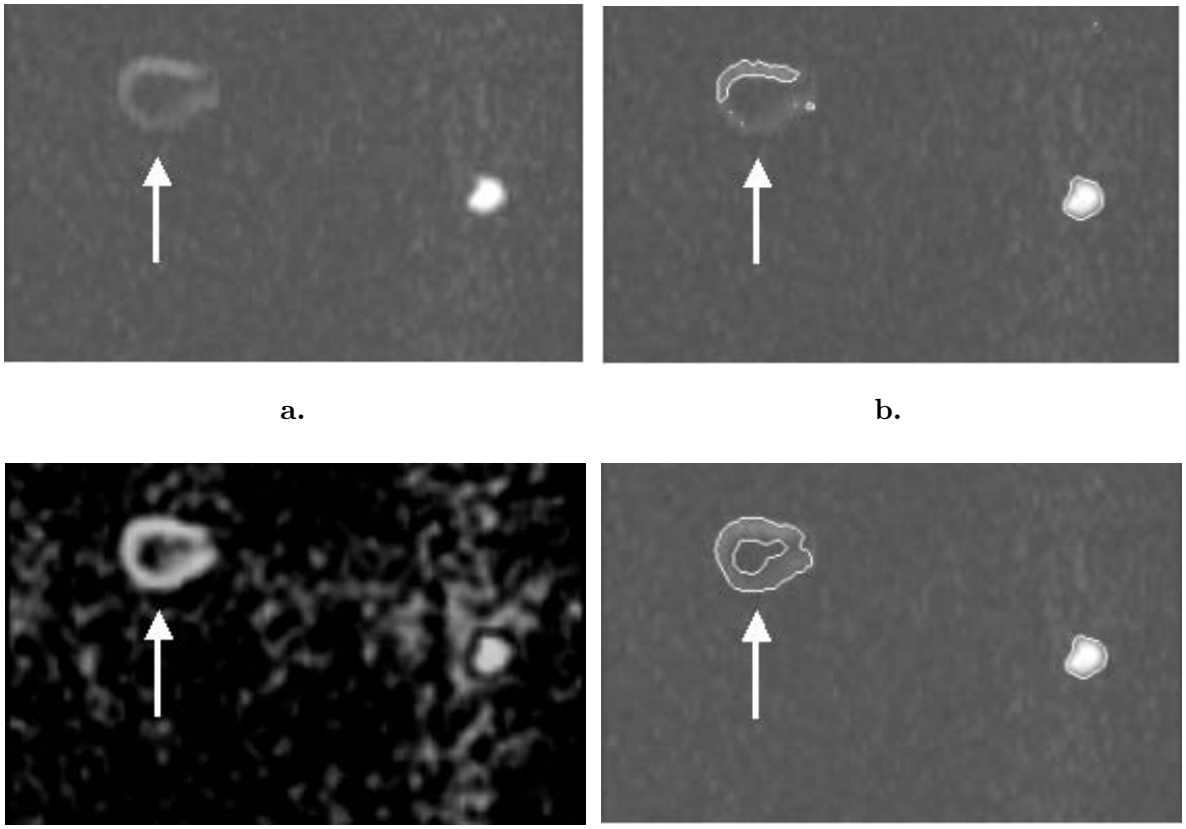

a. **b.**

c. **d.**

Figure 6.8: *Aneurysm phantom: (a) speed image, (b) contours generated by using the speed information alone, (c) LPC map and (d) contours generated by using the speed and flow coherence information.*

and the aneurysm is large[3] in size ($15mm$ diameter).

As shown in Figures 6.7d and 6.8d, the contours in the middle of the aneurysm enclose regions with very low flow rate as well as the singular point of the velocity field, where the flow rate is almost zero. These inner contours could be easily removed. However, they can also be a useful feature because they indicate to a neuroradiologist the regions of very low flow and positions of stagnant flow inside the aneurysm.

6.4 Clinical cases

This section presents results obtained by using the integrated approach based on speed and flow coherence information on clinical data. The focus of this section is to assess the detectability of the method on five datasets. The approach was applied to five clinical cases: two patient datasets were obtained from the Department of Neuroscience, King's College London, London (Section 6.4.1), one patient dataset from the Department of Radiological Sciences, Guy's Hospital, London (Section 6.4.2), and two patient datasets were obtained from the Department of Radiology, Radcliffe Infirmary, Oxford (Section 6.4.3). These were chosen to show that the approach works on a variety of different commercial machinery and hence different SNR conditions.

6.4.1 Patients 1 and 2

Patients 1 and 2 were scanned on the GE 1.5T Signa MR scanner at the Department of Neuroscience, King's College London, London. Patient 1 presented with a middle cerebral artery aneurysm. Figures 6.9a and 6.9b show the maximum intensity projection and the corresponding view of the 3D reconstructed vasculature respectively, in which the aneurysm is clearly shown and pointed to by the arrows in both images. The scan details were as follows. The image size was $256 \times 256 \times 28$ voxels and dimensions were $0.78 \times 0.78 \times 1.1mm^3$. Axial scan, TE/TR = $8/22ms$, flip angle 18^o, 1 signal average, FOV: $20 \times 15cm^2$, VENCS: $300mms^{-1}$ and acquisition matrix: 256×160 pixels. The data processing window: 248×184 pixels. The individual processing times were as follows. 1 second for the EM-based parameter estimation, 182 seconds for the computation of the 3D LPC maps, 35 seconds for the MAP-

[3]According to [86], a small aneurysm has a diameter less than $12mm$, a large aneurysm has a diameter ranging between $12mm$ and $25mm$, and a giant aneurysm has a diameter greater than $25mm$.

a. *Patient 1: MIP.*

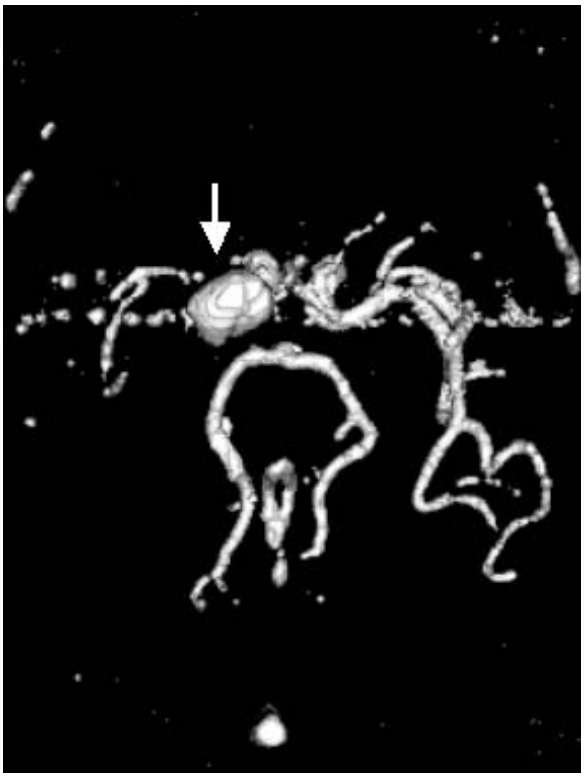

b. *Patient 1: 3D reconstructed vasculature.*

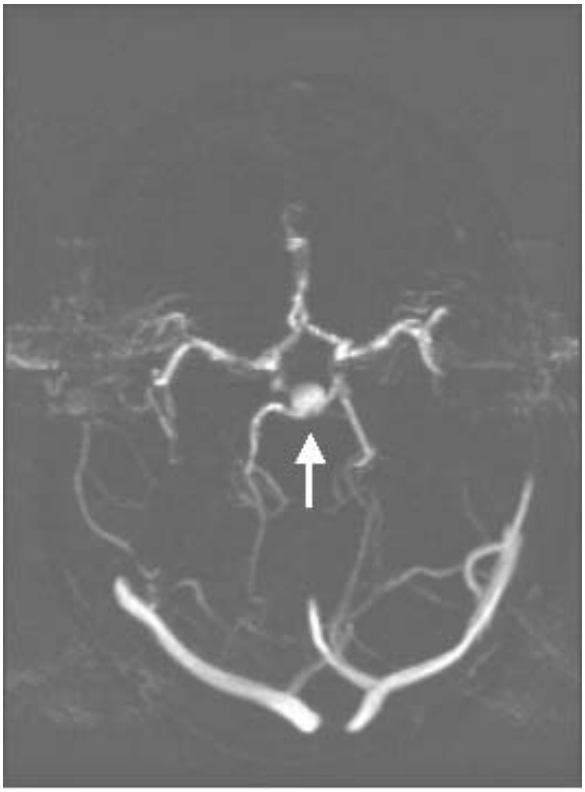

c. *Patient 2: MIP.*

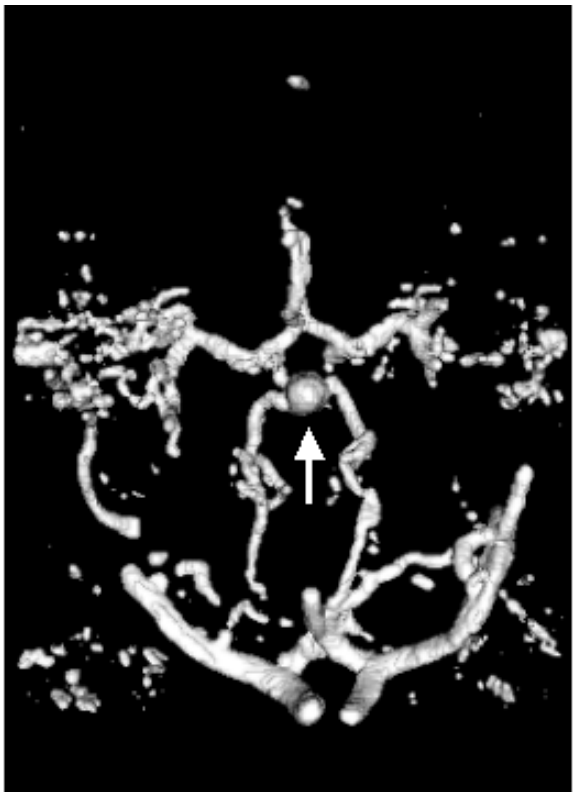

d. *Patient 2: 3D reconstructed vasculature.*

Figure 6.9: *The maximum intensity projections (MIP) and 3D reconstructed vasculature of patients 1 and 2.*

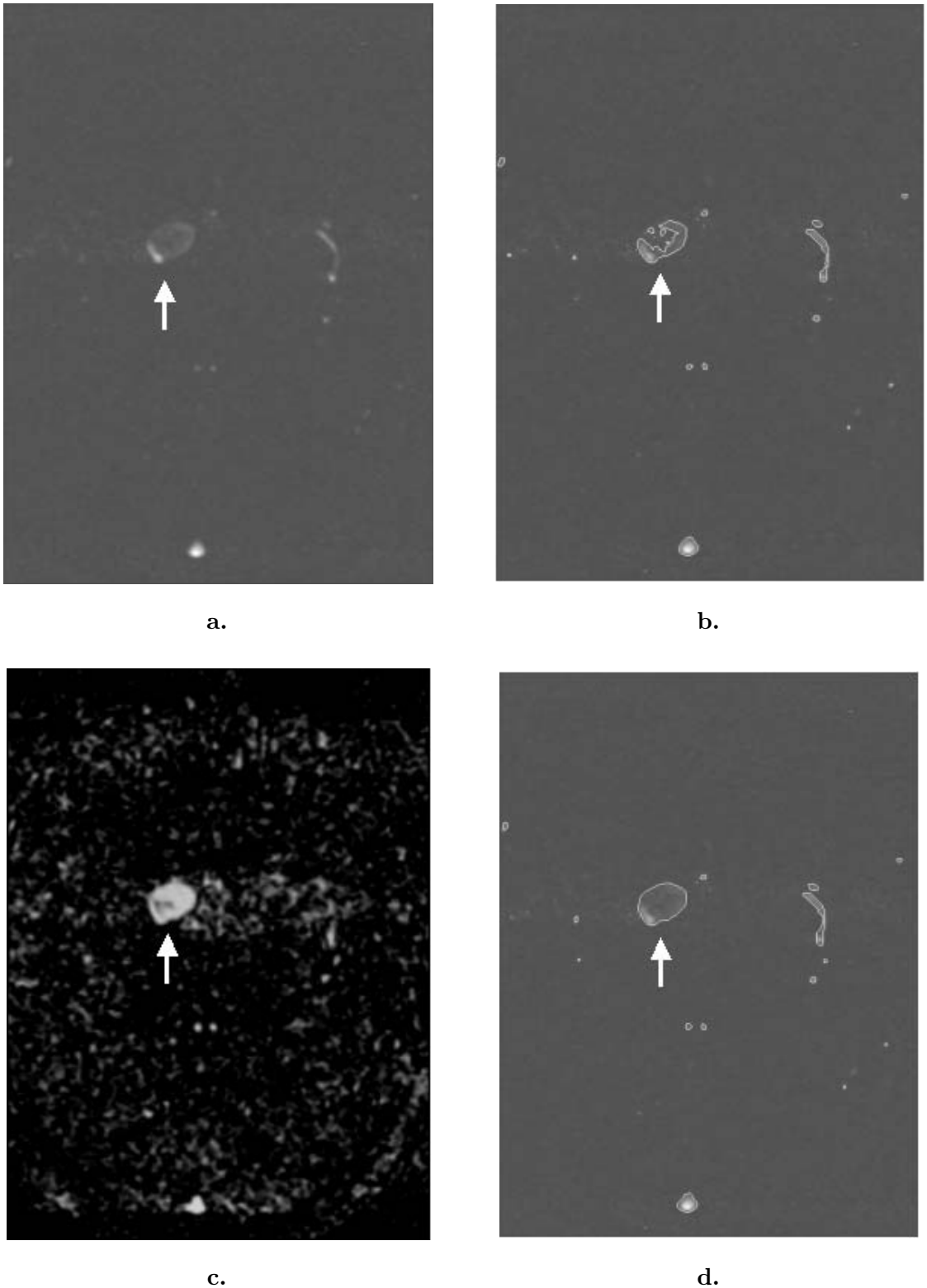

a. **b.**

c. **d.**

Figure 6.10: *Patient 1: (a) speed image, (b) contours generated by using the speed information alone, (c) LPC map and (d) contours generated by using the speed and flow coherence information.*

MRF algorithm (10 iterations, $\beta_1 = 2$ and $\beta_2 = 1$) and 52 seconds for the sub-voxel based level set method (8 iterations). Hence, the total time was 360 seconds (watch time).

Patient 2 presented with a basilar artery aneurysm. The maximum intensity projection of the dataset and the corresponding view of the 3D reconstructed vasculature are shown in Figures 6.9c and 6.9d respectively. The aneurysm can be clearly observed and is pointed to by the arrows in both images. The scan details were as follows. The image size was $256 \times 256 \times 28$ voxels and dimensions were $0.86 \times 0.86 \times 0.9mm^3$. Axial scan, TE/TR = $7.3/20ms$, flip angle 18^o, 1 signal average, FOV: $22 \times 16cm^2$, VENCS: $300mms^{-1}$ and acquisition matrix: 256×160 pixels. The data processing window: 251×185 pixels. The individual processing times were as follows. 1 second for the EM-based parameter estimation, 203 seconds for the computation of the 3D LPC maps, 32 seconds for the MAP-MRF algorithm (10 iterations, $\beta_1 = 2$ and $\beta_2 = 1$) and 220 seconds for the sub-voxel based level set method (8 iterations). Hence, the total time was 456 seconds (watch time).

As shown in Figure 6.10, an improvement in segmentation is obtained when the speed and flow coherence information are used so that the aneurysm is well represented. Figure 6.10a shows one of the PC-MRA speed images in patient 1 dataset. Figures 6.10d and 6.10b show the contours generated by using the integrated approach and an approach using the speed information alone respectively, whereas, Figure 6.10c illustrates the corresponding LPC map.

It is noted that the ghosting artifacts are apparent in the speed images, especially in Figure 6.9c (along the middle horizontal direction in the image), and have sometimes been reconstructed as parts of the vasculature, as shown in Figure 6.9d. This artifact is mainly caused by the pulsatility of the blood vessels, and could affect the quality of reconstructing if the artifact occurs in the region of interest, e.g. aneurysms or main arteries. Measures to reduce ghosting artifact by altering the k-space sampling order [56], or by auto-focus methods [55] have been proposed to overcome this but were not applied to the data presented in this thesis. For the purpose of visualisation and diagnosis, to minimise this problem, a region of interest enclosing the detected aneurysm and avoiding the ghosting artifacts can be drawn manually after the reconstruction.

6.4.2 Patient 3

Patient 3 presented a middle cerebral artery aneurysm and was scanned on the Philips 1.5T ACS Gyroscan MR scanner at the Department of Radiological Sciences, Guy's Hospital,

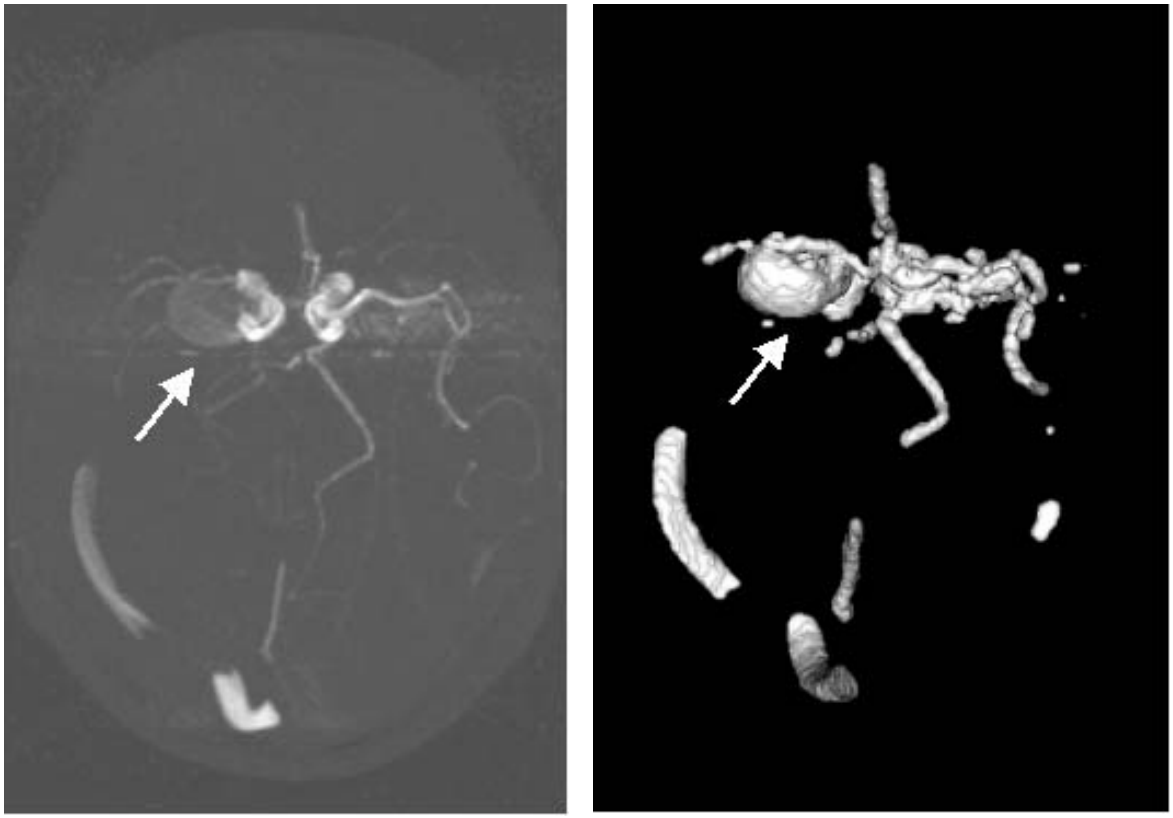

a. **b.**

Figure 6.11: *Patient 3: (a) maximum intensity projection and (b) 3D reconstruction of the vasculature.*

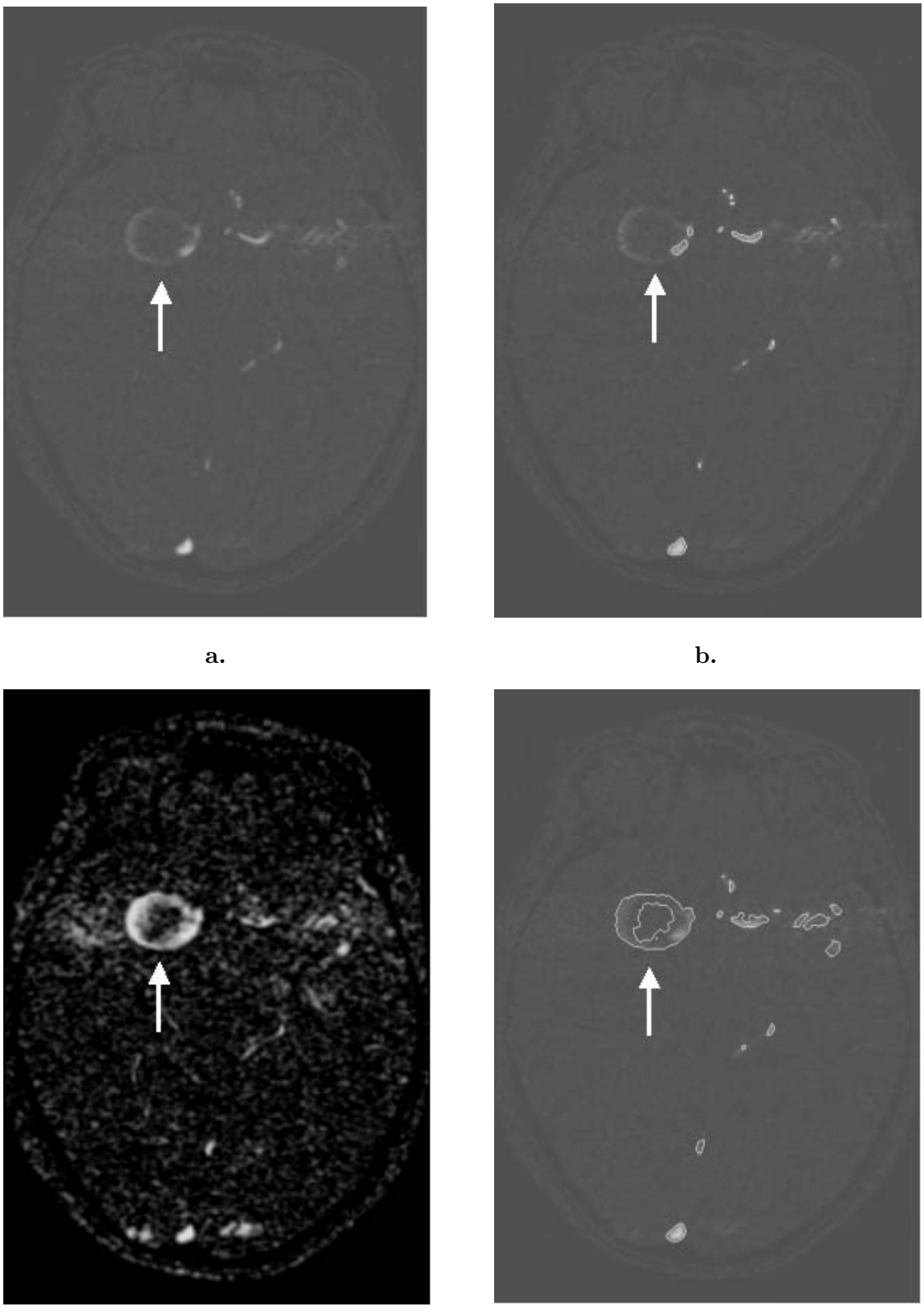

a. **b.**

c. **d.**

Figure 6.12: *Patient 3: (a) speed image, (b) contours generated by using the speed information alone, (c) LPC map and (d) contours generated by using the speed and flow coherence information.*

London. The scan details were as follows. The image size was $256 \times 256 \times 36$ voxels and dimensions were $0.86 \times 0.86 \times 1mm^3$. Axial scan, TE/TR = $8.1/16ms$, flip angle 20^o, 1 signal average, FOV: $22 \times 22cm^2$, VENCS: $200mms^{-1}$ and acquisition matrix: 256×192 pixels. The data processing window: 250×171 pixels. The individual processing times were as follows. 1 second for the EM-based parameter estimation, 248 seconds for the computation of the 3D LPC maps, 44 seconds for the MAP-MRF algorithm (10 iterations) and 54 seconds for the sub-voxel based level set method (8 iterations). Hence, the total time was 347 seconds (watch time). Similarly to the phantom dataset, we set $\beta_1 = 3$ and $\beta_2 = 1$ in the MAP-MRF model because, as shown in Figure 6.12b, the initial segmentation is not very good and the size of the aneurysm is giant ($28.4mm$ measured from the MRA speed image).

A maximum intensity projection of the dataset was generated and shown in Figure 6.11a. Due to the large size and low flow rate of the aneurysm, its shape cannot be obviously seen (pointed to by an arrow). Note that the ghosting artifact is observed as a horizontal band in the middle right of the image. Figure 6.11b shows the corresponding view of the 3D reconstructed vasculature and also the segmented ghost. In this case, the aneurysm is detected and depicted clearly in Figure 6.11b and pointed to by an arrow. Figure 6.12 shows an example of the individual slices. Note that although the cross-section of the aneurysm does not exhibit high intensity for the detection (Figure 6.12a), the regions inside the aneurysm are greatly enhanced (Figure 6.12c) so the aneurysmal surface can be extracted (Figure 6.12d).

6.4.3 Patients 4 and 5

Patients 4 and 5 were scanned on the 1.5T Magnetom Vision Siemens MR scanner at the Department of Radiology, Radcliffe Infirmary, Oxford. Patient 4 presented a regrowth of the middle cerebral artery aneurysm, which has been coiled before. The scan details were as follows. The image size was $256 \times 256 \times 38$ voxels and dimensions were $0.78 \times 0.78 \times 1.5mm^3$. Axial scan, TE/TR = $9/81ms$, flip angle 10^o, 1 signal average, FOV: $19.9 \times 19.9cm^2$, VENCS: $400mms^{-1}$ and acquisition matrix: 256×256 pixels. The data processing window: 225×156 pixels. The individual processing times were as follows. 1 second for the EM-based parameter estimation, 199 seconds for the computation of the 3D LPC maps, 15 seconds for the MAP-MRF algorithm (10 iterations, $\beta_1 = 2$ and $\beta_2 = 1$) and 107 seconds for the sub-voxel based level set method (8 iterations). Hence, the total time was 322 seconds (watch time).

A maximum intensity projection of the dataset is shown in Figure 6.13a, in which the

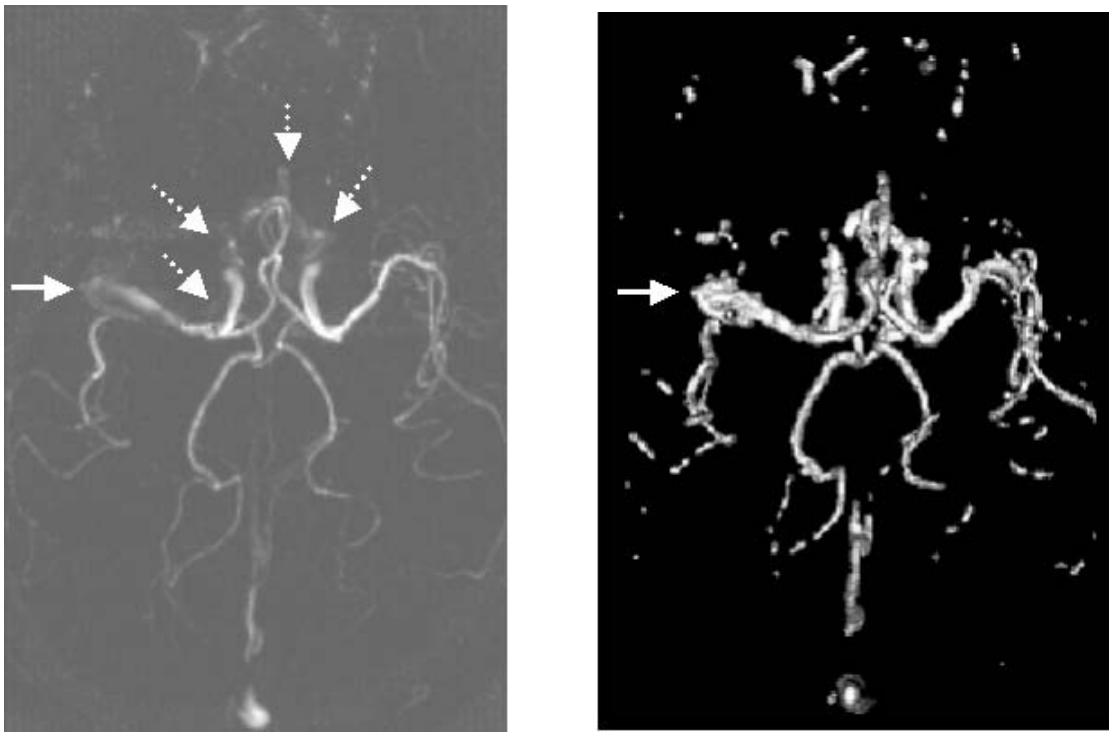

a. *Patient 4: MIP.* **b.** *Patient 4: 3D reconstructed vasculature.*

Figure 6.13: *(a) A maximum intensity projection of the dataset is shown, in which the regrowth of the aneurysm is pointed to by an solid arrow and the vertical ghosting artifacts are pointed to by the dotted arrows. (b) The regrowth of the aneurysm was successfully detected by the segmentation algorithm and its geometrical shape is clearly shown in the 3D reconstructed vasculature. Note that parts of the ghosts are reconstructed and are attached to the top of the internal carotid arteries. However, the detection of aneurysm is not affected in this case.*

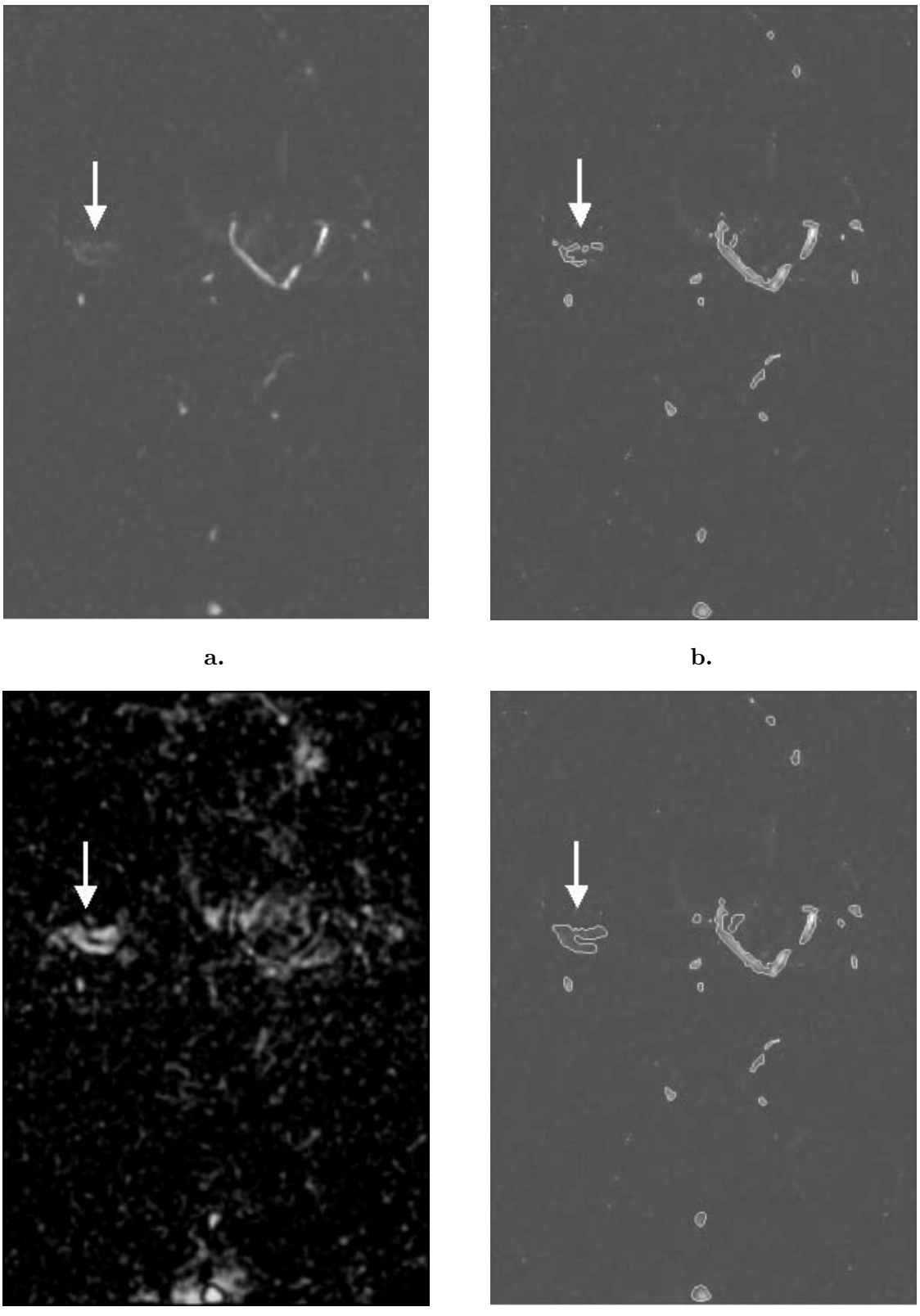

a. **b.**

c. **d.**

Figure 6.14: *Patient 4: (a) speed image, (b) contours generated by using the speed information alone, (c) LPC map and (d) contours generated by using the speed and flow coherence information.*

regrowth of the aneurysm is pointed to by an solid arrow and the vertical ghosting artifacts are pointed to by the dotted arrows. The regrowth of the aneurysm was successfully detected by the segmentation algorithm and its geometrical shape is clearly shown in the 3D reconstructed vasculature (Figure 6.13b). Note that parts of the ghosts are reconstructed and are attached to the top of the internal carotid arteries. However, the detection of aneurysm is not affected in this case.

Similar to the previous cases, as shown in Figure 6.14, the LPC map (Figure 6.14c) offers a useful explanation for the detection of low flow vascular regions and helps the reconstruction of aneurysm (Figure 6.14d) as compared to the reconstruction using speed information alone (Figure 6.14b). The aneurysm is pointed to by the arrows in the figures.

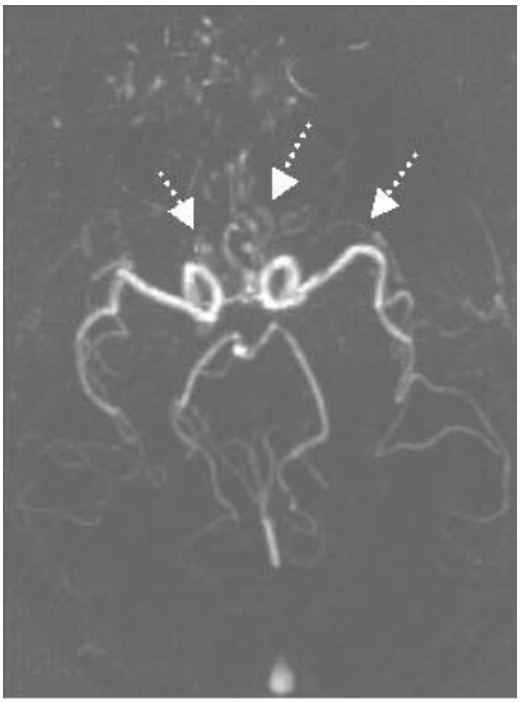

a. *Patient 5: MIP.*

b. *Patient 5: 3D reconstructed vasculature.*

Figure 6.15: *Patient 5: (a) shows the maximum intensity projection (MIP) of the dataset and (b) shows the corresponding view of the 3D reconstructed vasculature. The aneurysm was small and not readily visible in the MIP (top view of the dataset). The dotted arrows in (a) point to the ghosting artifacts*

Finally, patient 5 presented with an internal carotid artery aneurysm. The scan details were as follows. The image size was $256 \times 256 \times 33$ voxels and dimensions were $0.86 \times 0.86 \times 1.44 mm^3$. Axial scan, TE/TR = $8/81 ms$, flip angle 10^o, 1 signal average, FOV:

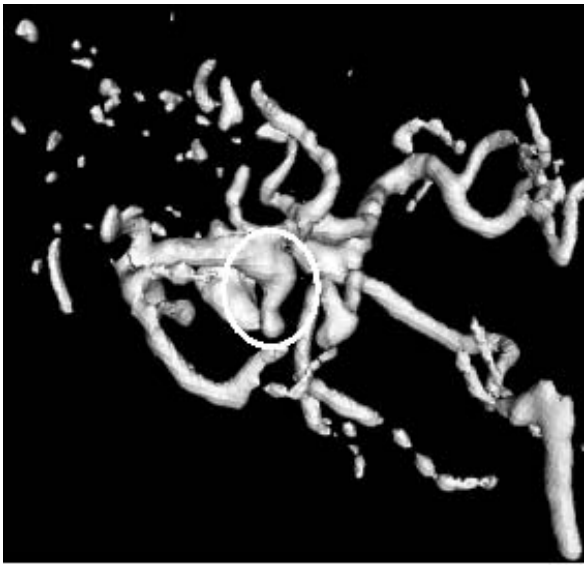

Figure 6.16: *Patient 5: a closeup of the aneurysm. The aneurysm is clearly detected and its relationship with the vessels at the vicinity of the aneurysm is clearly shown.*

$21.9 \times 21.9cm^2$, VENCS: $400mms^{-1}$ and acquisition matrix: 256×256 pixels. The data processing window: 211×157 pixels. The individual processing times were as follows. 1 second for the EM-based parameter estimation, 160 seconds for the computation of the 3D LPC maps, 12 seconds for the MAP-MRF algorithm (10 iterations, $\beta_1 = 2$ and $\beta_2 = 1$) and 118 seconds for the sub-voxel based level set method (8 iterations). Hence, the total time was 291 seconds (watch time).

Figures 6.15a and 6.15b show the maximum intensity projection (MIP) of the dataset and the corresponding view of the 3D reconstructed vasculature respectively. The aneurysm was small and not readily visible in the MIP (top view of the dataset). The dotted arrows in Figure 6.15a point to the ghosting artifacts, which are close to the true vasculature in this case. However, as illustrated in a closeup of the aneurysm (Figure 6.16), the aneurysm is clearly detected and its relationship with the vessels at the vicinity of the aneurysm is clearly shown.

6.5 Summary

In this chapter, we have demonstrated the applicability of the integrated approach to vessel and aneurysm segmentation based on both speed and flow coherence information. The ap-

proach was applied to two volunteers, one aneurysm phantom and five patient datasets. In the case of the aneurysm and patient datasets, it was found that the use of flow coherence information improves the reconstruction quality and detection of the aneurysm, especially when the size of aneurysm is large. The total computational time, on average for all volunteer and patient cases, is about 5-6 mins, which is acceptable for pre-operative planning or post-operative evaluation procedures.

Ghosting artifacts (present in all standard PC-MRA protocols) did not significantly affect the detection of aneurysms in the cases considered. However, their effect should be taken into account in general. On-going work is looking into how to reduce the ghosting artifacts possibly by using the altered k-space sampling order [56], or by auto-focus methods [55].

Chapter 7

Conclusions and future work

7.1 Conclusions

In this thesis, we have presented a new approach to reconstructing vessels and aneurysms in phase contrast magnetic resonance angiograms (PC-MRA). The main focus has been to show how speed and flow coherence information extracted from a PC-MRA dataset can be combined to detect and reconstruct normal vessels and aneurysms with relatively low signal-to-noise ratio (SNR) and low flow rate.

Our contributions have been both in the area of understanding PC-MRA imaging physics and also in vascular (vessel and aneurysm) segmentation. We began in Chapter 2 by analysing the statistical characteristics of vascular and background signals in PC-MRA speed images based on knowledge of image formation and a laminar blood flow assumption. The analysis led to the development of the Maxwell-Gaussian mixture model for modelling the background signals, and utilisation of a uniform distribution to model the vascular signals. We proposed to estimate the parameters in the Maxwell-Gaussian-uniform (MGU) mixture model by the Expectation-Maximisation (EM) algorithm and derived the update equations for the MGU model. Experimental results using a MAP global thresholding method revealed that the MGU model worked satisfactorily in classifying the background and vessel voxels. However, for relatively low SNR and low flow rate vessel regions, e.g. inside aneurysm, we found that it was hard to distinguish vessel voxels from the background voxels because of their low intensity values.

To deal with this problem, in Chapter 3 we proposed to incorporate a new flow coherence measure, namely *local phase coherence* (LPC) measure, into the segmentation process as an

additional local constraint. Experiments on synthetic data suggested that the LPC measure was better than prior coherence measures because it incorporates the spatial correlations between neighbouring flow vectors in the coherence measure.

A Bayesian framework was employed in Chapter 4 to integrate PC-MRA speed and flow coherence information. The (Maximum *A-Posteriori*) MAP-based framework encodes knowledge of the PC-MRA speed image formation process and physical characteristics of blood flow through the likelihood functions of the vessel and background, i.e. the MGU model; and enhances the local relationships between the voxels through the prior probability, i.e. the Markov Random Field (MRF) and Gibbs distributions, based on the LPC measure and current states of the voxels. Experimental results on synthetic and clinical data showed that the MAP-MRF method outperforms segmentation using either speed or flow coherence information alone, and gives a better segmentation quality at both low and high SNR values.

In Chapter 5, we link together all the key ideas developed in Chapters 2-4. In this Chapter, we present a sub-voxel based level-set method to extract the vascular surface in the posterior probability maps estimated by the Bayesian framework presented in Chapter 4. The resulting level-set MAP-MRF method is evaluated on a geometric accurate straight tube. The experimental results show that the surface boundary extracted by the sub-voxel based method is clearly defined according to the probabilities of vessel and background, and smoother than the voxel-based equivalent method; and the accuracies of the sub-voxel based method and the voxel resolution method are comparable. We also show that the sub-voxel level-set MAP-MRF method is more accurate than a sub-voxel let-set intensity gradient-based approach by an average 33.23%.

Finally, in Chapter 6 the performance of the sub-voxel level-set MAP-MRF method was evaluated on an aneurysm phantom and 7 clinical datasets. Testing on the datasets showed that the vasculature and aneurysms were reconstructed and detected by the new approach. In particular, the results also revealed that the new approach performs better than the approach using speed information alone in detecting aneurysms.

7.2 Future work

This section outlines some directions of future work.

First of all, as discussed in Chapter 6, image quality of PC-MRA images can be improved if ghosting artifacts can be reduced by using the altered k-space sampling order [56], or by auto-focus methods [55]. In addition, we have measured the accuracies of the proposed method on a geometrically accurate flow phantom (straight tube) data using PC-MRA. With the advance in 3D X-ray angiographic techniques, vasculature of a patient can be reconstructed in 3D by using a rotating C-arm and sequence of DSA images during the treatments. The X-ray based 3D angiography have higher spatial resolution than PC-MRA, and therefore could provide an alternative and accurate way of evaluating performance of the new methods in-vivo.

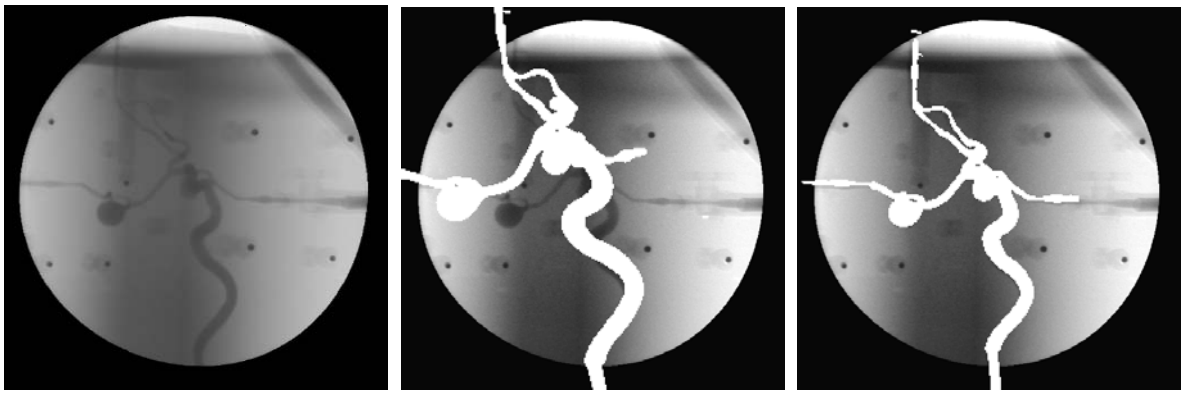

a. **b.** **c.**

Figure 7.1: *(a) Digital subtraction angiogram (DSA), (b) initial registration and (c) final registration, which shows that the DSA image and projection of the 3D vasculature are well matched.*

As mentioned in Chapter 1, during an endovascular treatment of an aneurysm, a neuro-radiologist guides a catheter through blood vessels, while viewing its progress using real-time 2D X-ray images, as shown in Figure 7.1a. Registration between the 2D X-ray images and 3D vasculature (2D-3D registration) can provide useful information about the current position of the catheter and help understanding of the spatial relationships between vessels and the aneurysm during the treatment. We have performed preliminary experiments using the 3D segmentation and reconstruction methods developed in this thesis to provide 3D model used in 2D-3D registration [59], Figure 7.1. Figure 7.1b shows a projection of 3D reconstructed

vessels and aneurysm on a DSA image before registration, and the result after registration is shown in Figure 7.1c.

Finally, the methods developed in this thesis can not only be used for detecting aneurysms, but could also be used in other clinical contexts such as the analysis of endovascular treatment results of brain arteriovenous malformations (AVM) [63]. Moreover, the methods could also be used in the field of computational fluid analysis (CFD) for simulating the changes of flow pattern inside the vasculature so that the effect of treatment could be predicted and assessed.

Appendix A

Derivation of the Maxwell-Gaussian mixture model

This appendix describes a derivation of the Maxwell-Gaussian mixture model for the background signal in PC-MRA speed images. Recall from Section 2.3.2, that a speed image is obtained by applying a modulus operation to the three corresponding magnitude-weighted phase shifts in the phase images (orthogonal directional components) voxel by voxel. Assume that, in background regions, the three magnitude-weighted phase values $\bar{M}\Delta\phi_x$, $\bar{M}\Delta\phi_y$ and $\bar{M}\Delta\phi_z$ are represented by statistically independent random variables, p_x, p_y and p_z, respectively and each PDF of the magnitude-weighted phase values consists of a zero-mean Gaussian (located at the centre) and two non-zero mean Gaussian distributions (located at each side) (Section 2.3.4). As such, the PDF f_{p_k} of each magnitude-weighted phase value is approximated by a triple Gaussian model, which is given by

$$f_{p_k}(p_k) = \frac{w_l}{\sqrt{2\pi}\sigma_l} \cdot e^{\frac{-(p_k-\mu_l)^2}{2\sigma_l^2}} + \frac{w_c}{\sqrt{2\pi}\sigma_c} \cdot e^{\frac{-p_k^2}{2\sigma_c^2}} + \frac{w_r}{\sqrt{2\pi}\sigma_r} \cdot e^{\frac{-(p_k-\mu_r)^2}{2\sigma_r^2}}, \tag{A.1}$$

where subscripts l, c and r represent left, central and right Gaussian distributions respectively; $k = \{x, y, z\}$; w_l, w_c and w_r are the weights attached to the respective distributions, and are summed to unity; μ_l and μ_r are the means; σ_l and σ_r are the standard deviations of the left and right Gaussian distributions respectively. The main reason to use a triple Gaussian model is to reduce the error in fitting each background magnitude-weighted phase value [58], as discussed in Section 2.3.4.

Therefore, in PC-MRA speed images, a signal m is determined by the modulus of the

three random variables, i.e.

$$m = \sqrt{p_x^2 + p_y^2 + p_z^2}. \tag{A.2}$$

The characteristic function of p_k^2 is given by

$$\Phi_{p_k^2}(t) = E[e^{itp_k^2}], \tag{A.3}$$

$$= \int_{-\infty}^{\infty} e^{itp_k^2} \cdot f_{p_k}(p_k) \cdot dp_k, \tag{A.4}$$

where $i = \sqrt{-1}$, and $k = \{x, y, z\}$. Therefore,

$$\Phi_{p_k^2}(t) = \frac{w_l e^{\frac{-\mu_l^2}{2\sigma_l^2}}}{\sqrt{2\pi}\sigma_l} \cdot \int_{-\infty}^{\infty} e^{(\frac{\mu_l}{\sigma_l^2})p_k} e^{-(\frac{1}{2\sigma_l^2} - it)p_k^2} dp_k + \frac{w_c}{\sqrt{2\pi}\sigma_c} \cdot \int_{-\infty}^{\infty} e^{-(\frac{1}{2\sigma_c^2} - it)p_k^2} dp_k + \frac{w_r e^{\frac{-\mu_r^2}{2\sigma_r^2}}}{\sqrt{2\pi}\sigma_r} \cdot \int_{-\infty}^{\infty} e^{(\frac{\mu_r}{\sigma_r^2})p_k} e^{-(\frac{1}{2\sigma_r^2} - it)p_k^2} dp_k \tag{A.5}$$

According to the Fourier transforms[1] [44], the characteristic function $\Phi_{p_k^2}(t)$ in Equation A.5 is given by

$$\Phi_{p_k^2}(t) = \frac{w_l}{\sqrt{1 - 2it\sigma_l^2}} \cdot e^{\frac{it\mu_l^2}{1-2it\sigma_l^2}} + \frac{w_c}{\sqrt{1 - 2it\sigma_c^2}} + \frac{w_r}{\sqrt{1 - 2it\sigma_r^2}} \cdot e^{\frac{it\mu_r^2}{1-2it\sigma_r^2}}. \tag{A.6}$$

Let T_l, T_c and T_r be the first, second and third terms on the right hand side of Equation A.6.

Since the characteristic functions of the sum of independent variables is the product of their separated characteristic functions [39, Ch 2], the characteristic function of q, where q is a random variable and $q = p_x^2 + p_y^2 + p_z^2$, is then given by

$$\Phi_q(t) = \Phi_{p_x^2}(t) \cdot \Phi_{p_y^2}(t) \cdot \Phi_{p_z^2}(t), \tag{A.7}$$

$$= T_c^3 + \underbrace{3T_c^2(T_l + T_r)}_{first\ order} + \underbrace{3T_c(T_l^2 + T_r^2 + 2T_lT_r)}_{second\ order} + \underbrace{T_l^3 + 3T_l^2T_r + 3T_lT_r^2 + T_r^3}_{third\ order}, \tag{A.8}$$

where the equation consists of first, second and third order terms of T_l and T_r.

Firstly, we consider T_c^3 in Equation A.8. By using the inversion formula of the characteristic function [69], the PDF of T_c^3 is obtained as

$$f_{T_c^3}(q) = \frac{1}{2\pi} \cdot \int_{-\infty}^{\infty} T_c^3(t) \cdot e^{-itq} \cdot dt, \tag{A.9}$$

$$= \frac{1}{2\pi} \cdot \int_{-\infty}^{\infty} \frac{w_c^3}{(1 - 2it\sigma_c^2)^{\frac{3}{2}}} \cdot e^{-itq} \cdot dt. \tag{A.10}$$

[1] According to [44], the Fourier transform of a function $f(t)$ and its inverse transform are given by $\hat{f}(w) = \int_{-\infty}^{\infty} e^{-iwx} f(x)dx$ and $f(x) = \frac{1}{2\pi}\int_{-\infty}^{\infty} e^{iwx}\hat{f}(w)dw$ respectively. If $f(x) = e^{-ax^2}$, then according to the Fourier transform table in [44], $\int_{-\infty}^{\infty} e^{-iwx}e^{-ax^2}dx = \sqrt{\frac{\pi}{a}}e^{\frac{-w^2}{4a}}$. For the first term in the right hand side of Equation A.5, let $-iw = \frac{\mu_l}{\sigma_l^2}$ and $a = \frac{1}{2\sigma_l^2} - it$, the result in Equation A.6 can be obtained. The same applies to the third term in the right hand side of Equation A.5.

Let $s = 1 - 2it\sigma_c^2$, and then Equation A.10 can be re-expressed as

$$f_{T_c^3}(q) = \frac{w_c^3 \cdot e^{\frac{-q}{2\sigma_c^2}}}{2\sigma_c^2} \cdot \frac{1}{2\pi i} \cdot \int_{1-i\infty}^{1+i\infty} e^{\left(\frac{q}{2\sigma_c^2}\right)s} \cdot \frac{1}{s^{\frac{3}{2}}} \cdot ds. \tag{A.11}$$

Applying inverse Laplace transforms[2] gives,

$$f_{T_c^3}(q) = \frac{w_c^3 \cdot \sqrt{q}}{\sqrt{2\pi}\sigma_c^3} \cdot e^{\frac{-q}{2\sigma_c^2}}. \tag{A.12}$$

We then consider one of the first order terms $T_c^2 T_l$ in Equation A.8. Similarly, by using the inversion formula of the characteristic function [69], the PDF can be obtained and is given by

$$f_{T_c^2 T_l}(q) = \frac{1}{2\pi} \cdot \int_{-\infty}^{\infty} T_c^2 T_l(t) \cdot e^{-itq} \cdot dt, \tag{A.13}$$

$$= \frac{1}{2\pi} \cdot \int_{-\infty}^{\infty} \frac{w_c^2 w_l}{(1 - 2it\sigma_c^2)\sqrt{1 - 2it\sigma_l^2}} \cdot e^{\frac{it\mu_l^2}{1-2it\sigma_l^2}} \cdot e^{-itq} \cdot dt. \tag{A.14}$$

Let $s = 1 - 2it\sigma_l^2$. Equation A.14 can be rewritten as

$$f_{T_c^2 T_l}(q) = \frac{w_c^2 w_l}{2\sigma_c^2} \cdot e^{\frac{-(\mu_l^2+q)}{2\sigma_l^2}} \cdot \frac{1}{2\pi i} \cdot \int_{1-i\infty}^{1+i\infty} e^{\left(\frac{q}{2\sigma_l^2}\right)s} \cdot \underbrace{\frac{1}{\left(\frac{\sigma_l^2}{\sigma_c^2} - 1\right) + s}}_{f_1(s)} \cdot \underbrace{\frac{1}{\sqrt{s}} \cdot e^{\left(\frac{\mu_l^2}{2\sigma_l^2}\right)\frac{1}{s}}}_{f_2(s)} \cdot ds. \tag{A.15}$$

Applying the Laplace transform convolution theorem to the functions f_1 and f_2 in Equation A.15 [2], we get

$$f_{T_c^2 T_l}(q) = \frac{w_c^2 w_l}{2\sigma_c^2} \cdot e^{\frac{-(\mu_l^2+q)}{2\sigma_l^2}} \cdot F_1 \otimes F_2 \left(\frac{q}{2\sigma_l^2}\right), \tag{A.16}$$

where $F_1 \otimes F_2(t)$ indicates convolution[3] and F_1 and F_2 are the inverse Laplace transformed functions, which are given by

$$F_1(t) = \mathcal{L}^{-1}\{f_1(s)\} = e^{\left(1 - \frac{\sigma_l^2}{\sigma_c^2}\right)t} \quad \text{and} \tag{A.17}$$

$$F_2(t) = \mathcal{L}^{-1}\{f_2(s)\} = \frac{1}{\sqrt{\pi t}} \cdot \cosh\left(\frac{\mu_l\sqrt{2t}}{\sigma_l}\right). \tag{A.18}$$

[2] According to [2], the Laplace transform of a function $f(t)$ and its inverse transform are given by $\hat{f}(s) = \int_0^\infty e^{-st} f(t)dt$ and $f(t) = \frac{1}{2\pi i} \cdot \int_{c-i\infty}^{c+i\infty} e^{ts}\hat{f}(s)ds$ respectively. According to the table of Laplace transforms in [2], if $\hat{f}(s) = s^{-\frac{3}{2}}$, then $f(t) = 2\sqrt{\frac{t}{\pi}}$. Therefore, we let $t = \frac{q}{2\sigma_c^2}$ and $c = 1$ in Equation A.11. The result in Equation A.12 can then be obtained.

[3] $\int_0^t F_1(t-\tau)F_2(\tau) \cdot d\tau$

As such, the PDF of the first order term is given by

$$f_{first\ order}(q) = 3(f_{T_c^2 T_l}(q) + f_{T_c^2 T_r}(q)), \tag{A.19}$$

where $f_{T_c^2 T_l}(q)$ is defined in Equation A.16, and the PDF of $T_c^2 T_r$ in Equation A.8 is obtained by replacing μ_l and σ_l with μ_r and σ_r respectively in Equation A.16. Similarly, by applying inverse Fourier transforms and the Laplace transform convolution theorem, the PDFs of the other third order terms, $f_{second\ order}(q)$ and $f_{third\ order}(q)$, can be derived accordingly.

For example, the PDF of $T_c T_l^2$, $f_{T_c T_l^2}$, is given by

$$f_{T_c T_l^2}(q) = \frac{w_c w_l^2}{2\sigma_c \sigma_l} \cdot e^{\frac{-(2\mu_l^2+q)}{2\sigma_l^2}} \cdot F_1^{'} \otimes F_2^{'}\left(\frac{q}{2\sigma_l^2}\right), \tag{A.20}$$

where $F_1^{'} \otimes F_2^{'}(t) = \int_0^t F_1^{'}(t-\tau) F_2^{'}(\tau) \cdot d\tau$, and $F_1^{'}$ and $F_2^{'}$ are given by

$$F_1^{'}(t) = \frac{1}{\sqrt{t}} \cdot e^{\left(1-\frac{\sigma_l^2}{\sigma_c^2}\right)t} \quad \text{and} \tag{A.21}$$

$$F_2^{'}(t) = I_0\left(\frac{2\mu_l\sqrt{t}}{\sigma_l}\right), \tag{A.22}$$

where I_0 is the modified Bessel function of the first kind. Also, the PDF of T_l^3, $f_{T_l^3}$, is given by

$$f_{T_l^3}(q) = \frac{w_l^3}{\sqrt{6\pi}\sigma_l\mu_l} \cdot e^{\frac{-(3\mu_l^2+q)}{2\sigma^2}} \cdot \sinh\left(\frac{\sqrt{3q}\mu_l}{\sigma_l^2}\right). \tag{A.23}$$

Let $f_{second\ order}(q)$ and $f_{third\ order}(q)$ be

$$f_{second\ order}(q) = 3(f_{T_c T_l^2}(q) + f_{T_c T_r^2}(q) + 2f_{T_c T_l T_r}(q)), \text{ and} \tag{A.24}$$

$$f_{third\ order}(q) = f_{T_l^3}(q) + 3f_{T_l^2 T_r}(q) + 3f_{T_l T_r^2}(q) + f_{T_r^3}(q). \tag{A.25}$$

Then, the PDF of q is given by

$$f_q(q) = \frac{1}{2\pi} \cdot \int_{-\infty}^{\infty} \Phi_q(t) \cdot e^{-itq} \cdot dt, \tag{A.26}$$

$$= f_{T_c^3}(q) + f_{first\ order}(q) + f_{second\ order}(q) + f_{third\ order}(q), \tag{A.27}$$

where $\Phi_q(t)$ is defined in Equation A.8.

Finally, since $m^2 = q$, the PDF of signal m in a speed image is given by

$$f_m(m) = 2mf_q(q=m^2), \tag{A.28}$$

$$= 2mf_{T_c^3}(q=m^2) + 2mf_{first\ order}(q=m^2) + 2mf_{second\ order}(q=m^2) + 2mf_{third\ order}(q=m^2), \tag{A.29}$$

where m is the signal (intensity) value in a speed image, and

$$2mf_{T_c^3}(q = m^2) = w_c^3 \cdot \frac{2m^2}{\sqrt{2\pi}\sigma_c^3} \cdot e^{\frac{-m^2}{2\sigma_c^2}}, \tag{A.30}$$

which is the Maxwell distribution [5].

We used Monte Carlo simulations to validate the signal PDF f_m in Equation A.29. Using the Monte Carlo simulation, the values of the three magnitude-weighted phase variables p_x, p_y and p_z in Equation A.2 were generated according to the statistical distribution described in Equation A.1. The signal m in a speed image is equal to the modulus of the three magnitude-weighted phase variables voxel-by-voxel in a 256×256 image. We set the parameter values based on typical experimental results. As shown in Figure A.1, the average values of the parameters in Equation A.1 are as follows: $w_l = 0.117 \pm 0.029$, $w_c = 0.782 \pm 0.047$, $w_r = 0.101 \pm 0.024$, $\sigma_c = 28.102 \pm 1.739$, $\mu_l = -41.354 \pm 3.761$, $\sigma_l = 19.161 \pm 2.51$, $\mu_r = 41.182 \pm 3.843$ and $\sigma_r = 18.683 \pm 2.29$.

Figure A.2a shows the histogram of the simulated data (dotted) and the histogram of the theoretical distribution $f_m(m)$ (solid) , which gives an absolute difference error of 3.12%. Figure A.2b shows the individual histograms of the Maxwell ($2mf_{T_c^3}(m)$), first order ($2mf_{first\ order}(m)$), second order ($2mf_{second\ order}(m)$) and third order ($2mf_{third\ order}(m)$) terms according to Equation A.29.

To illustrate the statistical characteristics of the first order term ($2mf_{first\ order}(m)$) , we assume that $\mu = \mu_l = \mu_r$ and $\sigma = \sigma_l = \sigma_r$ because, in practice, the values of μ_l and μ_r, and the values of σ_l and σ_r are very close to each other, as shown in Figure A.1c. We plot the changes of the first order term in Figure A.3a, in which the signal-to-noise ratios (SNR $= \frac{\mu}{\sigma}$, and $\sigma = 19$, which is fixed. As such, the value of SNR is changed only when the value of μ is changed.) were increased from 0 to 3. This figure shows (a) that when the SNR was equal to 0, the distribution of the first order term is reduced closely to the Maxwell distribution, and (b) that the distribution of the first order term changed smoothly from the Maxwell distribution to the Gaussian distribution as the SNR was increased. This smooth transition is modelled as a linear combination of the Maxwell and Gaussian distributions.

The change in the statistical characteristics of the second order term ($2mf_{second\ order}(m)$) are plotted in Figure A.3b, in which the SNR is increased from 0 to 3. A similar smooth transition from the Maxwell distribution to Gaussian distribution was observed. Therefore, the distribution of the second order term is also modelled as a linear Maxwell and Gaussian mixture. The same observation was obtained for the third order term. Therefore, all terms,

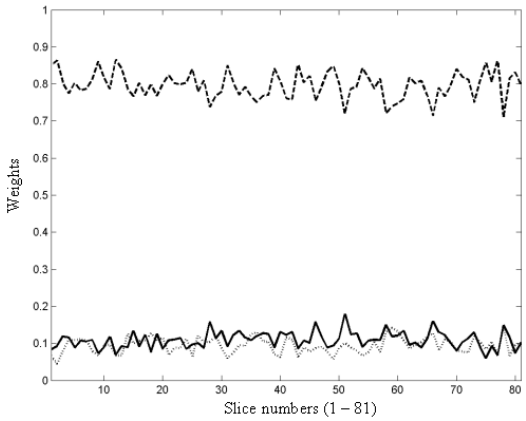

a. *Weights:* w_l *(solid),* w_c *(dashed) and* w_r *(dotted). Averages:* $w_l = 0.117 \pm 0.029$, $w_c = 0.782 \pm 0.047$ *and* $w_r = 0.101 \pm 0.024$.

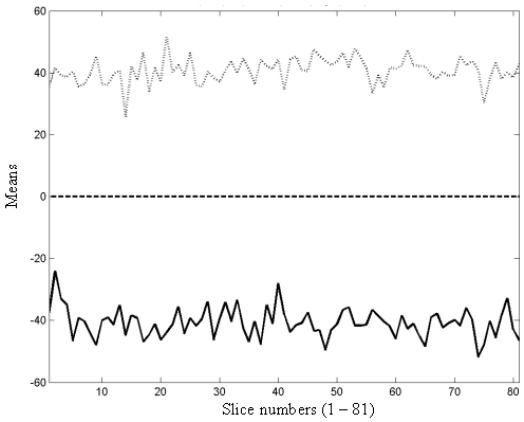

b. *Means:* μ_l *(solid),* μ_c *(dashed) and* μ_r *(dotted). Averages:* $\mu_l = -41.354 \pm 3.761$, $\mu_c = 0$ *and* $\mu_r = 41.182 \pm 3.843$

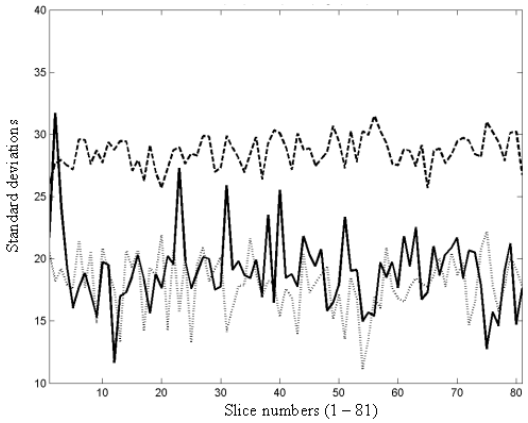

c. *Standard deviations:* σ_l *(solid),* σ_c *(dashed) and* σ_r *(dotted). Averages:* $\sigma_l = 19.161 \pm 2.51$, $\sigma_c = 28.102 \pm 1.739$ *and* $\sigma_r = 18.683 \pm 2.29$

Figure A.1: *Average parameter values of the triple Gaussian mixture model.*

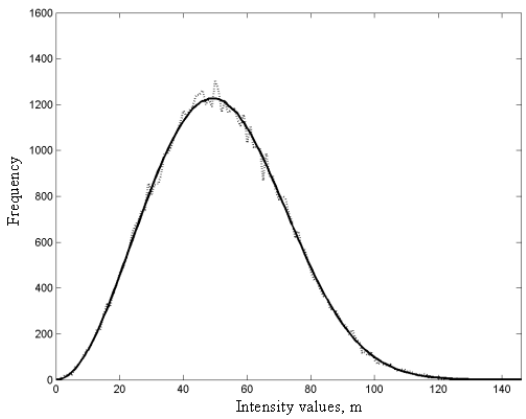

a. *Simulated data (dotted) and the theoretical distribution (solid). Absolute difference error*=3.12%.

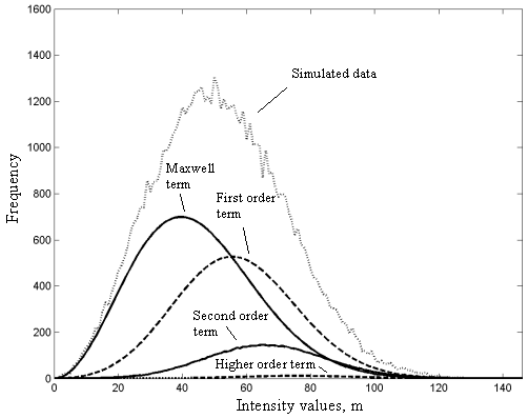

b. *Simulated data (dotted) and the individual distributions (solid and dashed).*

Figure A.2: *Histogram of the simulated data, the theoretical distribution, and distributions of the Maxwell, first order, second order and third order terms.*

including the Maxwell, first order, second order and third order terms, can be approximated by a combination of the Maxwell and Gaussian distributions.

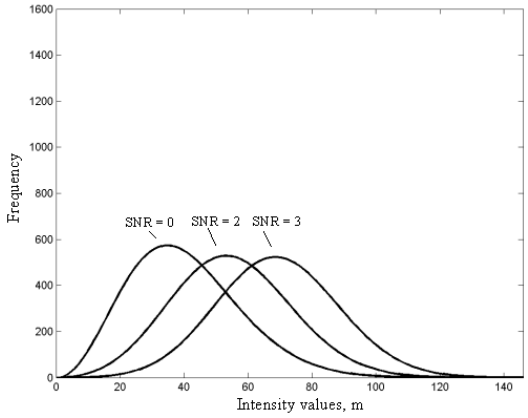

a. *First order term* $2mf_{first\ order}(m)$.

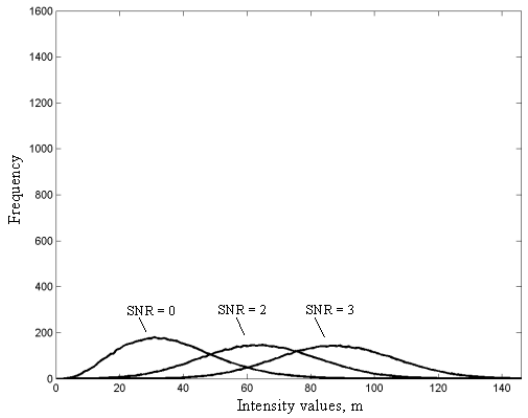

b. *Second order term* $2mf_{second\ order}(m)$.

Figure A.3: *Histograms of the first and second order terms at different SNRs.*

When the SNR is equal to zero, the sum of all terms closely follows the Maxwell distribution, whereas when the SNR is equal to 3, the sum of all terms follows a Gaussian distribution. These transitions are illustrated in Figures A.4a and A.4b. Consequently, the PDF of m, $f_m(m)$, can then be approximated by a mixture of Maxwell f_M and Gaussian f_G

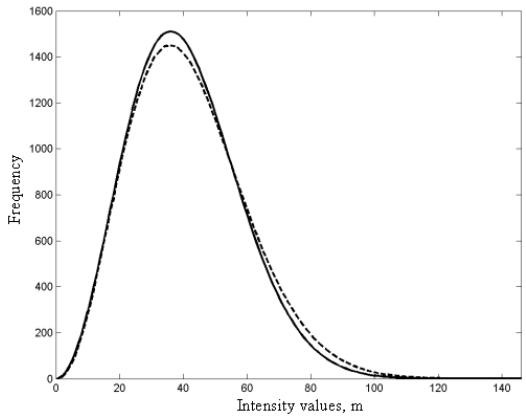

a. *Histograms of the fitted Maxwell distribution (solid), and the sum of all terms (dashed), including the Maxwell, first order, second order and third order terms, when* $SNR = 0$.

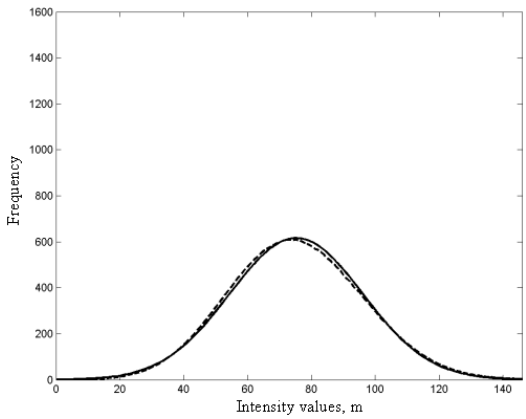

b. *Histograms of the fitted Gaussian distribution (solid), and the sum of all terms (dashed), including the Maxwell, first order, second order and third order terms, when* $SNR = 3$.

Figure A.4: *Histograms of the sum of all terms at different SNRs.*

distributions, given by

$$f_m(m) = w_M f_M(m) + w_G f_G(m), \tag{A.31}$$

where w_M and w_G are weights assigned to the Maxwell and Gaussian distributions respectively, and

$$f_M(m) = \frac{2m^2}{\sqrt{2\pi}\sigma_M^3} \cdot e^{\frac{-m^2}{2\sigma_M^2}} \quad \text{and} \tag{A.32}$$

$$f_G(m) = \frac{1}{\sqrt{2\pi} \cdot \sigma_G} \cdot e^{\frac{-(m-\mu_G)^2}{2\sigma_G^2}}, \tag{A.33}$$

Here σ_M is the standard deviation of the Maxwell distribution, and μ_G and σ_G are the mean and standard deviation of the Gaussian distribution respectively. As plotted in Figure A.5a, the Maxwell and Gaussian mixture was fitted to the same simulated data as above and gave an absolute difference error of 3.65%, which was comparable to the theoretical distribution (Equation A.29). The Maxwell and Gaussian distributions are separated in Figure A.5b to demonstrate their relative contributions to the model.

A detailed comparison between a Maxwell and Gaussian mixture model, and the Maxwell distribution for modelling the background signal in PC-MRA speed images is given in Section 2.5.

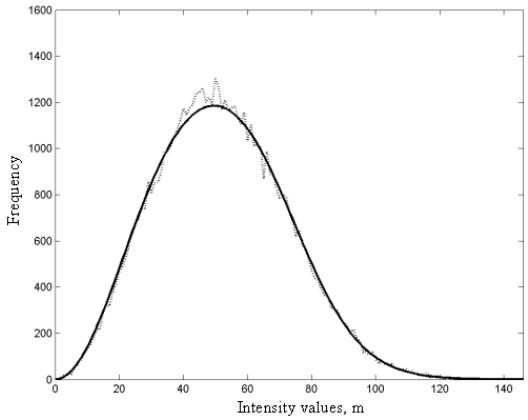

a. *Simulated data (dotted) and the Maxwell and Gaussian mixture (solid). Absolute difference error*=3.65%.

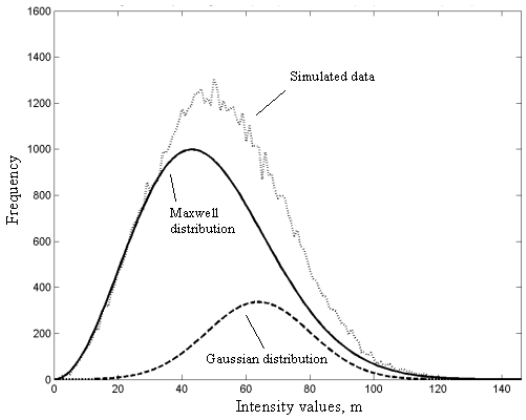

b. *Simulated data (dotted) and the individual distributions (solid and dashed).* $w_M = 0.7$, $w_G = 0.3$, $\sigma_M = 30.4$, $\mu_G = 60.0$ *and* $\sigma_G = 17.5$.

Figure A.5: *Histogram of the simulated data, the Maxwell and Gaussian mixture, and individual distributions.*

Appendix B

Derivation of update equations for the MGU model

This appendix shows how the parameters of the Maxwell-Gaussian-uniform (MGU) model can be estimated by using the EM algorithm. Recall from Equation 2.13 that, given a mixture model, consisted of Maxwell, Gaussian and uniform distributions, there are six parameters: w_M, w_G, w_U, σ_M^2, μ_G and σ_G^2, which need to be estimated. The overall probability density function $f(i)$ of an MRA speed image is given by Equation 2.13, where

$$f(i) = \underbrace{w_M f_M(i) + w_G f_G(i)}_{Background\ Signal} \quad + \quad \underbrace{w_U f_U(i)}_{Vascular\ Signal} \quad ,$$

and $w_M + w_G + w_U = 1$. The Maxwell distribution $f_M(i)$ is defined in Equation 2.10 and the Gaussian distribution $f_G(i)$ is defined as

$$f_G(i) = \frac{1}{\sqrt{2\pi} \cdot \sigma_G} \cdot e^{\frac{-(i-\mu_G)^2}{2\sigma_G^2}}, \tag{B.1}$$

and the uniform distribution is defined as

$$f_U(i) = \frac{1}{I_{max}}, \tag{B.2}$$

where I_{max} is the maximum intensity in the observed frequency histogram.

The EM algorithm is an iterative procedure that can be used to estimate the parameters by maximising the log-likelihood of the mixture distribution at each iteration [10]. The iterative procedure terminates when the change in log-likelihood or the parameters is sufficiently small.

Let the log-likelihood function be $L = \sum_{i=0}^{I_{max}} h(i) \cdot log\ f(i)$, where $h(i)$ is the observed frequency histogram and $f(i)$ is the mixture PDF in Equation 2.13. The change in log-likelihood function is given by

$$L^{k+1} - L^k = \sum_{i=0}^{I_{max}} h(i) \cdot log\left(\frac{f^{k+1}(i)}{f^k(i)}\right), \tag{B.3}$$

where index k represents the k^{th} iteration step. We aim to maximise the change of log-likelihood $L^{k+1} - L^k$ until the change is sufficiently small. Suppose that, given an intensity i, the posterior probabilities of the Maxwell, Gaussian and uniform distributions are $p(M|i)$, $p(G|i)$ and $p(U|i)$ respectively. Then $p(M|i) = \frac{w_M f_M(i)}{f(i)}$. The same form applies to $p(G|i)$ and $p(U|i)$. Also $p(M|i) + p(G|i) + p(U|i) = 1$. Equation B.3 can be rewritten as

$$L^{k+1} - L^k = \sum_{i=0}^{I_{max}} h(i) \cdot log\left(p^k(M|i)\frac{w_M^{k+1} f_M^{k+1}(i)}{f^k(i)p^k(M|i)} + p^k(G|i)\frac{w_G^{k+1} f_G^{k+1}(i)}{f^k(i)p^k(G|i)} + p^k(U|i)\frac{w_U^{k+1} f_U^{k+1}(i)}{f^k(i)p^k(U|i)}\right) \tag{B.4}$$

We use Jensen's inequality,

$$log(\lambda_1 x_1 + \lambda_2 x_2 + \lambda_3 x_3) \geq \lambda_1 log\ x_1 + \lambda_2 log\ x_2 + \lambda_3 log\ x_3, \tag{B.5}$$

where $\lambda_1 + \lambda_2 + \lambda_3 = 1$. Let $\lambda_1 = p^k(M|i)$, $\lambda_2 = p^k(G|i)$ and $\lambda_3 = p^k(U|i)$. By expanding $f^{k+1}(i)$ and multiplying by both numerator and denominator $p^k(M|i)$, $p^k(G|i)$ and $p^k(U|i)$, then from Equation B.4, we have

$$\begin{aligned} L^{k+1} - L^k \geq & \\ \sum_{i=0}^{I_{max}} h(i) \cdot \Bigg[& p^k(M|i) log\left(\frac{w_M^{k+1} f_M^{k+1}(i)}{f^k(i)p^k(M|i)}\right) + p^k(G|i) log\left(\frac{w_G^{k+1} f_G^{k+1}(i)}{f^k(i)p^k(G|i)}\right) + \\ & p^k(U|i) log\left(\frac{w_U^{k+1} f_U^{k+1}(i)}{f^k(i)p^k(U|i)}\right)\Bigg]. \end{aligned} \tag{B.6}$$

Therefore, maximising the right-hand-side of the inequality in Equation B.6 is equivalent to ensuring the maximal lower bound to the change in log-likelihood is achieved until the log-likelihood converges to a stationary point.

Maximisation with respect to w_M^{k+1}, w_G^{k+1} and w_U^{k+1}: the right-hand-side of Equation B.6 can be rearranged to isolate the terms related to w_M^{k+1}, w_G^{k+1} and w_U^{k+1}. Let

$$Q_w = \sum_{i=0}^{I_{max}} h(i) \cdot (p^k(M|i) \cdot log\ w_M^{k+1} + p^k(G|i) \cdot log\ w_G^{k+1} + p^k(U|i) \cdot log\ w_U^{k+1}). \tag{B.7}$$

Then we need to maximise Q_w under the constraint $w_M^{k+1} + w_G^{k+1} + w_U^{k+1} = 1$, i.e. maximise

$$Q_w + \lambda \cdot (1 - w_M^{k+1} - w_G^{k+1} - w_U^{k+1}), \tag{B.8}$$

where λ is the Lagrange multiplier. Setting the derivatives with respect to w_M^{k+1}, w_G^{k+1} and w_U^{k+1} to zero gives,

$$\begin{aligned} \lambda \cdot w_M^{k+1} &= \sum_{i=0}^{I_{max}} h(i) \cdot p^k(M|i), \\ \lambda \cdot w_G^{k+1} &= \sum_{i=0}^{I_{max}} h(i) \cdot p^k(G|i) \quad \text{and} \\ \lambda \cdot w_U^{k+1} &= \sum_{i=0}^{I_{max}} h(i) \cdot p^k(U|i). \end{aligned} \tag{B.9}$$

Summing Equation B.9 gives $\lambda = n$, where n is the total number of voxels. Hence, we obtain

$$\begin{aligned} w_M^{k+1} &= \frac{1}{n} \cdot \sum_{i=0}^{I_{max}} h(i) \cdot p^k(M|i), \\ w_G^{k+1} &= \frac{1}{n} \cdot \sum_{i=0}^{I_{max}} h(i) \cdot p^k(G|i) \quad \text{and} \\ w_U^{k+1} &= \frac{1}{n} \cdot \sum_{i=0}^{I_{max}} h(i) \cdot p^k(U|i). \end{aligned} \tag{B.10}$$

Maximisation with respect to σ_M^2: the right-hand-side of Equation B.6 can be rearranged to isolate the terms related to σ_M^2, giving

$$Q_M = \sum_{i=0}^{I_{max}} h(i) \cdot p^k(M|i) \cdot log\ f_M^{k+1}(i). \tag{B.11}$$

Setting the derivatives of Q_M with respect to σ_M^2 to zero gives

$$\sum_{i=0}^{I_{max}} h(i) \cdot p^k(M|i) \left[i^2 - 3(\sigma_M^2)^{k+1} \right] = 0. \tag{B.12}$$

Therefore, we obtain

$$(\sigma_M^2)^{k+1} = \frac{\sum_{i=0}^{I_{max}} h(i) \cdot p^k(M|i) \cdot i^2}{3 \cdot \sum_{i=0}^{I_{max}} h(i) \cdot p^k(M|i)}. \tag{B.13}$$

Maximisation with respect to μ_G and σ_G^2: the right-hand-side of Equation B.6 can be rearranged to isolate the terms related to μ_G and σ_G^2, giving

$$Q_G = \sum_{i=0}^{I_{max}} = h(i) \cdot p^k(G|i) \cdot log\ f_G^{k+1}(i). \tag{B.14}$$

Setting the derivatives of Q_G with respect to μ_G and σ_G^2 to zero gives

$$\sum_{i=0}^{I_{max}} h(i) \cdot p^k(G|i) \cdot (i - \mu_G^{k+1}) = 0 \quad \text{and} \tag{B.15}$$

$$\sum_{i=0}^{I_{max}} h(i) \cdot p^k(G|i) \cdot \left[(i - \mu_G^{k+1})^2 - (\sigma_G^2)^{k+1} \right] = 0. \tag{B.16}$$

Therefore, we obtain

$$\mu_G^{k+1} = \frac{\sum_{i=0}^{I_{max}} h(i) \cdot p^k(G|i) \cdot i}{\sum_{i=0}^{I_{max}} h(i) \cdot p^k(G|i)} \quad \text{and} \tag{B.17}$$

$$(\sigma_G^2)^{k+1} = \frac{\sum_{i=0}^{I_{max}} h(i) \cdot p^k(G|i) \cdot (i - \mu_G^{k+1})^2}{\sum_{i=0}^{I_{max}} h(i) \cdot p^k(G|i)}. \tag{B.18}$$

Note that the same derivation and update equations can be easily re-applied when the combination of distributions in the mixture is altered, e.g. a mixture of the two Gaussian distributions (Section 4.4).

Appendix C

Derivation of the equation of motion in 3D

This appendix shows the evolution equation derivation for the 3D geodesic flow using the divergence theorem. Let

$$H(t) = \int\int\int_{R_{xyz}} f(x,y,z)\ dV, \tag{C.1}$$

where R_{xyz} is a volumetric region in the Euclidean space, $H(t)$ is a volumetric integral of a functional $f(x,y,z)$ and $dV = dxdydz$ is a volume element in the Euclidean space.

Furthermore, let

$$L(x,y,z) = \frac{1}{3}\cdot\int_0^x f(\tau,y,z)\ d\tau, \tag{C.2}$$

$$M(x,y,z) = \frac{1}{3}\cdot\int_0^y f(x,\tau,z)\ d\tau\ and \tag{C.3}$$

$$N(x,y,z) = \frac{1}{3}\cdot\int_0^z f(x,y,\tau)\ d\tau \tag{C.4}$$

such that the condition

$$f(x,y,z) = \frac{\partial L}{\partial x} + \frac{\partial M}{\partial y} + \frac{\partial N}{\partial z} \tag{C.5}$$

is satisfied. Then, from Equation C.1 we obtain,

$$H(t) = \int\int\int_{R_{xyz}} div(L,M,N)\ dV, \tag{C.6}$$

where 'div' denotes the divergence operator. By applying the divergence theorem in 3D, we have

$$H(t) = \int\int_{\mathcal{S}_{xyz}} (L,M,N)\cdot\hat{n}\ d\sigma, \tag{C.7}$$

where $\mathcal{S}_{xyz}$ is a closed surface that encloses the region R_{xyz}, $\hat{n}$ is an unit surface normal and $d\sigma$ is a surface element in the Euclidean space. The parametric form of the surface $\mathcal{S}_{xyz}$ is given by

$$x = x(u, v, t), \quad y = y(u, v, t) \ \ and \ \ z = z(u, v, t), \tag{C.8}$$

where $u, v \in [0, 1]$ denote the space parameters and $t \in [0, \infty)$ denotes the time parameter. Now, the unit normal vector $\hat{n}$ is given by

$$\hat{n} = \frac{\vec{p_1} \times \vec{p_2}}{|\vec{p_1} \times \vec{p_2}|}, \tag{C.9}$$

where $\vec{p_1} = \left(\frac{\partial x}{\partial u}, \frac{\partial y}{\partial u}, \frac{\partial z}{\partial u}\right)^T$ and $\vec{p_2} = \left(\frac{\partial x}{\partial v}, \frac{\partial y}{\partial v}, \frac{\partial z}{\partial v}\right)^T$, and the surface element $d\sigma$ is given by

$$d\sigma = \sqrt{EG - F^2}\ dudv, \tag{C.10}$$

where $E = \left|\frac{\partial \mathcal{S}}{\partial u}\right|^2$, $G = \left|\frac{\partial \mathcal{S}}{\partial v}\right|^2$ and $F = \frac{\partial \mathcal{S}}{\partial u} \cdot \frac{\partial \mathcal{S}}{\partial v}$. Hence, Equation C.7 can be re-written as,

$$H(t) = \int_0^1 \int_0^1 (L, M, N) \cdot (\vec{p_1} \times \vec{p_2})\ dudv. \tag{C.11}$$

The derivative of Equation C.11 with respect to t gives

$$\frac{dH(t)}{dt} = \int_0^1 \int_0^1 (\frac{\partial x}{\partial t}, \frac{\partial y}{\partial t}, \frac{\partial z}{\partial t}) \cdot f\ (\vec{p_1} \times \vec{p_2})\ dudv, \tag{C.12}$$

where we have written $f = f(x, y, z)$ for simplicity of notation. Hence,

$$\frac{dH(t)}{dt} = \int \int_{\mathcal{S}_{xyz}} \frac{\partial \mathcal{S}}{\partial t} \cdot (f\ \hat{n})\ d\sigma. \tag{C.13}$$

Then, the following evolution equation should be solved in order to find the local minimum of $H(t)$,

$$\frac{\partial \mathcal{S}}{\partial t} = -f\ \hat{n}. \tag{C.14}$$

This forms the evolution equation of geodesic flow and shows the direction in which $H(t)$ is decreased most rapidly.

Bibliography

[1] E. Aarts and J. Korst. *Simulated Annealing and Boltzmann Machines*. Chichester, John Wiley & Sons, 1989.

[2] Milton Abramowitz and Irene A. Stegun. *Handbook of mathematical functions : with formulas, graphs and mathematical tables. Tenth Printing*. New York, A Wiley-Interscience publication, 1972.

[3] A. Adalsteinsson and J.A. Sethian. A Fast Level Set Method for Propagating Interfaces. *International Journal of Computational Physics*, 118:269–277, 1995.

[4] A. Adalsteinsson and J.A. Sethian. The Fast Construction of Extension Velocities in Level Set Methods. *International Journal of Computational Physics*, 148:2–22, 1999.

[5] A.H. Andersen and J.E. Kirsch. Analysis of noise in phase contrast MR imaging. *Medical Physics*, 23(6):857–869, 1996.

[6] M.A. Bernstein, M. Grgic, T.J. Brosnan, and N.J. Pelc. Reconstructions of Phase Contrast, Phased Array Multicoil Data. *Magnetic Resonance in Medicine*, 32:330–334, 1994.

[7] M.A. Bernstein, X.J. Zhou, J.A. Polzin, K.F. King, A. Ganin, N.J. Pelc, and G.H. Glover. Concomitant gradient terms in phase contrast MR: analysis and correction. *Magnetic Resonance in Medicine*, 39(2):300–308, 1998.

[8] Julian Besag. Spatial Interaction and the Statistical Analysis of Lattice Systems (with discussion). *Journal of the Royal Statistical Society. Series B (Methodological)*, 36(2):192–326, 1974.

[9] Julian Besag. On the Statistical Analysis of Dirty Pictures. *Journal of the Royal Statistical Society. Series B (Methodological)*, 48(3):259–302, 1986.

[10] C. Bishop. *Neural Networks for Pattern Recognition*. Oxford, Clarendon Press, 1995.

[11] Andrew Blake and Andrew Zisserman. *Visual Reconstruction*. Cambridge, Mass., The MIT Press, 1987.

[12] G.E.P. Box and G.C. Tiao. *Bayesian Inference in Statistical Analysis*. New York, John Wiley & Sons, 1973.

[13] A.C. Burleson, C.M. Strother, and V.T. Turitto. Computer Modeling of Intracranial Saccular and Lateral Aneurysms for the Study of Their Hemodynamics. *Neurosurgery*, 37(4):774–784, Oct. 1995.

[14] J.V. Byrne and G. Guglielmi. *Endovascular Treatment of Intracranial Aneurysms*. Berlin, Springer-Verlag, 1997.

[15] J.V. Byrne, M.J. Sohn, and A.J. Molyneux. Five-year experience in using coil embolization for ruptured intracranial aneurysms: outcomes and incidence of late rebleeding. *Journal of Neurosurgery*, 90:656–663, 1999.

[16] C.G. Caro, T.J. Pedley, R.C. Schroter, and W.A. Seed. *The Mechanics of the Circulation*. Oxford, Oxford University Press, 1978.

[17] V. Caselles, R. Kimmel, and G. Sapiro. Geodesic Active Contours. *International Journal of Computer Vision*, 22(1):61–79, 1997.

[18] V. Cerny. Thermodynamical approach to the travelling salesman problem:an efficient simulation algorithm. *Journal of Optimization Theory and Applications*, 45:41–51, 1985.

[19] James J. Clark and Alan L. Yuille. *Data Fusion for Sensory Information Processing Systems*. Boston, Kluwer Academic Publishers, 1990.

[20] Herve Delingette and Johan Montagnat. Topology and shape constraints on parametric active contours. *Technical Report 3880, INRIA, France*, 2000.

[21] R.O. Duda and Peter E. Hart. *Pattern Classification and Scene Analysis* . New York, John Wiley & Sons, 1973.

[22] Ibrahim M. Elfadel. From Random Fields to Networks. In *Ph.D. Thesis, Dept. of Mechanical Engineering, Massachusetts Institute of Technology*, 1993.

[23] J. Holzenbein et. al. Endovacular AAA treatment: expensive prestige or economic alternative? *European Journal of Vascular and Endovascular Surgery*, 14(4):265–272, Oct. 1997.

[24] G.N. Foutrakis, H. Yonas, and R.J. Sclabassi. Saccular Aneurysm Formation in Curved and Bifurcating Arteries. *American Journal of Neuroradiology (AJNR)*, 20:1309–1317, Aug. 1999.

[25] Jean Gallier. *Geometric Methods and Applications: for Computer Science and Engineering*. New York, Springer-Verlag, 2001.

[26] E.B. Gamble, D. Geiger, and T. Poggio. Integration of Vision Modules and Labelling of Surface Discontinuities. *IEEE Transactions on Systems, Man, and Cybernetics*, 19(6):1576–1581, 1989.

[27] Davi Geiger and Federico Girosi. Parallel and Deterministic Algorithms from MRF's: Surface Reconstruction. *IEEE Transactions on Pattern Analysis and Machine Intelligence*, PAMI-13(5):401–412, 1991.

[28] Stuart Geman and Donald Geman. Stochastic Relaxation, Gibbs Distributions, and the Bayesian Restoration of Images. *IEEE Transactions on Pattern Analysis and Machine Intelligence*, PAMI-6(6):721–741, 1984.

[29] Y.P. Gobin, J.L. Counord, P. Flaud, and J. Duffaux. In vitro study of haemodynamics in a giant saccular aneurysm model. *Neuroradiology*, 36:530–536, 1994.

[30] Jose Gomes and Olivier Faugeras. Reconciling Distance Functions and Level Sets. *Technical Report 3666, INRIA, France*, 1999.

[31] D.M. Greig, B.T. Porteous, and A.H. Seheult. Exact Maximum A Posteriori Estimation for Binary Images. *Journal of the Royal Statistical Society. Series B (Methodological)*, 51(2):271–279, 1998.

[32] Guido Guglielmi, Fernando Vinuela, Jacques Dion, and Gary Duckwiler. Electrothrombosis of saccular aneurysms via endovascular approach part 2: Preliminary clinical experience. *Journal of Neurosurgery*, 75:8–14, July 1991.

[33] Guido Guglielmi, Fernando Vinuela, Ivan Sepetka, and Velio Macellari. Electrothrombosis of saccular aneurysms via endovascular approach part 1: Electrochemical basis, technique, and experimental results. *Journal of Neurosurgery*, 75:1–7, July 1991.

[34] R.M. Haralick. Statistical and structural approaches to texture. *Proceedings of the IEEE*, 67(5):786–804, 1979.

[35] R.M. Haralick, K. Shanmugam, and I. Dinstein. Textural Features for Image Classification. *IEEE Transactions on Systems, Man, and Cybernetics*, SMC-3:610–621, 1973.

[36] K. Held, E.R. Kops, B.J. Krause, W.M. Wells III, R. Kikinis, and H.W.M. Gartner. Markov Random Field Segmentation of Brain MR Images. *IEEE Transactions on Medical Imaging*, 16(6):878–886, 1997.

[37] R. Mark Henkelman. Measurement of signal intensities in the presence of noise in MR images. *Medical Physics*, 12(2):232–233, 1985.

[38] Berthold K. P. Horn. *Robot Vision*. Cambridge, Mass., The MIT Press, 1986.

[39] Harold Jeffreys. *Theory of Probability. Third Edition*. Oxford, Oxford University Press, 1961.

[40] Tina Kapur. Model based three dimensional Medical Image Segmentation. In *Ph.D. Thesis, Artificial Intelligence Laboratory, Massachusetts Institute of Technology*, 1999.

[41] J. Kim, J.W. Fisher III, A. Tsai, C. Wible, A.S. Willsky, and W.M. Wells III. Incorporating Spatial Priors into an Information Theoretic Approach for fMRI Data Analysis. In *Medical Image Computing and Computer-Assisted Intervention (MICCAI)*, pages 62–71, 2000.

[42] S. Kirkpatrick, Jr. C.D. Gellatt, and M.P. Vecchi. Optimization by simulated annealing. *IBM Thomas J. Watson Research Center, Yorktown Heights, NY*, 1982.

[43] Peter Kovesi. *Invariant Measures of Image Features from Phase Information*. Ph.D. Thesis, University of Western Australia, 1996.

[44] E. Kreyszig. *Advanced Engineering Mathematics 7th ed.* New York, John Wiley & Sons, INC., 1993.

[45] K. Krissian, G. Malandain, and N. Ayache. Model-based multiscale detection and reconstruction of 3D vessels. *INRIA Tech. Report 3442*, 1998.

[46] K. Krissian, G. Malandain, and N. Ayache. Model-based Detection of Tubular Structures in 3D Images. *INRIA Tech. Report 3736*, 1999.

[47] B.P. Lathi. *Modern Digital and Analog Communication Systems*. New York, Holt, Rinehart and Winston, 1983.

[48] S.Z. Li. *Markov Random Field Modeling in Computer Vision*. Tokyo, Springer-Verlag, 1995.

[49] L.M. Lorigo, O. Faugeras, W.E.L. Grimson, R. Keriven, R. Kikinis, and C.F. Westin. Co-dimension 2 Geodesic Active Contours for MRA Segmentation. In *International Conference on Information Processing in Medical Imaging (IPMI)*, pages 126–139, 1999.

[50] M. Low, K. Perktold, and R. Raunig. Hemodynamics in Rigid and Distensible Saccular Aneurysms: A Numerical Study of Pulsatile Flow Characteristics. *Biorheology*, 30:287–298, 1993.

[51] R. Malladi, J.A. Sethian, and B.C. Vemuri. Shape Modelling with Front Propagation: A Level Set Approach. *IEEE Trans. on Pattern Analysis and Machine Intelligence*, 17(2):158–175, 1995.

[52] James Manyika and Hugh Durrant-Whyte. *Data Fusion and Sensor Management: a decentralized information-theoretic approach*. New York, Ellis Horwood Limited, 1994.

[53] J. Marroquin, S. Mitter, and T. Poggio. Probabilistic Solution of Ill-Posed Problems in Computational Vision. *Journal of the American Statistical Association*, 82(397):76–89, Mar. 1987.

[54] D.A. McDonald. *Blood Flow in Arteries:* 2^{nd} *ed.* London: Edward Arnold, 1974.

[55] K. McGee, J. Felmlee, and et al. Autocorrection of Three-dimensional Time-of-flight MR Angiography of the Circle of Willis. *American Journal of Roentgenology*, 176:513–518, 2001.

[56] C. McGowan and M. Wood. Phase-encode Reordering to Minimize Errors Caused by Motion. *Magnetic Resonance in Medicine*, 35:391–398, 1996.

[57] T. McInerney and D. Terzopoulos. Medical image segmentation using topologically adaptable surfaces. In *Computer Vision, Virtual Reality and Robotics in Medicine (CVRMed)*, pages 92–101, 1995.

[58] J. McLachlan and D. Peel. *Finite Mixture Models*. New York, John Wiley & Sons Ltd., 2000.

[59] R.A. McLaughlin, J. Hipwell, G.P. Penney, K. Rhode, A. Chung, J.A. Noble, and D.J. Hawkes. Intensity-based Registration versus Feature-based Registration for Neurointerventions. In *Medical Image Understanding and Analysis (MIUA)*, pages 69–72, 2001.

[60] N. Metropolis, A. Rosenbluth, M. Rosenbluth, A. Teller, and E. Teller. Equation of state calculations by fast computing machines. *Journal of Chemical Physics*, 21:1087–1092, 1953.

[61] M. Mignotte, C. Collet, and et al. Three-Class Markovian Segmentation of High-Resolution Sonar Images. *Computer Vision and Image Understanding*, 76(3):191–204, 1999.

[62] D. Mumford and J. Shah. Boundary Detection by Minimizing Functionals, 1. In *International Conference on Computer Vision and Pattern Recognition*, pages 22–26, 1985.

[63] David Niemann. *Phase Contrast MRA can detect periprocedural anatomic and hemodynamic changes in embolized AVMs*. M.Sc. Thesis, University of Oxford, 2001.

[64] H.V. Ortega. Computer simulation helps predict cerebral aneurysms. *Journal of Medical Engineering & Technology*, 22(4):179–181, July/Aug. 1998.

[65] S. Osher and R. P. Fedkiw. Level Set Methods: An Overview and Some Recent Results. *UCLA CAM Report 00(08)*, 2000.

[66] S. Osher and J.A. Sethian. Fronts Propagating with Curvature-Dependent Speed: Algorithms Based on Hamilton-Jacobi Formulations. *International Journal of Computational Physics*, 79:12–49, 1988.

[67] S. Oyre, S. Ringgaard, S. Kozerke, W.P. Paaske, S. Ringgaard, M. Erlandsen, P. Boesiger, and E.M. Pedersen. Accurate non-invasive quantization of blood flow, cross sectional lumen vessel area, and wall shear stress by three-dimensional paraboloid modelling of magnetic resonance velocity data. *J. Am. Coll. Cardiol.*, 32:128–134, 1998.

[68] S. Oyre, S. Ringgaard, S. Kozerke, W.P. Paaske, M.B. Scheidegger, P. Boesiger, and E.M. Pedersen. Quantization of circumferential subpixel vessel wall position and wall shear stress by multiple sectored three-dimensional paraboloid modelling of velocity encoded cine MR. *Magnetic Resonance in Medicine*, 40:645–655, 1998.

[69] Athanasios Papoulis. *Probability, Random Variables, and Stochastic Processes. Third Edition.* New York, McGraw-Hill, Inc., 1991.

[70] N. Paragios and R. Deriche. Geodesic Active Regions for Texture Segmentation. *Technical Report 3440, INRIA, France*, 1998.

[71] E. Parzen. *Modern Probability Theory and Its Applications.* New York, John Wiley & Sons, Inc., 1960.

[72] N.J. Pelc, M.A. Bernstein, A. Shimakawa, and G.H. Glover. Encoding strategies for three-direction Phase Contrast MR imaging of flow. *Journal of Magnetic Resonance Imaging (JMRI)*, 1:405–413, 1991.

[73] A. Ravishankar Rao and Ramesh C. Jain. Computerized Flow Field Analysis: Oriented Texture Fields. *IEEE Transactions on Pattern Analysis and Machine Intelligence*, 14(7):693–709, 1992.

[74] P.A. Rinck. *Magnetic Resonance in Medicine.* Oxford, Blackwell Scientific Publications, 1993.

[75] B.D. Ripley. The Use of Spatial Models as Image Priors. In *Spatial Statistics and Imaging. Lecture Notes-Monograph Series, 20, Springer-Verlag*, pages 309–340, 1991.

[76] Sebastien Roy and Venu Govindu. MRF Solution for Probabilistic Optical Flow Formulations. In *IEEE Workshop on Graph Algorithms and Computer Vision*, `http://www.cs.cornell.edu/iccv-graph-workshop/`, 1999.

[77] Guillermo Sapiro. *Geometric Partial Differential Equations and Image Analysis.* Cambridge, Cambridge University Press, 2001.

[78] J.A. Sethian. *Level Set Methods and Fast Marching Methods.* Cambridge, Cambridge University Press, 1999.

[79] H.J. Steiger, Jr., J.N. Oshinski, R.I. Pettigrew, and D.N. Ku. Computational Simulation of Turbulent Signal Loss in 2D Time-of-Flight Magnetic Resonance Angiograms. *Magnetic Resonance in Medicine*, 37:609–614, 1997.

[80] C.M. Strother, V.B. Graves, and A. Rappe. Aneurysm Hemodynamics: An Experimental Study. *American Journal of Neuroradiology (AJNR)*, 13:1089–1095, 1992.

[81] P. Summers, A. Bhalerao, and D. Hawkes. Multi-resolution, Model-based segmentation of MR Angiograms. *Journal of Magnetic Resonance Imaging (JMRI)*, 7(6):950–957, 1997.

[82] P. Summers, D.W. Holdsworth, H. Nikolov, Y. Papaharilou, and B.K. Rutt. Design and Construction of a Robust Flow Phantom for the ISMRM Flow and Motion Group Multi-Centre Trial. In *International Society for Magnetic Resonance in Medicine*, page 458, 2000.

[83] D.J. Weatherall, J.G.G. Ledingham, and D.A. Warrell. *Oxford Textbook of Medicine : 3rd Ed.* Oxford, Oxford University Press, 1996.

[84] C.F. Westin, L.M. Lorigo, O. Faugeras, W.E.L. Grimson, S. Dawson, A. Norbash, and R. Kinkinis. Segmentation by Adaptive Geodesic Active Contours. In *Medical Image Computing and Computer-Assisted Intervention (MICCAI)*, pages 266–275, 2000.

[85] D.J. Wilcock, T. Jaspan, and B.S. Worthington. Problems and pitfalls of 3-D TOF magnetic resonance angiography of the intracranial circulation. *Clinical Radiology*, 50:526–532, 1995.

[86] D.L. Wilson. *An Improved Planning Protocol for the Endovascular Treatment of Intracranial Aneurysms.* D.Phil. Thesis, University of Oxford, 1998.

[87] O. Wink, W.J. Niessen, and M.A. Viergever. Fast Delineation and Visualization of Vessels in 3-D Angiographic Images. *IEEE Transactions on Medical Imaging*, 19:337–346, 2000.

[88] A. Yezzi, S. Kichenassamy, P. Olver, and A. Tannenbaum. A gradient surface approach to 3D segmentation. *IEEE Transactions on Medical Imaging*, 16:199–210, 1997.

[89] S.C. Zhu and A.L. Yuille. Region competition: Unifying Snakes, Region growing, and Bayes/MDL for multiband Image Segmentation. *IEEE Transactions on Pattern Analysis and Machine Intelligence*, 18(9):884–900, 1996.